DEVELOPMENT OF ALITE CALCIUM SULFOALUMINATE CEMENT FOR SMART CEMENT-BASED MATERIALS APPLICATION

PITHIWAT TIANTONG

A Thesis Submitted to the Graduate School of Naresuan University
in Partial Fulfillment of the Requirements
for the Doctor of Philosophy in Civil Engineering
2021

DEVELOPMENT OF ALITE CALCIUM SULFOALUMINATE CEMENT FOR SMART CEMENT-BASED MATERIALS APPLICATION

PITHIWAT TIANTONG

A Thesis Submitted to the Graduate School of Naresuan University
in Partial Fulfillment of the Requirements
for the Doctor of Philosophy in Civil Engineering
2021

Thesis entitled "Development of alite calcium sulfoaluminate cement for smart cement-based materials application"

By PITHIWAT TIANTONG

has been approved by the Graduate School as partial fulfillment of the requirements for the Doctor of Philosophy in Civil Engineering of Naresuan University

Oral Defense Committee

.... Chair
(Assistant Professor Panuwat Joyklad, Ph.D.)

.... Advisor
(Assistant Professor Phongthorn Julphunthong, Ph.D.)

.... Co Advisor
(Associate Professor Tawat Suriwong, Ph.D.)

.... Co Advisor
(Associate Professor Theerachai Bongkarn, Ph.D.)

.... Internal Examiner
(Assistant Professor Sasikorn Leungvichcharoen, Ph.D.)

Approved

....
(Associate Professor Krongkarn Chootip, Ph.D.)

Dean of the Graduate School

Title DEVELOPMENT OF ALITE CALCIUM
SULFOALUMINATE CEMENT FOR SMART
CEMENT-BASED MATERIALS APPLICATION
Author PITHIWAT TIANTONG
Advisor Assistant Professor Phongthorn Julphunthong, Ph.D.
Co-Advisor Associate Professor Tawat Suriwong, Ph.D.
Associate Professor Theerachai Bongkarn, Ph.D.
Academic Paper Ph.D. Dissertation in Civil Engineering, Naresuan
University, 2021

Keywords Alite calcium sulphoaluminate cement, KNLNTS ceramics,
composite, dielectric and piezoelectric properties

ABSTRACT

Different compositions of alite calcium sulfoaluminate (ACSA) clinkers were synthesised for use as an alternative, more environmentally friendly binder than ordinary Portland cement (OPC). ACSA clinkers have a lower firing temperature than OPC clinkers, thus reducing carbon dioxide emissions during processing. Calcium fluoride (CaF_2) and copper oxide (CuO) were added to the raw materials and the resulting phase formation for clinkers was compared with and without these additives. Three different compositions of ACSA clinkers as well as six different firing temperatures were tested and evaluated. Results revealed that the additives accelerated initial formation of alite at as low as 1,100°C. The ability to process ACSA at such a low temperature enabled the coexistence of alite - ye'elimite phases in the clinker, while SO_3 content greatly influenced alite crystal formation. Unexpected $CaSO_4 \times 2H_2O$ loss due to evaporation in the firing process initially reduced the ye'elimite phase content below the designed target. Using additional $CaSO_4 \times 2H_2O$ subsequently increased ye'elimite content to the target level when the experiment was repeated using the optimal composition and temperature.

New smart composites as sensors and actuators in civil engineering for structural health monitoring were fabricated and investigated. A novel 0–3 piezoelectric composite is presented which consists of $(K_{0.44}Na_{0.52}Li_{0.04})(Nb_{0.84}Ta_{0.10}Sb_{0.06})O_3$ (KNLNTS) as the piezoelectric phase and alite calcium sulphoaluminate cement (ACSA cement) as the matrix phase. Since they are new types of materials, the synthesising processes for each material is intensively investigated. ACSA cement was successfully prepared using an appropriate composition and fired at 1250°C for 30 minutes. The Rietveld refinement technique was used to determine the amount of each quantitative phase, calculated through the XRD patterns from the model structure. Characterisation of the KNLNTS sintered ceramics was investigated by XRD patterns, SEM, dielectric properties, and piezoelectric properties. The optimum synthesising conditions provided sintered KNLNTS ceramics that had dielectric constant and dielectric loss at room temperature values of 1,386 and 0.022, respectively. The KNLNTS/ACSA cement composites were prepared with various KNLNTS content in the range of 30-70 vol.%. The hardened density, acoustic impedance, microstructure, dielectric properties, and piezoelectric coefficient of the composites were also investigated.

ACKNOWLEDGEMENTS

First of all, I would like to express my sincere appreciation to my supervisor, Asst. Prof. Dr. Phongthorn Julphunthong who has given me useful suggestion, and all supports he has given me throughout my education life. The work presented in this thesis was conducted in the Department of Civil engineering and Department of Physics at Naresuan University, and Department of Physics and Materials Science at Chiang Mai University.

I would also thanks and acknowledge Assoc. Prof. Dr. Theerachai Bongkarn and Assoc. Prof. Dr. Tawat Suriwong, Prof. Dr. Arnon Chaipanich, and Asst. Prof. Dr. Rattiyakorn Rianyoi for their time and valuable comments of this thesis. This study was made possible by a generous grant from Research and Researchers for Industries (RRi) (PHD60I0052). I am grateful to Siam City Cement Public Company Limited for financial assistance and material characterisations.

PITHIWAT TIANTONG

TABLE OF CONTENTS

Page

ABSTRACT C

ACKNOWLEDGEMENTS .... E

TABLE OF CONTENTS .... F

List of table I

List of figures .... K

CHAPTER I INTRODUCTION 1

- 1.1 Reasons for the study 1
- 1.2 Objective of this study 5
- 1.3 Scope of the study 6

CHAPTER II RELATED THEORETICAL AND LITERATURE REVIEW 8

- 2.1 Ordinary Portland cement (OPC) 8
  - 2.1.1 Cement composition 8
  - 2.1.2 Phase composition of cement 10
  - 2.1.3 Finenss 11
  - 2.1.4 Hydration of Portland cement 12
    - 2.1.4.1 Hydration of tricalcium aluminate 13
    - 2.1.4.2 Hydration of ferrite 13
    - 2.1.4.3 Hydration of calcium silicate 14
- 2.2 Calcium sulfoaluminate cement (CSA) 15
  - 2.2.1 Introduction 15
  - 2.2.2 Phase composition 15
- 2.3 Alite calcium sulfoaluminate cement (ACSA cement) 17
  - 2.3.1 Related theoretical with ACSA cement 17
  - 2.3.2 Effect of additive for alite formation 18
- 2.4 Piezoelectricity theory 26

2.4.1 Poling......29
2.4.2 Ferroelectric properties......30
2.4.3 Basic theory of dielectric and piezoelectric properties......31
2.5 Piezoelectric materials: KNN-based piezoelectric ceramic......33
2.6 Piezoelectric – cement composite......37
CHAPTER III THE EXPERIMENTS......46
3.1 Synthesis of alite calcium sulfoaluminate cement......46
3.2 Modified potassium sodium niobate ceramic fabrication......48
3.3 Fabrication of the piezoelectric-cement composites......50
3.4 Characterization measurements......51
CHAPTER IV THE RESULTS PART I: Effects of CaF_2-CuO additives and various firing temperatures on characteristics of alite calcium sulfoaluminate clinkers......55
4.1 Particle size analysis results......55
4.2 X-ray fluorescence analysis results......55
4.3 X-ray diffraction patterns analysis results......56
4.4 Phase quantitative analysis......58
4.4.1 Effect of additives on clinker phase formation......63
4.4.2 Effect of firing temperature on clinker phase formation......64
4.4.3 C_3S polymorphic transformation......64
4.5 Influence of sulfur on ye’elimite formation......69
CHAPTER V THE RESULTS PART II: Fabrication and characterisation of 0–3 KNLNTS piezoelectric ceramic/alite calcium sulphoaluminate cement composites......73
5.1 KNLNTS ceramics......73
5.1.1 KNLNTS calcined powders......73
5.1.2 KNLNTS sintered ceramics......75
5.2 KNLNTS/ACSA cement composite......79
5.2.1 Density and acoustic impedance......79
5.2.2 Microstructure analysis......80

5.2.3 Effect of KNLNTS content on dielectric and piezoelectric properties 82
5.2.4 Effect of hydration ages on dielectric and piezoelectric properties 86
CHAPTER VI CONCLUSIONS 91
REFERENCES 93
BIOGRAPHY 99

List of table

Page

Table 1 Physical and crystallographic data on pure tricalcium silicate polymorphs[1] 10

Table 2 The benefits and drawbacks of OPC and CSA cements 17

Table 3 Targeted mineralogical phase assemblage of BAY clinkers, raw materials dosages and nominal element composition of raw mixtures.[16] 19

Table 4 RQPA (wt%) for BAY clinkers.[16] 20

Table 5 RQPA (wt%) for sc-BAY_4 clinker at different thermal cycles.[16] 20

Table 6 The five theoretical clinker composition with three modulus values.[21] 21

Table 7 The clinker's alite and ye'elimite constituents burnt at a temperature of 1,300 °C.[26] 23

Table 8 Analyses of the chemical composition and phase composition of ACSA clinker and OPC utilized.[51] 24

Table 9 MgO concentration in clinker (wt.%).[52] 24

Table 10 Properties of PZT-PC composites.[58] 38

Table 11 Compositions of the composites used for Fly ash was replacement into Portland cement.[61] 41

Table 12 Target compositions of the mixture designs. 46

Table 13 Targeted mineralogical phase assemblage and raw materials. 47

Table 14 Specifications of the base materials for the KNLNTS + 0.2wt%CuO +0.4wt%Fe_2O_3 +0.3wt%Bi_2O_3 ceramic 49

Table 15 Chemical composition of clinkers fired at 1,250 °C. 55

Table 16 Quantity of phase analysis of Mix A clinkers fired at various temperatures calculated by the Rietveld refinement technique. 65

Table 17 Quantity of phase analysis of Mix B clinkers fired at various temperatures calculated by the Rietveld refinement technique. 66

Table 18 Quantity of phase analysis of Mix C clinkers fired at various temperatures calculated by the Rietveld refinement technique..67

Table 19 *RMSE* values of Mix A, Mix B, and Mix C...68

Table 20 Design phase compositions and clinkers with excess sulfur fired at 1,250 C of Mix C (M-group), Mix C-M + 0.5x SO_3 and Mix C-M + 1x SO_3. 70

Table 21 Atomic ratios of sample clinker phases as calculated from EDS data. The corresponding theoretical atomic ratio of each clinker phase is included in parentheses. 72

Table 22 Percent perovskite phase of the KNLNTS calcined powders and the KNLNTS sintered ceramics. 75

Table 23 The dielectric properties and piezoelectric coefficient of the KNLNTS ceramics. 79

List of figures

Page

Figure 1 Typical proportions of phases for the formation of Portland clinker minerals as a function of the progressive kiln temperature.[1] 9

Figure 2 Particle size distribution data for Type I and III Portland cement. 12

Figure 3 Process of hydration of the Portland cement's basic ingredients..................14

Figure 4 Development of the strength of Portland cement's major ingredients...........15

Figure 5 XRD patterns of anhydrous ACSA and after 2 h, 7 d and 180 d of hydration. (E – ettringite, Ms – monosulfate, F ferrite, HG – iron-containing siliceous hydogranet, CH – portlandite, Ye – ye'elimite, An – anhydrite, A – alite and 18

Figure 6 Optimal firing regimes for each composition as determined by XRD graphs [21] 21

Figure 7 The influence of copper oxide concentration on the free lime content of clinker.[26]...22

Figure 8 The DTA curves for samples devoid of CuO and those containing 1.0 percent CuO.[26]...22

Figure 9 The XRD for samples devoid of CuO and those containing 1.0 percent CuO.[26] 23

Figure 10 The concentration of free lime in clinkers as a function of MgO.[52]........25

Figure 11 XRD patterns of clinkers with addition of MgO.[52] 26

Figure 12 Piezoelectric material's direct and indirect effects on voltage generation and shape change when voltage is applied. [55]..27

Figure 13 Classification of the 32 crystallographic crystal classes. 28

Figure 14 Traditional piezoelectric ceramic crystal structure, above and below the Curie point [55]..29

Figure 15 Left: prior to polarization, random orientation of polar domains , center: polarization of a piezoelectric ceramic, and right: polarization that remains after an electric field is removed. [55] 29

Figure 16 Schematic of typical ferroelectric P-E hysteresis loop. 31

Figure 17(a) A and d parallel-plate capacitors in vacuum connected to a voltage source, (b) Circuit closure creates a brief burst of current. AUC (area under the curve) is the charge held on the capacitor. (c) Similar to (a) only a dielectric is now between the plates, (d) The charge stored on the parallel plates must be larger than the charge stored in the (b). [56] 32

Figure 18 Variation of dielectric constant as a function of temperature of $K_xNa_{1-x}NbO_3$ (where x = 0.53, 0.48, 0.45 and 0.41) ceramic at 1 kHz and 10 kHz frequencies.[57] 34

Figure 19 Temperature variations of KNN and KNN-LS dielectric constants at 100 kHz. [31] 35

Figure 20 (a) Bulk densities, (b) d_{33} of KNN-N, KNN-LS and KNN-LST12 as a function of sintering temperature.[32] 36

Figure 21 Dielectric constant and dielectric loss of KNN-N, KNN-LS, and KNN-LST12 at room temperature.[32] 37

Figure 22 Effect of BNBK content on 1-3 BNBK-PC composites' acoustic impedance. [59] 39

Figure 23 The dielectric characteristics of composites containing 1-3 BNBK and PC. [59] 39

Figure 24 (a) Coefficient of electromechanical coupling and (b) The piezoelectric coefficient of composites containing 1-3 BNBK-PC.[59] 40

Figure 25 BNT-PC composites dielectric constant and dielectric loss.[60] 41

Figure 26 Composite BZT-PC SEM micrographs with (a) 10% volume of fly ash content, (b) 30% volume of fly ash content. And (c) 50% volume of fly ash content.[61] 42

Figure 27 The effect of fly ash on dielectric properties of (a) 40BZT-PC/FA, (b) 50BZT-PC/FA composites at 1 kHz.[61] 43

Figure 28 Fly ash's effect on the piezoelectric coefficient of (a) 40BZT-PC/FA and (b) 50BZT-PC/FA composites. [61] 44

Figure 29 The dielectric loss of PP materials with time and temperature.[62]............45

Figure 30 The effect of curing time on the piezoelectric coefficient of PP materials under the AA, AB, BA, and BB heating conditions.[62] 45

Figure 31 Steps for investigating the KNLNTS + sinter aids......................................49

Figure 32 Piezoelectric-cement based composites fabrication. 51

Figure 33 Particle size distibution of raw materials, D $[4,3]$ = volume mean diameter (μm) 55

Figure 34 XRD patterns of Mix A-clinker; (a) R-group and (b) M-group
1 = C_3S, 2 = C_2S, 3 = C_4A_3S, 4 = C_4AF, 5 = C_3A, 6 = free lime, 7 = $C_{12}A_7$ 56

Figure 35 XRD patterns of Mix B-clinker; (a) R-group and (b) M-group
1 = C_3S, 2 = C_2S, 3 = C_4A_3S, 4 = C_4AF, 5 = C_3A, 6 = free lime, 7 = $C_{12}A_7$....57

Figure 36 XRD patterns of Mix C-clinker; (a) R-group and (b) M-group
1 = C_3S, 2 = C_2S, 3 = C_4A_3S, 4 = C_4AF, 5 = C_3A, 6 = free lime, 7 = $C_{12}A_7$ ...58

Figure 37 Variation of phases contents with firing temperatures of Mix A 61

Figure 38 Variation of phases content with firing temperatures of Mix B 62

Figure 39 Variation of phases content with firing temperatures of Mix C 63

Figure 40 XRD patterns with and without excess SO_3 of Mix C at 1,250 °C: 70

Figure 41 SEM images of (a) Mix C (M-group), (b) Mix C-M + 1*x* SO_3 71

Figure 42 XRD patterns of KNLNTS powders calcined at 650 – 900 °C; 74

Figure 43 XRD patterns of KNLNTS ceramics sintered at 1000 – 1100 °C; ♦ = Perovskite, ♠ = Nb_2O_3. 74

Figure 44 SEM images of the pellet surface sintered at (a) 1000°C, (b) 1025°C, (c) 1050°C, (d) 1075°C, and (e) 1100°C. 76

Figure 45 The temperature dependence of dielectric properties of KNLNTS ceramics sintered at (a) 1000°C, (b) 1025°C, (c) 1050°C, (d) 1075°C, and (e) 1100°C. ..78

Figure 46 The density and acoustic impedance of KNLNTS/ACSA cement composite. 79

Figure 47 Microstructure of 0-3 connectivity KNLNTS/ACSA cement composites with KNLNTS content of 30 vol.%: (a) SEM micrograph; (b) element mapping for Nb and Ca in composite; (c) EDS analysis of the KNLNTS ceramics phase; and (d) EDS analysis of the cement matrix phase. 81

Figure 48 Microstructure of 0-3 connectivity KNLNTS/ACSA cement composite with KNLNTS content of 70 vol.%: (a) SEM micrograph; (b) element mapping for Nb and Ca in composite; (c) EDS analysis of the KNLNTS ceramics phase; and (d) EDS analysis of the cement matrix phase. 81

Figure 49 Comparison of the dielectric constant from the experimental data and the numerical model for 0-3 KNLNTS/ACSA cement composites. 83

Figure 50 Comparison of the piezoelectric coefficient from experimental data and the numerical model for 0-3 KNLNTS/ACSA cement composites. 84

Figure 51 Comparison of the piezoelectric voltage factor from experimental data and the numerical model for 0-3 KNLNTS/ACSA cement composites............................. 86

Figure 52 Variation over time of the dielectric constants for the KNLNTS ceramic and the KNLNTS/ACSA cement composites. 88

Figure 53 Variation over time of the piezoelectric coefficients for the KNLNTS ceramic and the KNLNTS/ACSA cement composites... 89

Figure 54 Variation over time of the piezoelectric voltage factor for the KNLNTS ceramic and the KNLNTS/ACSA cement composites... 89

Figure 55 (a) The comparison between the dielectric constant and piezoelectric coefficient with KNLNTS content at 28 days, (b) The d_{33} / ε_r ratio and KNLNTS content at 28 days.. 90

CHAPTER I
INTRODUCTION

1.1 Reasons for the study

Ordinary Portland cement (OPC) is the most commonly used type of cement throughout the world due to its high strength and adaptability to a wide variety of applications [1]. The raw materials for OPC production as limestone and either clay or shale are inexpensive [2, 3]. When these materials are mixed together and fired, the resulting cement is mainly composed of C_3S (alite), C_2S (belite), C_3A (tricalcium aluminate), and C_4AF (calcium aluminoferrite). However, the processing of OPC has two major disadvantages. First, high energy is required to grind the raw materials and complete the firing process at high temperatures of around 1,450-1,550 °C. The second disadvantage is the negative impact that these processes have on the environment, as, together, they emit about 870 kg of carbon dioxide for each metric ton of cement produced. The cement industry is responsible for around 5% of carbon dioxide global emissions, resulting from the burning of fossil fuels during the rotary kiln sintering process, limestone decomposition and transportation [1-5].

Calcium sulfoaluminate cement (CSA cement) was first developed in China in the 1960s and is widely produced in China [6] as an alternative binder to OPC. The main compounds in CSA cement include $C_4A_3\bar{S}$ (ye'elimite), C_2S, and C_4AF. CSA cement saves substantial amounts of energy because it can be fired at 1,250 °C and is also easier to grind. Emissions of CO_2 are reduced when compared to OPC [7-9]. Gartner et al. [10] demonstrated that the CO_2 released from the main compound of OPC (C_3S), during the manufacturing firing process was 578 kg/ton phase, while the main compound of CSA cement ($C_4A_3\bar{S}$) emitted only 216 kg/ton phase. Besides energy savings and lower environmental impact, other benefits of CSA cement include rapid setting time, high early strength, low shrinkage and high sulfate resistance due to $C_4A_3\bar{S}$ hydration [11]. The main obstruction for CSA applications is that strength development at up to 28 days is significantly lower than that of OPC due to the slow reactivity of C_2S [12, 13]. Maximum strength over time of CSA remains constant but is lower than OPC. One solution to improve the low strength of CSA cement involves blending CSA cement with OPC. This improves the mechanical properties of the hydrated mixture cement and was investigated by Trauchessec et al. [14]. Another solution is to separately synthesise the pure phases of $C_4A_3\bar{S}$, C_3S and C_2S at different firing temperatures and then blend these phases to combine the advantages of each phase, as demonstrated by Skibsted et al. [15]. However, this method requires a complicated production process. Hence, the recent process route of interest is to synthesise the coexistence of C_3S and $C_4A_3\bar{S}$ phases at the same firing temperature, producing alite calcium sulfoaluminate (ACSA cement) [16]. The $C_4A_3\bar{S}$ phase initially forms above 1,000 °C and decomposes when the firing temperature exceeds 1,300 °C [17, 18], while the ideal temperature of C_3S phase formation is around 1,450 °C [1]. Thus, coexistence of C_3S and $C_4A_3\bar{S}$ phases does not occur.

This problem can be resolved by the incorporation of small amounts of additives into the raw mix, thereby promoting the formation of C_3S at lower temperatures. Small amounts of CaF_2 also exhibit fluxing properties that generate several chemical reactions during clinker formation [19]. This causes the temperature of C_3S formation to decrease, resulting in the formation of the C_3S phase at a lower temperature [20]. Tristana et al. demonstrated that adding CaF_2 (0.8 wt.%) to the raw meal improved the burnability of the raw mix and promoted C_3S formation at lower temperatures between 50 °C-100 °C [21], while Londono et al. showed that coexistence of C_3S and $C_4A_3\bar{S}$ occurred at a firing temperature of 1,300 °C by adding CaF_2 at 0.9 wt.% [16]. Raquel et al. [22] demonstrated that with the increase of CaF_2 from 0.5-1 wt.% in the raw mixture of ACSA cement, the content of C_3S significantly increased, with a suitable clinkering temperature of 1,300 °C. These researchers also found that using CuO as another additive, besides CaF_2, promoted the formation of C_3S at lower temperatures. The CuO compound changed the crystallisation process and affected the formation of C_3S [1]. Addition of CuO was very effective in reducing free lime and the viscosity of the liquid phase [1, 23]. Yang et al. [24] demonstrated improved burnability of C_3S by adding CuO at less than 0.5 wt.%. However, only small amounts of CuO can be used as an additive due to the cost of the product, the amount of pollution released in the processes and the detrimental effect on the hydration reaction of the cement when CuO content is higher than 1.5 wt.% [25]. Only a small amount of CuO (0.1 wt.%) is needed to promote the formation of C_3S and $C_4A_3\overline{S}$ and to facilitate the coexistence of the two minerals in the clinker at temperatures ranging from 1,250 °C to 1,300 °C [26].

Smart materials or piezoelectric materials have recently been the focus of numerous studies and applications, including in relation to sensors and actuators [27, 28]. The most often employed materials in these applications are lead-based perovskites, such as PZT-based ceramics, due to their superior electromechanical characteristics. At present there is significant interest in using lead-free materials rather than lead-containing ceramic due to the environmental risks that lead poses. Potassium Sodium Niobate ($K_{0.5}Na_{0.5}NbO_3$, KNN) exhibits a perovskite structure at room temperature with a high Curie temperature (~420 °C). However, Due to the difficulty of manufacturing dense ceramics using a standard sintering technique, these lead-free ceramics exhibit poor piezoelectric characteristics ($\mathrm{d}_{33} \approx 80$ pC/N). [29]. To improve the sintering behaviour of KNN ceramics, different additives [30] such as $LiSbO_3$, $LiTaO_3$, and $LiNbO_3$ have been added to KNN materials. Gerold A. Schneider et al.[31] discovered that increasing the Li and Sb content in KNN results in a drop in the ceramics' Curie and first-order phase transition temperatures, while it also enhanced the piezoelectric and dielectric properties. Binary and ternary systems have been researched to increase the densification and electrical characteristics of KNN ceramics. [32] by adding other piezoelectric elements such as $(K_{0.50}Na_{0.46}Li_{0.04})(Nb_{0.96-x}Ta_xSb_{0.04})O_3$ ($x = 0, 0.12$) or (KNN-LST) and $K_{0.52}N_{0.46}NbO_3$ or (KNN-N). The dielectric and piezoelectric properties of KNN-LST ceramic are higher than those of KNN-N ceramic. Bongkarn et al. [29] synthesised lead-free $(K_{0.44}Na_{0.52}Li_{0.04})(Nb_{0.84}Ta_{0.10}Sb_{0.06})O_3$ KNLNTS ceramics. A sample sintered at 1100°C exhibited the densest ceramic (4.42 g/cm^3), highest dielectric constant ($\varepsilon_r = 6114$), and piezoelectric coefficient ($d_{33} = 203$ pC/N). It is widely known that obtaining dense microstructures in KNN ceramics is difficult due to the instability of alkali metal oxide at elevated temperatures. Using sintered aids such as CuO, Fe_2O_3, ZnO, B_2O_3, and Bi_2O_3 to improve the densification of ceramics has been reported by [33-35]. Moreover, Sang et al. [36] demonstrated that utilizing 0.3 wt% Bi_2O_3 + 0.4 wt.% Fe_2O_3 + 0.2 wt.% CuO as sintering aids decreased the sintering temperature and improved the ceramic's densification and electrical characteristics.

Since 2002, cement-based piezoelectric composites have been created and are now being employed in a variety of civil engineering applications, including sensors and actuators for real-time monitoring of concrete structures, among others. [37-40]. The advantage of composite materials over piezoelectric materials is their increased compatibility and the ability to alter their acoustic impedance to match the host structural materials (concrete). The acoustic impedance of concrete is $\approx 10\times10^6$ kg/m^2s, while that of piezoelectric ceramics such as KNN is $\approx 30\times10^6$ kg/m^2s [41]. Due to the variations in acoustic impedance and volume stability between piezoelectric ceramics and concrete, piezoelectric ceramic sensors employed in concrete buildings may be erroneous. Following that, 0–3 type cement-based piezoelectric composites were created to address compatibility concerns with concrete constructions where traditional sensors and actuators do not respond synchronously with the concrete. [38, 42-44]. Numerous research have been conducted to determine the piezoelectric capabilities at 24 hours after polarisation of 0-3 type cement-based piezoelectric composites that have been cured for one or three days. [44-47]. However, age after polarisation had an effect on the dielectric and piezoelectric properties of the cement, which continue to alter as the cement hydrates. [48].

Many previous studies demonstrated that CaF_2 or CuO as additives were efficient in promoting the coexistence of C_3S - $C_4A_3\overline{S}$ phases at low temperatures. However, incorporation of CaF_2 and CuO additives to reduce the firing temperature at which the C_3S phase is formed; especially for coexistence with $C_4A_3\overline{S}$, has not been reported. To study the effects of raw meal composition and firing temperature on phase formation of ACSA clinker, three different compositions were designed and then fired at six different temperatures. Each composition was prepared by adding CaF_2 and CuO in the raw meal. The resulting phase formations were compared without additive supplementation. The XRD patterns and the Rietveld refinement technique were used to analyse phase formation behaviour, phase content and crystal transformation of the ACSA clinkers. Quantitative phase analysis results were verified by scanning electron microscopy (SEM) and energy dispersive spectroscopy (EDS) investigations.

In this research, Lead-free $(K_{0.44}Na_{0.52}Li_{0.04})(Nb_{0.84}Ta_{0.10}Sb_{0.06})O_3$ ceramic was synthesised via employing sintering aids such as CuO, Fe_2O_3 and Bi_2O_3 in the solid-state reaction method. Temperature effects on phase formation and microstructure were examined during calcination and sintering. The effects of KNLNTS ceramic fraction on the hardened density, acoustic impedance, dielectric properties, and piezoelectric coefficient of the 0-3 KNLNTS piezoelectric ceramic / ACSA cement composite were also studied in this work. This advancement is particularly beneficial for concrete structures, as it resolves the matching issue of acoustic impedance and volume compatibility that has been found in concrete structures constructed with ACSA concrete.

1.2 Objective of this study

Part I: Effects of CaF_2-CuO additives and various firing temperatures on characteristics of alite calcium sulfoaluminate clinkers

1. Develop the ACSA clinker in the laboratory scale for three different mix compositions. Determine the effect of additives and firing temperatures on phase formation and the optimal firing temperature for ACSA clinker synthesis.
2. Investigate effect of adding the excess SO_3 content into the raw materials in order to enhance the formation of $C_4A_3\bar{S}$ in the ACSA clinker.

Part II: Fabrication and characterisation of 0–3 KNLNTS piezoelectric ceramic/alite calcium sulphoaluminate cement composites

1. Determine the optimal calcined temperature and sintered temperature of $(K_{0.44}Na_{0.52}Li_{0.04})(Nb_{0.84}Ta_{0.10}Sb_{0.06})O_3$ + 0.2wt%CuO + 0.4wt%Fe_2O_3 + 0.3wt%Bi_2O_3 (KNLNTS + sinter aids) ceramic synthesized with the solid-state method by phase identification, microstructure analysis, dielectric and piezoelectric properties.

2. Fabricate the KNLNTS-ACSA cement composites with several KNLNTS fractions. Investigate the effect of KNLNTS content and ACSA cement hydration on acoustic impedance, interfacial transition zone, and dielectric and piezoelectric properties.

1.3 Scope of the study

1. Synthesis of alite – calcium sulfoaluminate clinker

To synthesize alite-calcium sulfoaluminate clinker, high purity powders of $CaCO_3$, SiO_2, Al_2O_3, Fe_2O_3, and $CaSO_4{\cdot}2H_2O$ were used as raw materials, and the additives CaF_2 (0.8%) and CuO (0.1%), both analytical grade, were added in the raw meal. Four target phase compositions of alite calcium sulfoaluminate cement (ACSA cement) were designed. Three mixtures of the above powders corresponding to the four target phase compositions were prepared. These three mixtures were tested, first with the two additives and then without, for a total of six experimental powder mixtures, to compare the additives' impact on the final phase compositions of ACSA cement. Each sample were separated into six sections, with each section subjected to a unique firing condition. All samples were initially fired at 900 °C for 30 minutes, with a heating rate of 5 °C/minute, and then fired continue at one of the six different maximum temperatures (1,100 °C; 1,200 °C; 1,250 °C; 1,275 °C; 1,300 °C; or 1,325 °C) for 30 minutes, using the same earlier heating rate of 5 °C/minute. Thus, six experimental powder mixtures were fired at six different temperatures for a total of 36 experimental trials. After grinding, the chemical composition, and phase composition of all the fired mixtures were investigated.

2. Fabrication of the KNLNTS-ACSA cement composites

First a piezoelectric material consisting of KNLNTS + 0.2wt%CuO + 0.4wt%Fe_2O_3 + 0.3wt%Bi_2O_3 (KNLNTS + sinter aids) were synthesized using the conventional solid-state technique. High purity powders of $KHCO_3$, Na_2CO_3, Li_2CO_3, Nb_2O_5, Ta_2O_5, and Sb_2O_3 were used as starting materials for the $(K_{0.44}Na_{0.52}Li_{0.04})(Nb_{0.84}Ta_{0.10}Sb_{0.06})O_3$ (KNLNTS) ceramic. After mixing, these powders were calcined at either 650, 750, 850, and 900 °C (four versions) for 6 hours with a heating rate of 5

°C/minute. The four calcined samples were analyzed using the XRD technique in order to determine the optimal version that delivers the purest KNLNTS. The calcined sample thus selected were then mixed with oxides of CuO, Fe_2O_3, and Bi_2O_3 in order to lower the sintering temperature and improve the physical properties of the KNLNTS ceramic. The resulting mixture was pressed into disk shaped pellets with a diameter of 12 mm at a pressure of 80 MPa. After that, the pellets were sintered at either 1,000; 1,025; 1,050; 1,075; or 1,100 °C for 2 hours with a heating rate of 5 °C/minute. The density of the three sintered samples were checked and they were analyzed using XRD, and SEM to obtain the optimal version. That optimal sample were then tested for its acoustic impedance, dielectric properties, and piezoelectric properties. Next a series of five new composites of (KNLNTS + sinter aids) – ACSA cement composites were fabricated with varying ACSA cement volume contents of 30%, 40%, 50%, 60%, or 70%, respectively. Finally the acoustic impedance, density, dielectric properties, and piezoelectric properties of these five composites were investigated.

CHAPTER II
RELATED THEORETICAL AND LITERATURE REVIEW

2.1 Ordinary Portland cement (OPC)

2.1.1 Cement composition

Ordinary Portland cement (OPC) has been widely utilized as a binder in construction because it contains approximately two-thirds calcium silicate (C_3S and C_2S) by mass and also contains tricalcium aluminate (C_3A) and ferrite (C_4AF) as major phases. This cement is made from limestone ($CaCO_3$) and clay, marl, or shale as raw ingredients (SiO_2, Al_2O_3 and Fe_2O_3). CaO (60-70 percent), SiO2 (18-22 percent), Al_2O_3 (4-6 percent), and Fe_2O_3 (2-4 percent) are the major oxides, while MgO, K_2O, TiO_2, Mn_2O_3, and SO_3 are minor components. The raw components were then combined, crushed, and heated to approximately 1,450 degrees Celsius to generate clinker (Clinker is solid material formed in high temperature processes). Following that, it was substituted with 0-10 percent calcium sulfate and processed again to make cement[1].

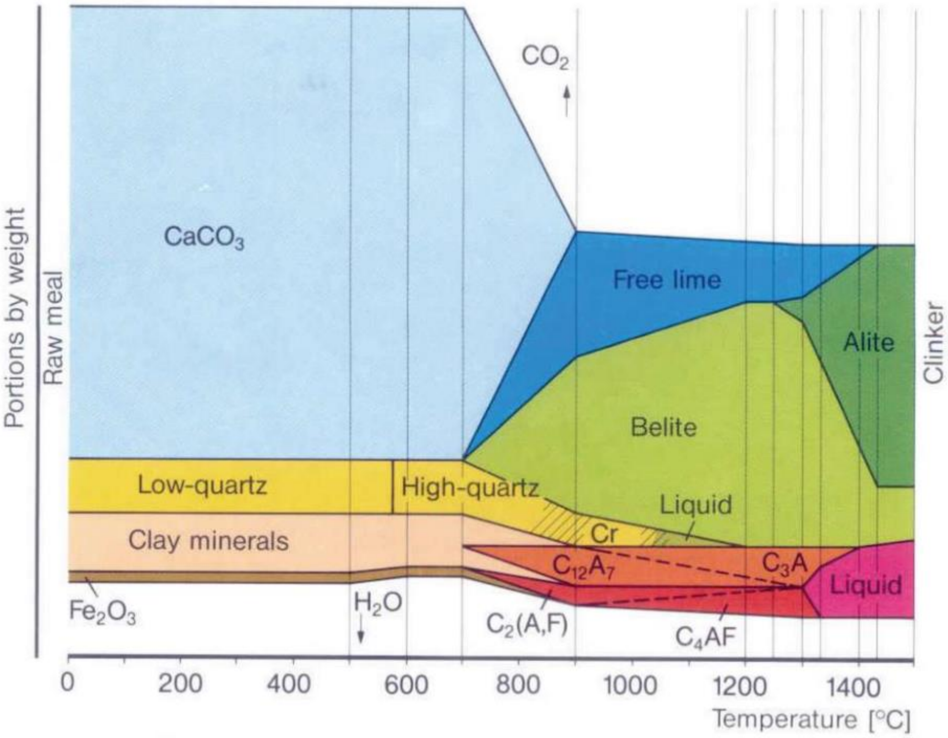

Figure 1 Typical proportions of phases for the formation of Portland clinker minerals as a function of the progressive kiln temperature.[1]

In the clinkering process, the reactions of each phase occur at different temperature after being heated. The first one is dehydration which up to a temperature of about 700 °C for removal free water. Calcium oxide (CaO) and carbon dioxide (CO_2) were produced as a gas as a result of the dissociation of calcium carbonate at temperatures between 700 and 900 degrees Celsius. This was followed by the initial combination of aluminum oxide, iron oxide, and silicon dioxide with calcium oxide (CaO). After that belite, tricalcium aluminate and ferrite were being formed in the temperature range of 900-1,300°C. In the temperature zone 1,300-1,450 °C, the liquid phase appears and then helps to promote the formation of alite (C_3S) by the reaction of belite and free lime. These processes are summarized in Figure 1. During the cooling stage, the entering air provides the immediate quenching that is required. When the clinker melt cools, it re-crystallizes into tricalcium aluminate and ferrite, respectively. Fast cooling will also occur for alite, depending on the rate at which it is cooled. The slow cooling should avoid due to alite will dissolve back into the liquid phase and found as secondary belite[1, 4, 49].

2.1.2 Phase composition of cement

The main phase composition of OPC consists of alite, belite, tricalcium aluminate, and ferrite. Other phases, such as quartz, periclase, free lime, and so on, may be present in trace amounts, usually less than 1 percent by weight.

Alite is the most importance hydraulic phase of Portland clinker which occurs in about 50-90%. It is chemically a tricalcium silicate ($3CaO{\cdot}SiO_2$). Alite undergoes several phase transformations which are summarized by 3 groups: one rhombohedral (R), three monoclinic (M_3, M_2, M_1) and three triclinic (T_3, T_2, T_1). The following is the cooling sequence:

$$R \xrightarrow{1{,}060\ ^{\circ}C} M_3 \xrightarrow{1{,}050\ ^{\circ}C} M_2 \xrightarrow{990\ ^{\circ}C} M_1 \xrightarrow{980\ ^{\circ}C} T_3 \xrightarrow{920\ ^{\circ}C} T_2 \xrightarrow{600\ ^{\circ}C} T_1$$

Table 1 shows the physical and crystallographic characteristics of various phases based on their composition. Production clinkers are typically of the monoclinic variety (M1, M3), and their properties are strongly sensitive on the impurity level, heating and cooling history, and other factors, e.q. addition of some MgO stabilizes M_3 but increasing SO_3 content promote M_1 formation. Alite crystalizes in the melt between 1,300 °C and 1,450 °C which higher temperatures than belite.

Table 1 Physical and crystallographic data on pure tricalcium silicate polymorphs[1]

Polymorph	Melting/ transformation temp. (°C)	Structure	a	b	c	α	β	γ
R	2,070	Rhombohedral	7.15	-	25.56	90.00	90.00	120.00
M_3	1,060	Monoclinic	33.08	7.03	18.50	90.00	94.12	90.00
M_2	1,050	Pseudohexagonal	7.13	7.14	25.13	90.00	90.00	120.06
		Orthorhombic	12.34	7.14	25.13	90.00	90.00	90.00
M_1	990	Pseudohexagonal	7.12	7.14	25.42	89.95	90.13	120.08
		Monoclinic	14.23	7.14	25.42	90.00	90.13	90.00
T_3	980	Triclinic	14.23	14.29	25.41	89.94	90.15	120.05
T_2	920	Triclinic	14.20	14.28	25.36	90.00	90.17	120.04
T_1	600	Triclinic	14.14	14.28	25.29	90.10	90.21	120.02

Belite (C_2S) is the second most importance clinker mineral which presents in a range of 10-40% in Portland clinker. It is a dicalcium silicate ($2CaO \cdot SiO_2$). Belite can be found in five distinct polymorphs, each with its own unique properties: three α, one β, and one γ forms. Belite undergoes several phase transformations as follows:

$$\alpha \xleftrightarrow{1{,}425\ ^{\circ}C} \alpha'_H \xleftrightarrow{1{,}160\ ^{\circ}C} \alpha''_L \xleftrightarrow{630\text{-}680\ ^{\circ}C} \beta \xleftrightarrow{<500\ ^{\circ}C} \gamma$$

The hydraulically important polymorph in Portland cement being β-C_2S, which can be obtained by quenching or crystallo-chemical doping. The transformation at lower temperature forms γ- C_2S (non-hydraulic), which is known as "dusting" due to a volume increase. In Portland cement clinker, it is possible to have distinct belite origins originating from different sources:

Primary belite is created when lime and silicon sources react.

Secondary belite is generated when alite decomposes according to the formula $C_3S \rightarrow C_2S + C$

Tertiary belite is formed as a result of the recrystallization of the interstitial phase formed by the breakdown and decrease in solid solution of SiO_2 in the C_3A phase.

Tricalcium aluminate (C_3A) constitutes of 5-10% of Portland clinker. In general, the cubic and/or orthorhombic structure of tricalcium aluminate phase exists. This phase has a significant effect on the early set characteristics due to its quick hydration, which requires retardation, which is typically accomplished by the addition of gypsum.

Ferrite (C_4AF) consists of 5-15% of normal Portland clinker. Among the ternary phases in the system, ferrite is the sole one. Portland cement's gray color is caused by the presence of an iron-rich phase in the mix. When it comes to amount, ferrite and tricalcium aluminate are very close in comparison.

2.1.3 Finenss

Along with its chemical composition, the fineness of cement has an effect on its reactivity with water. In general, the finer the cement, the faster it reacts. For a given compound composition, finer grinding of cement can increase the pace of reactivity and hence the strength development; nevertheless, the expense of grinding and the heat generated during hydration impose some limitations on the fineness.

Fineness is easily evaluated in the cement industry for quality control purposes by the residue on standard sieves such as No. 200 mesh (75 μm) and No. 325 mesh (45 μm). It is well accepted that cement particles greater than 45 m hydrate slowly, and those larger than 75 m may never entirely hydrate. However, without knowledge of the whole particle size distribution, it is impossible to assess the relative reactivity of cements with identical component compositions. Due to the difficulty or expense of determining the particle size distribution, it is a standard practice in the industry to get a relative measure of the particle size distribution from the surface area measurement of the cement using the Blaine Air Permeability Method (ASTM C 204). The particle size distribution and Blaine surface area of two industrially manufactured Portland cement samples are depicted in Figure 2.

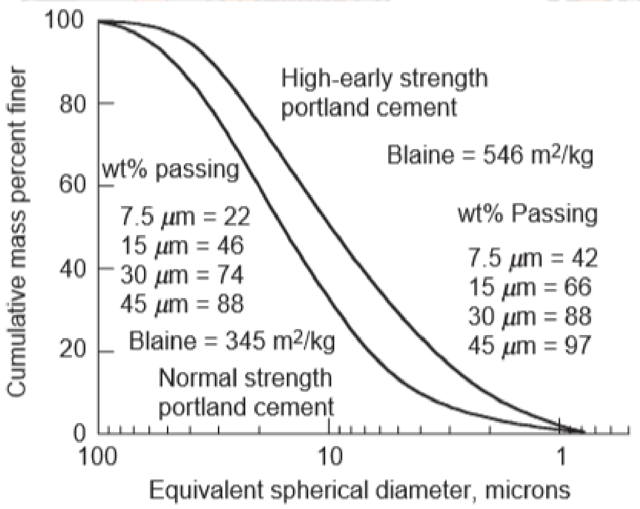

Figure 2 Particle size distribution data for Type I and III Portland cement.

2.1.4 Hydration of Portland cement

Due to the fact that Portland cement is a heterogeneous combination of many compounds, the hydration process is characterized by simultaneous interactions of the anhydrous components with water. However, not all chemicals hydrate uniformly. It is well established that aluminates hydrate substantially more rapidly than silicates. Indeed, the stiffening (loss of consistency) and setting (solidification) features of

Portland cement paste are substantially governed by the aluminates' hydration processes.

Silicates, which account for approximately 75% of typical Portland cement, are critical in defining the hardening (pace of strength growth) features of the material. To have a thorough knowledge of the chemical and physical changes that occur during Portland cement hydration, it is necessary to discuss the hydration processes of aluminates and silicates individually.

2.1.4.1 Hydration of tricalcium aluminate

C_3A reacts immediately with water. Crystalline hydrates, such as C_3AH_6, C_4AH_{19}, and C_2AH_8, develop rapidly, releasing a significant amount of hydration heat. Portland cement cannot be used in the majority of construction applications unless the quick hydration of C_3A is slowed in some way. Generally, this operation is achieved with the addition of gypsum. Thus, for practical purposes, it is not the hydration reactions of C_3A alone that are significant, but the hydration reactions of C_3A in the presence of gypsum.

When gypsum is present, the amount of tricalcium aluminate hydrate consumed during the early stage of hydration is significantly reduced when compared to when $CaSO_4$ is not present. The primary result of the hydration of tricalcium aluminate with $CaSO_4$ was ettringite.

$$C_3A + 3CSH_2 + 26H \xrightarrow{fast} C_6AS_3H_{32}$$

Ettringite is used to generate a coating on the surface of tricalcium aluminate that functions as a barrier, slowing down the tricalcium aluminate reaction and preventing the creation of monosulfate.

$$2C_3A + C_6AS_3H_{32} + 4H \xrightarrow{slow} 3C_4ASH_{12}$$

2.1.4.2 Hydration of ferrite

Ferrite hydrates similarly to tricalcium aluminate, but more slowly. Ferrite is far more severely slowed than tricalcium aluminate by the addition of gypsum or a mixture of gypsum and lime.

2.1.4.3 Hydration of calcium silicate

Rapid hydration of the alite helps to the formation of the cement. Approximately 40% of alite reacts within a day, approximately 70% within 28 days, and practically all within a year. Calcium silicate hydrate (C-S-H) and calcium hydroxide are formed when alite interacts with water.

$$nCaO\cdot SiO_2 + (n - x - y)H_2O \rightarrow xCaO\cdot SiO_2\cdot yH_2O) - (n - x)Ca(OH)_2$$

Belite undergoes the same hydration mechanism as alite, although the rate of hydration is significantly slower. While hydration of belite contributes little to early strength development, it is primarily important for long-term strength growth.

During the first few days, the rate of hydration is $C_3A > C_3S > C_4AF > C_2S$. Figure 3 illustrates the rate of hydration. The strength development of several minerals is depicted in Figure 4. As can be observed, C_3S has a high initial strength, whereas C_2S builds its strength slowly at first but rapidly later age. It may be determined that C_3S contributes the most to the early strength of Portland cement, whereas C_2S provides the most to the long-term strength. On the other hand, C_3A and C_4AF provide a negligible addition to the strength of Portland cement. Additionally, the strength development and kinetics of many minerals are related in some way although not very closely.

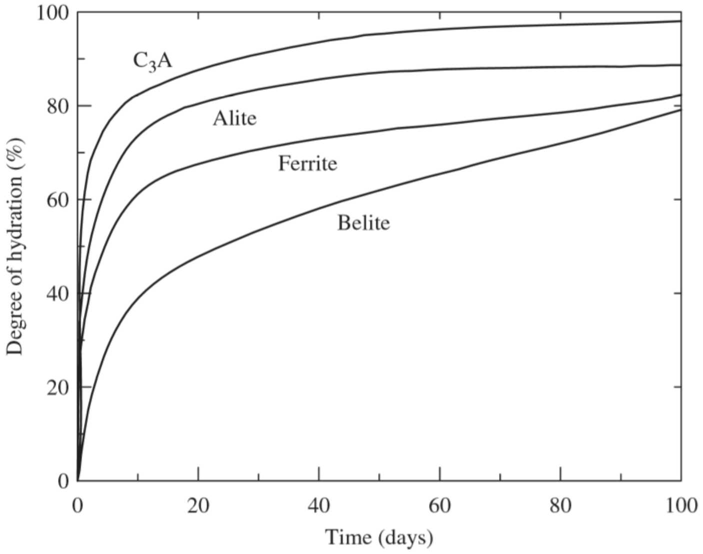

Figure 3 Process of hydration of the Portland cement's basic ingredients

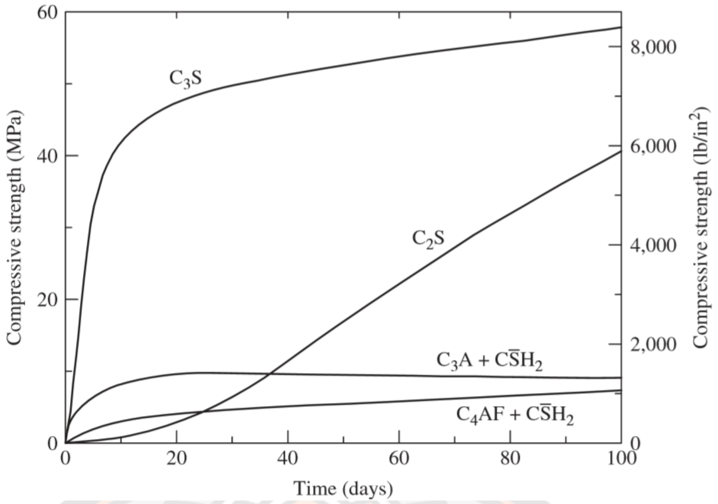

Figure 4 Development of the strength of Portland cement's major ingredients

2.2 Calcium sulfoaluminate cement (CSA)

2.2.1 Introduction

Calcium sulfoaluminate (CSA) cement is one kind of alternative binder instead of Ordinary Portland Cement (OPC) because CSA cement is synthesized at a temperature around 1,250 °C and 1,450 °C of OPC as well as the reduction of CO_2 emission during CSA cement production when compared with OPC. CSA cement has been produced mainly in China and firstly developed in 1,960s[8]. The raw materials used to from CSA are limestone, gypsum, and bauxite. The main chemical composition of CSA clinker consists of belite, tetracalcium trialuminate sulfate ($C_4A_3\overline{S}$ also known as ye'elimite) and gypsum. CSA cements are available with a range of qualities, including strong early strength, rapid setting, shrinkage compensation, and self-stressing.

2.2.2 Phase composition

CSA includes some of the same phase composition contained in OPC: belite (C_2S), ferrite (C_4AF), Calcium sulfate ($C\overline{S}$) and Ye'elimite ($C_4A_3\overline{S}$). In CSA compound, ye'elimite is substituted for alite due to the formation of alite is after 1,350 °C and the decomposition of ye'elimite ($C_4A_3\overline{S}$) occurs when the temperature exceeds 1,300 °C. Ye'elimite reduces carbon dioxide formation and give early strength instead of alite. Besides, the clinker is soft and makes grinding easier. Ye'elimite manufacturing requires calcium, sulfate, and alumina, the latter of which requires bauxite.

2.2.3 Hydration of calcium sulfoaluminate cement

The hydration of Ye'elimite with calcium sulfate ($C\bar{S}$), resulting in the lead to the formation of ettringite ($C_6A\bar{S}_3H_{32}$) and gibbsite (AH_3). Without calcium sulfate ($C\bar{S}$), monosulfate($C_4A\bar{S}H_{12}$) is formed instead of ettringite ($C_6A\bar{S}_3H_{32}$). However, monosulfate formation does not cause expansion and show little to strength development. The hydration product of belite such as calcium hydroxide (portlandite) and combined with ye'elimite and calcium sulfate, the result shows more amount of ettringite ($C_6A\bar{S}_3H_{32}$). The formation of ettringite promote early strength of CSA cement and the long-term strength is received by the reaction of belite (C_2S), C-S-H and CH are the hydration products.

$$C_4A_3\bar{S} + 2CS + 38H \rightarrow C_6A\bar{S}_3H_{32} + 2AH_3$$

$$C_4A_3\bar{S} + 18H \rightarrow C_4A\bar{S}H_{12} + 2AH3$$

$$C_4A_3\bar{S} + 6CH + 8CS + 90H \rightarrow 3C_6A\bar{S}_3H_{32}$$

The mechanical qualities of this type of cement are determined by the proportion of $C_4A_3\bar{S}$ and minor phases in the clinker, as well as the amount of sulfate present. Indeed, the inclusion of 15–25% calcium sulfate by weight aids in the regulation of setting time, strength development, and volume stability. CSA cement performs similarly to OPC cement in terms of compressive and flexural strength, but in a shorter time frame. Indeed, CSA cement reaches 75% of its full strength in 24 hours, compared to around 40% for OPC. The primary physical properties of CSA cement are its extremely high early strength (about 35 MPa after 24 hours and approximately 60 MPa after 28 days), low permeability, great resistance to sulfates and corrosion, and regulated expansion. Due to their short working period, set retarding admixtures may be required to increase the amount of time available for placement and finishing, as well as to improve long-term strength, durability, and consistency. Due to the rapid development of ettringite, expansion, and low alkalinity of this type of cement, it may be useful in other applications such as "self-leveling screeds, self-leveling topping mortars, and high-performance glass-fiber-reinforced composites." Due to the low pH (in comparison to OPC), low porosity, and hydrate's tendency to bind heavy metals, CSA cement may potentially be utilized in hazardous waste encapsulation. The advantages and disadvantages of OPC and CSA cement are presented in Table 2.

Table 2 The benefits and drawbacks of OPC and CSA cements

Type of cement	OPC	CSA cement
benefits	- The C_3S phase - Processes that are extremely well-known	- The $C_4A_3\bar{S}$ phase - fired at temperature of 1,250 °C - emits low CO_2 - Low energy consumption - Early strength is really important
drawbacks	- Emits high CO_2 - Fired at high temperature of 1,450 °C	- Expansive - Particular application - Experts are required to operate it, due to rapid hydration

2.3 Alite calcium sulfoaluminate cement (ACSA cement)

2.3.1 Related theoretical with ACSA cement

Alite calcium sulfoaluminate cement is one type of calcium sulfoaluminate cement, which is developed to combine the main phases composition of OPC and CSA cement such as alite, belite and ye’elimite. Alite-calcium sulfoaluminate cement provides both early strength and late strength. Incorporating of alite and ye’elimite is challenging during clinkerization, the decomposition of ye’elimite ($C_4A_3\bar{S}$) occurs when the temperature exceeds 1,300 °C [17, 18], while the ideal formation of alite is about 1,450 °C [1]. Fortunately, this problem can be solved by the addition of some additive in raw materials. These could lower formation of alite, promote the coexistence of alite and ye’elimite which then increased the strength of the clinker.

2.3.2 Effect of additive for alite formation

Natechanok et al.[50] synthesized alite-calcium sulfoaluminate clinker by using 72.5% limestone, 16.9% tuff and 10.6% gypsum as raw materials. 1 % of calcium fluoride is used for additive. The clinker was produced by firing at 1,300 C for 45 min, then the clinker was ground and mixed with anhydrite for 5 %. Alite-calcium sulfoaluminate clinker with a phase composition of roughly 50% alite and 10% ye'elimite. Figure 5 shown the XRD pattern of anhydrous clinker also exhibits the incorporating of alite and ye’elimite. C-S-H, ettringite, monosulfate, and portlandite are the major hydration products. The compressive strength of mortar rapidly develops, which shows approximately 35 MPa at 28 d.

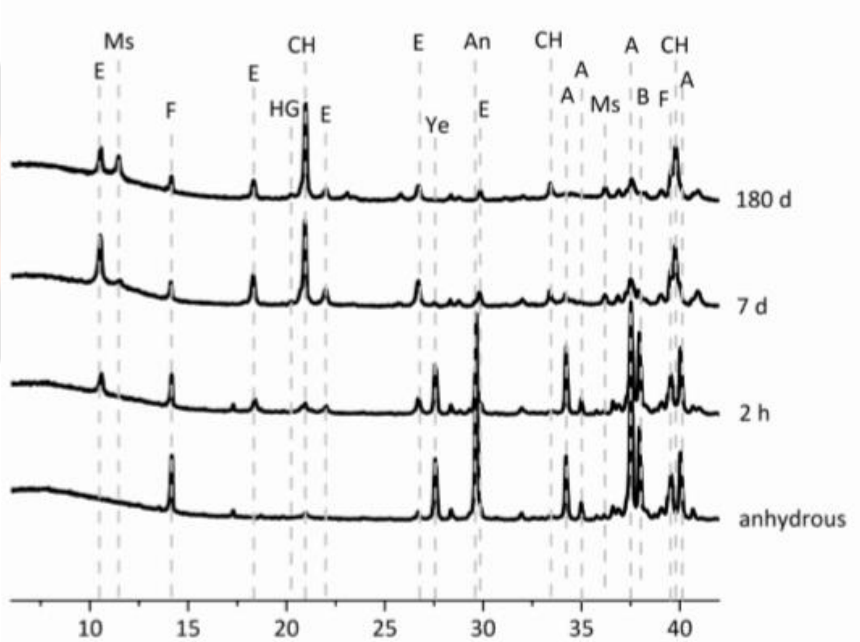

Figure 5 XRD patterns of anhydrous ACSA and after 2 h, 7 d and 180 d of hydration. (E – ettringite, Ms – monosulfate, F ferrite, HG – iron-containing siliceous hydogranet, CH – portlandite, Ye – ye’elimite, An – anhydrite, A – alite and

B - belite)[50]

A.G. De la Torre et al.[16] produce belite-alite-ye’elimite (BAY) cement, which is a combination of alite and ye’elimite in this cement. Table 3 shows the clinker preparation including natural limestone, sand, iron oxide, kaolin, and gypsum. Researcher design four targeted phase composition of clinker and using 0.9 % of CaF_2

of the amount of oxides after carbonation in the raw materials. The sample was heated at 900 °C for 30 minutes by a heating rate of 5 °C/minute. Then, the temperature was raised at the same rate to 1,300 °C and held for 15 minutes. Finally, the clinker was quenched by using forced air convection to room temperature. Table 4 exhibits the result from Reitveld refinement technique by XRD pattern of BAY_1, BAY_2, BAY_3, BAY_4. The mixture of BAY_4 was scale-up due to containing maximum percentages of alite and ye’elimite, respectively. The scale-up sample was fired at 3 condition of final temperature, shown in Table 5, which found that the sample heated at 1,300 °C for 15 minutes exhibit maximum of alite, but the amount of ye’elimite show only 5.2 % due to the loss of SO_3. This problem promotes the formation of mayenite($C_{12}A_7$) and tricalcium aluminate (C_3A). However, a problem was solved by add excess of sulfur to raw materials to compensate for the loss of sulfur. The result shows the increment of ye’elimite, which mayenite($C_{12}A_7$) and tricalcium aluminate (C_3A) were decreased. The sc-BAY_4 was prepared to mortar by using w/c of 0.4 and 0.5, then compared with belite-ye’elimite-ferrite cement (BYF) by using w/c 0.55. Finally, sc-BAY_4 mortar show higher compressive strength for approximately 34 MPa at 28 days by using w/c of 0.4.

Table 3 Targeted mineralogical phase assemblage of BAY clinkers, raw materials dosages and nominal element composition of raw mixtures.[16]

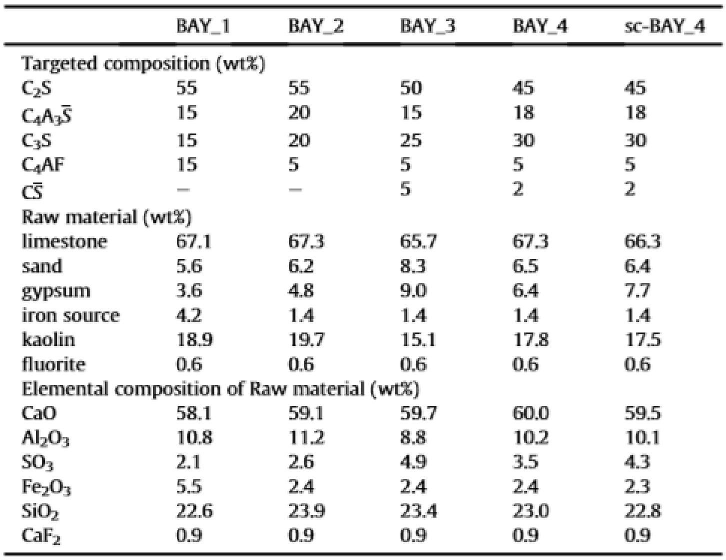

	BAY_1	BAY_2	BAY_3	BAY_4	sc-BAY_4
Targeted composition (wt%)					
C_2S	55	55	50	45	45
$C_4A_3\bar{S}$	15	20	15	18	18
C_3S	15	20	25	30	30
C_4AF	15	5	5	5	5
$C\bar{S}$	–	–	5	2	2
Raw material (wt%)					
limestone	67.1	67.3	65.7	67.3	66.3
sand	5.6	6.2	8.3	6.5	6.4
gypsum	3.6	4.8	9.0	6.4	7.7
iron source	4.2	1.4	1.4	1.4	1.4
kaolin	18.9	19.7	15.1	17.8	17.5
fluorite	0.6	0.6	0.6	0.6	0.6
Elemental composition of Raw material (wt%)					
CaO	58.1	59.1	59.7	60.0	59.5
Al_2O_3	10.8	11.2	8.8	10.2	10.1
SO_3	2.1	2.6	4.9	3.5	4.3
Fe_2O_3	5.5	2.4	2.4	2.4	2.3
SiO_2	22.6	23.9	23.4	23.0	22.8
CaF_2	0.9	0.9	0.9	0.9	0.9

Table 4 RQPA (wt%) for BAY clinkers.[16]

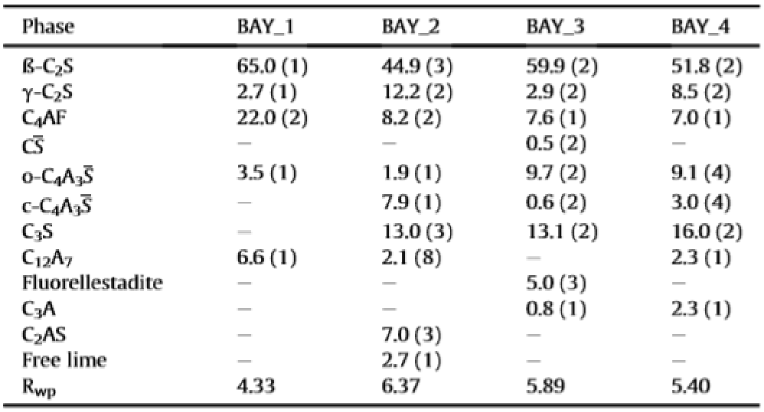

Phase	BAY_1	BAY_2	BAY_3	BAY_4
ß-C_2S	65.0 (1)	44.9 (3)	59.9 (2)	51.8 (2)
γ-C_2S	2.7 (1)	12.2 (2)	2.9 (2)	8.5 (2)
C_4AF	22.0 (2)	8.2 (2)	7.6 (1)	7.0 (1)
$C\overline{S}$	–	–	0.5 (2)	–
o-$C_4A_3\overline{S}$	3.5 (1)	1.9 (1)	9.7 (2)	9.1 (4)
c-$C_4A_3\overline{S}$	–	7.9 (1)	0.6 (2)	3.0 (4)
C_3S	–	13.0 (3)	13.1 (2)	16.0 (2)
$C_{12}A_7$	6.6 (1)	2.1 (8)	–	2.3 (1)
Fluorellestadite	–	–	5.0 (3)	–
C_3A	–	–	0.8 (1)	2.3 (1)
C_2AS	–	7.0 (3)	–	–
Free lime	–	2.7 (1)	–	–
R_{wp}	4.33	6.37	5.89	5.40

Table 5 RQPA (wt%) for sc-BAY_4 clinker at different thermal cycles.[16]

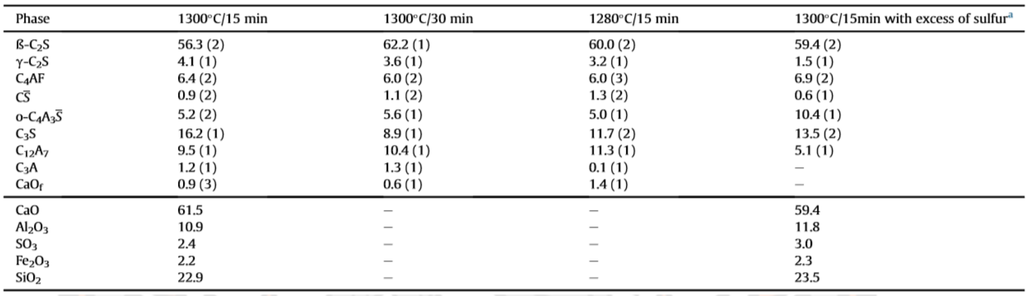

Phase	1300°C/15 min	1300°C/30 min	1280°C/15 min	1300°C/15min with excess of sulfur[a]
ß-C_2S	56.3 (2)	62.2 (1)	60.0 (2)	59.4 (2)
γ-C_2S	4.1 (1)	3.6 (1)	3.2 (1)	1.5 (1)
C_4AF	6.4 (2)	6.0 (2)	6.0 (3)	6.9 (2)
$C\overline{S}$	0.9 (2)	1.1 (2)	1.3 (2)	0.6 (1)
o-$C_4A_3\overline{S}$	5.2 (2)	5.6 (1)	5.0 (1)	10.4 (1)
C_3S	16.2 (1)	8.9 (1)	11.7 (2)	13.5 (2)
$C_{12}A_7$	9.5 (1)	10.4 (1)	11.3 (1)	5.1 (1)
C_3A	1.2 (1)	1.3 (1)	0.1 (1)	–
CaO_f	0.9 (3)	0.6 (1)	1.4 (1)	–
CaO	61.5	–	–	59.4
Al_2O_3	10.9	–	–	11.8
SO_3	2.4	–	–	3.0
Fe_2O_3	2.2	–	–	2.3
SiO_2	22.9	–	–	23.5

Tristana Duvallet et al.[21] study the influence of high-iron on alite-calcium sulfoaluminate-ferrite cement. Even while the ferrite phase is not known to contribute significantly to the strength development of OPC, when mixed with belite and ye'elimite, it can create a high compressive strength. Five compositions containing varying amounts of ferrite as the target phase, ranging from 5% to 50% by weight, were generated using industrial by-products such as hydrated lime, bottom ash, red mud, bauxite, blast furnace slag fines, and class C fly ash shown in Table 6. The modified Bogue equations are used to determine the chemical composition.

Table 6 The five theoretical clinker composition with three modulus values.[21]

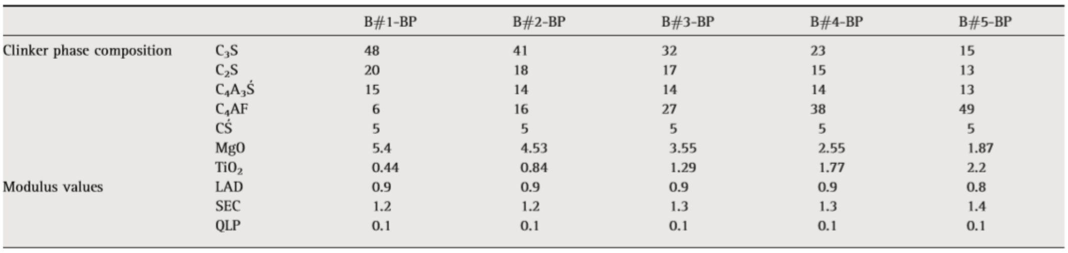

		B#1-BP	B#2-BP	B#3-BP	B#4-BP	B#5-BP
Clinker phase composition	C_3S	48	41	32	23	15
	C_2S	20	18	17	15	13
	$C_4A_3\acute{S}$	15	14	14	14	13
	C_4AF	6	16	27	38	49
	$C\acute{S}$	5	5	5	5	5
	MgO	5.4	4.53	3.55	2.55	1.87
	TiO_2	0.44	0.84	1.29	1.77	2.2
Modulus values	LAD	0.9	0.9	0.9	0.9	0.8
	SEC	1.2	1.2	1.3	1.3	1.4
	QLP	0.1	0.1	0.1	0.1	0.1

The raw mixed were fired at 800 °C for 30 minutes, then heated to 1,250 – 1,300 °C and hold at 30 or 60 minutes. All composition and firing temperature were tested by XRD and shows the result in Figure **6**, which some samples have a prominent peak that appears to be unreacted free lime. Furthermore, tricalcium aluminate was discovered to be present. due to ye'elimite peak is clearly observed as decomposes to tricalcium aluminate and calcium sulfate. For batches #2 through #5, the optimal firing temperature of 1,250 °C for 60 minutes was determined, but batch #1 formed best at 1,275 °C for 60 minutes. This finding indicates that the composition with a low concentration of ferrite must heat to a greater temperature.

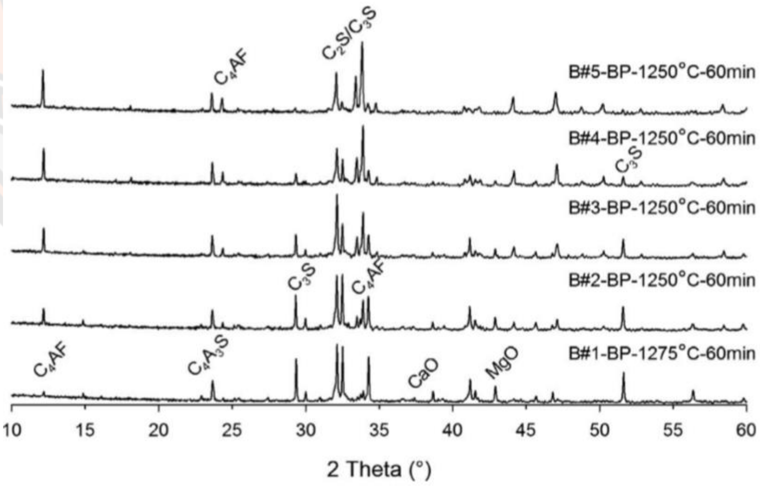

Figure **6** Optimal firing regimes for each composition as determined by XRD graphs [21]

Suhua Ma et al.[26] is particularly interested in the effect of CuO on the development and coexistence of alite and ye'elimite. The limestone, clay, gypsum and fly ash were used as starting raw materials. XRF analysis of the raw meal revealed its chemical composition: 43.35% of CaO, 1.16% of Fe_2O_3, 3.71% of Al_2O_3, 2.16% of

SO_3, 13.70% of SiO_2 and 34.41% for Loss. The CuO content was added to the sample for 0 %, 0.1 %, 0.3 %, 0.5 % and 1 % by named as D_0, D_{C1} to D_{C4}. The burn-ability of clinker was investigated by firing to 1,300 °C, 1,350 °C and 1,400 °C, which show free lime content decrease when CuO content increased.

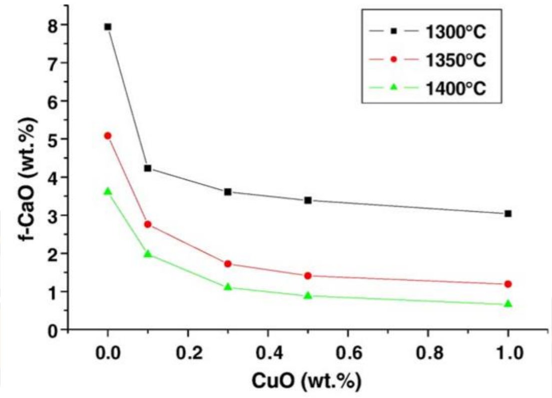

Figure 7 The influence of copper oxide concentration on the free lime content of clinker.[26]

The thermal analysis results processed by DTA technique. The sample containing 1 % of CuO shown the formation of strong peak of the liquid phase and found peak at a lower temperature than the sample without CuO (1,241 °C of 1 % CuO and 1,274 °C of without CuO). Additionally, it demonstrates that CuO can lower the liquid phase's formation temperature.

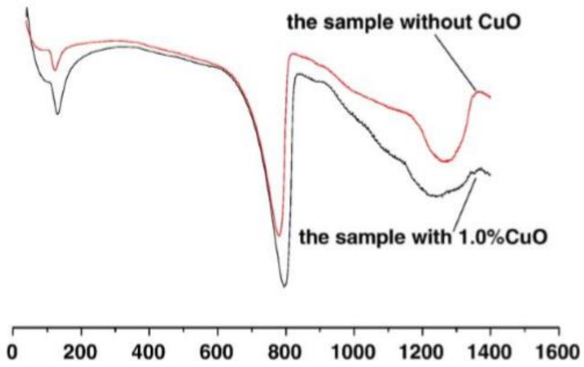

Figure 8 The DTA curves for samples devoid of CuO and those containing 1.0 percent CuO.[26]

From the result of XRD pattern found the influence of additive on the formation of ye’elimite that the sample with 1 % CuO has shown the lower formation of ye’elimite by about 50 °C at temperature range 1,150 °C – 1,250 °C. Whereas tricalcium aluminate was presented at 1,300 °C due to ye’elimite mineral decomposes to tricalcium aluminate and calcium sulfate. As a result, an excess of CuO is unfavourable to the coexistence of alite and ye'elimite. The greatest concentrations of alite and ye'elimite in clinker at 1,300 °C are observed in a sample containing 0.1 percent CuO.

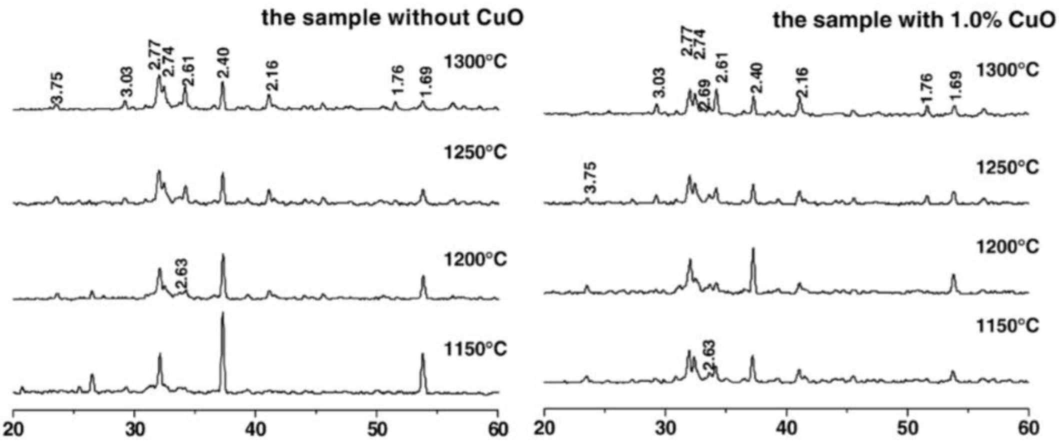

Figure **9** The XRD for samples devoid of CuO and those containing 1.0 percent CuO.[26]

Table 7 The clinker's alite and ye'elimite constituents burnt at a temperature of 1,300 °C.[26]

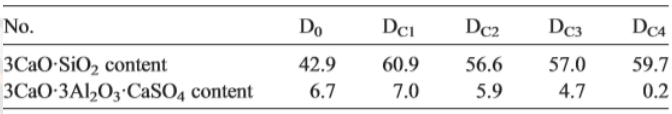

No.	D_0	D_{C1}	D_{C2}	D_{C3}	D_{C4}
$3CaO \cdot SiO_2$ content	42.9	60.9	56.6	57.0	59.7
$3CaO \cdot 3Al_2O_3 \cdot CaSO_4$ content	6.7	7.0	5.9	4.7	0.2

At 1,300 °C, Weifeng Li et al.[51] synthesized alite-ye'elimite clinker utilizing limestone, sandstone, fly ash, and gypsum as raw materials. This research interested to use oxide of phosphorus (P_2O_5) and copper (CuO) as an additive by using phosphorus slag and copper slag for the source of that oxide. The raw mixed prepared by 70.7% limestone, 7.2% sandstone, 8.9% fly ash, 9.7 % gypsum, 1.2 % copper slag and 2.3 % phosphorus slag. For 60 minutes, an electric furnace was used to heat the raw material to 1,300 degrees Celsius. The clinker was investigated and compared with Ordinary Portland cement (OPC). The phases composition of clinker found that alite was able to form at 1,300 °C for 41.6 %. The amount of ye’elimite shown about 1.3% and found the formation of tricalcium aluminate of 7.2 %, which may occur by decomposes of ye'elimite. The compressive strength exhibits around 62 MPa, while OPC has shown 56 MPa at 28 days.

Table 8 Analyses of the chemical composition and phase composition of ACSA clinker and OPC utilized.[51]

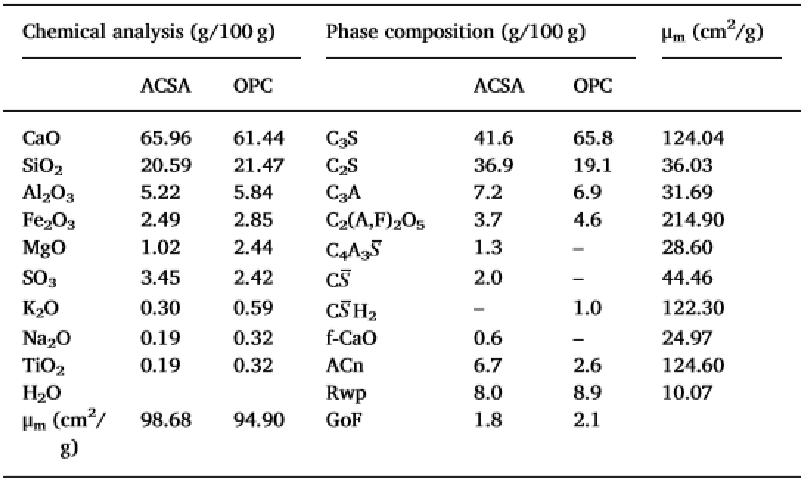

Chemical analysis (g/100 g)			Phase composition (g/100 g)			μ_m (cm^2/g)
	ACSA	OPC		ACSA	OPC	
CaO	65.96	61.44	C_3S	41.6	65.8	124.04
SiO_2	20.59	21.47	C_2S	36.9	19.1	36.03
Al_2O_3	5.22	5.84	C_3A	7.2	6.9	31.69
Fe_2O_3	2.49	2.85	$C_2(A,F)_2O_5$	3.7	4.6	214.90
MgO	1.02	2.44	$C_4A_3\overline{S}$	1.3	–	28.60
SO_3	3.45	2.42	$C\overline{S}$	2.0	–	44.46
K_2O	0.30	0.59	$C\overline{S}H_2$	–	1.0	122.30
Na_2O	0.19	0.32	f-CaO	0.6	–	24.97
TiO_2	0.19	0.32	ACn	6.7	2.6	124.60
H_2O			Rwp	8.0	8.9	10.07
μ_m (cm^2/g)	98.68	94.90	GoF	1.8	2.1	

The effect of magnesium oxide on alite-sulfoaluminate cement was examined by Xiaocun Liu et al.[52]. The target phases were designed as 5 % alite, 30 % belite, 15 % ye'elimite, 5 % ferrite and 5 % calcium sulfate. The raw mixture was made using analytically pure ingredients such as $CaCO_3$, SiO_2, Al_2O_3, $CaSO_42H_2O$, and Fe_2O_3, which were combined with 0.25 percent CaF_2 and varying amounts of MgO.

Table 9 MgO concentration in clinker (wt.%).[52]

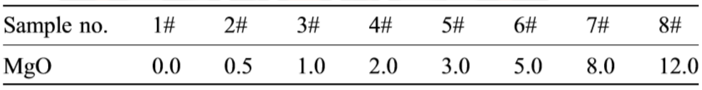

Sample no.	1#	2#	3#	4#	5#	6#	7#	8#
MgO	0.0	0.5	1.0	2.0	3.0	5.0	8.0	12.0

The three firing temperatures were processed for 60 minutes at 1,200 °C, 1,250 °C, 1,300 °C and then removed from the furnace and cooled rapidly in air. The burnability of clinker was determined using the free lime content, and it was discovered that when the MgO content is between 0.5 and 3%, the free lime content tends to decrease. When the MgO level is greater than 3%, the free lime content tends to increase.

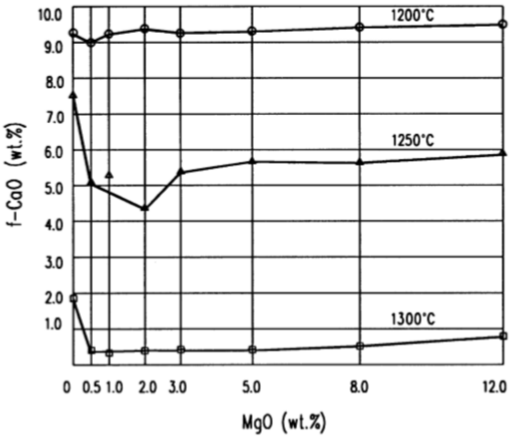

Figure 10 The concentration of free lime in clinkers as a function of MgO.[52]

Figure 11 illustrates the XRD patterns of clinker burned at 1300°C. When the MgO level of the clinkers exceeds 3.0%, the periclase phase forms. XRD peak intensities of several samples are compared, and it can be noticed that alite without MgO has lower peak intensities when compared to the other samples. The formation of alite, on the other hand, increases significantly when the amount of MgO added is 0.5 percent. Increased amounts of alite can be found in the clinkers when MgO concentrations range from 2.0 percent to 5.0 percent. This reveals that the presence of MgO is advantageous to the coexistence of alite and ye'elimite.

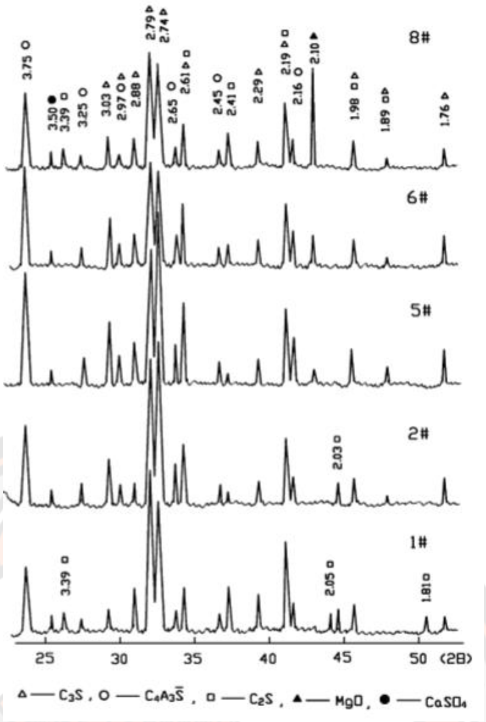

Figure 11 XRD patterns of clinkers with addition of MgO.[52]

2.4 Piezoelectricity theory

Piezoelectricity was derived directly from the Greek term "piezein," which translates as "pressure electricity." Jacques and Pierre Curie developed piezoelectricity in 1880. They discovered electricity when some crystals, including tourmaline, quartz, topaz, cane sugar, and Rochelle salt, were subjected to mechanical strain. This phenomenon was separated from others of a similar kind, such as "contact electricity" (friction-generated static charge). A crystal must lack a center of symmetry in order to exhibit the piezoelectric effect. The direct piezoelectric effect is described as a proportionate change in electric polarization due to strain. If external mechanical stress induces dielectric displacement in a material, the material is said to be piezoelectric. Closely related is the converse phenomenon, which occurs when an external electric field is supplied to a piezoelectric crystal [53, 54].

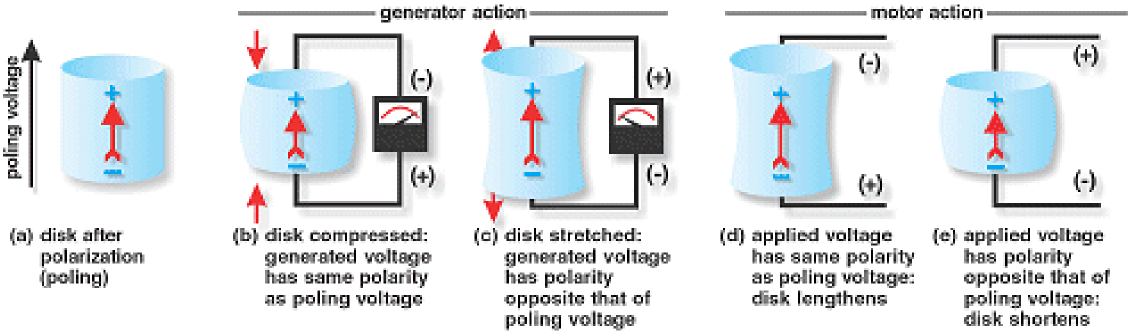

Figure 12 Piezoelectric material's direct and indirect effects on voltage generation and shape change when voltage is applied. [55]

Crystallographers use four types of symmetry to define symmetry about a point in space, such as the central point of a unit cell: (1) a center of symmetry, (2) rotation axes, (3) mirror planes, and (4) combinations of these. Using these symmetry factors, all crystals can be classified into 32 distinct classes or point groups, as illustrated in Figure 13. These 32-point groups correspond to seven fundamental crystal systems: triclinic, monoclinic, orthorhombic, tetragonal, rhombohedral (trigonal), hexagonal, and cubic. Twenty-one of these classes are noncentrosymmetric (a required condition for the existence of piezoelectricity), and twenty of them are piezoelectric. Despite the absence of a center of symmetry, one class is not piezoelectric due to the presence of additional coupled symmetry elements. There are ten crystal classifications classed as pyroelectric out of a possible twenty. This class of materials is remarkable in that it is permanently polarized within a specified temperature range. In contrast to the more general piezoelectric classes, which create polarization in response to stress, pyroelectrics acquire polarization spontaneously and form permanent dipoles within the structure. Ferroelectrics are a particularly unusual class of materials that are a subgroup of spontaneously polarized pyroelectrics. Similar to pyroelectrics, materials in this group exhibit spontaneous dipoles; however, unlike pyroelectrics, these dipoles are reversible in the presence of an electric field several orders of magnitude smaller than the material's dielectric breakdown. There are four forms of ceramic ferroelectrics: (1) tungsten–bronze, (2) oxygen octahedral, (3) pyrochlore, and (4) bismuth layer–structure. Economically, the second category

(ABO_3 perovskite type) is far and away the most important. The composition families described above ($BaTiO_3$, PZT, PLZT, PT (lead titanate), PMN, and (Na, K)NbO_3) account for the vast majority of ferroelectric ceramics created today [53, 54].

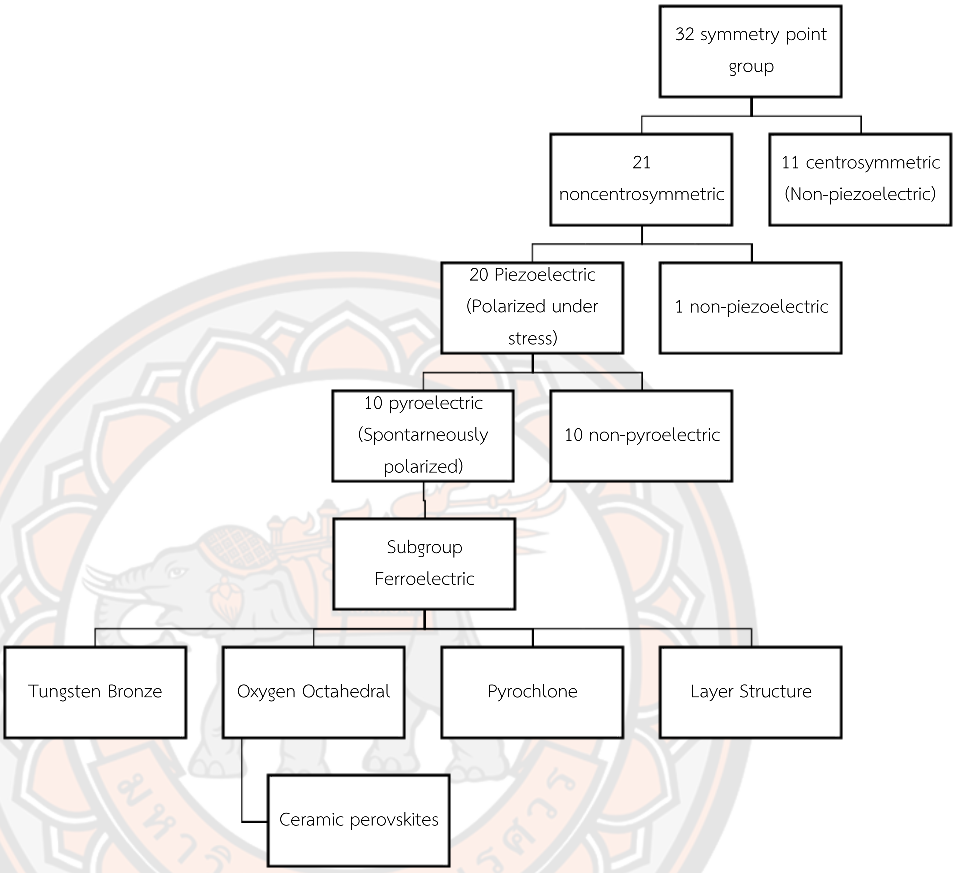

Figure 13 Classification of the 32 crystallographic crystal classes.

A traditional piezoelectric ceramic is perovskite crystal. The perovskite structure has the general chemical formula ABO_3, where O is oxygen in the centers of the faces, A denotes a cation with a larger ionic radius at the corners, while B denotes a cation with a smaller ionic radius in the body center. Each crystal possesses a dipole moment when it is subjected to conditions that impart tetragonal or rhombohedral symmetry on it [53, 54].

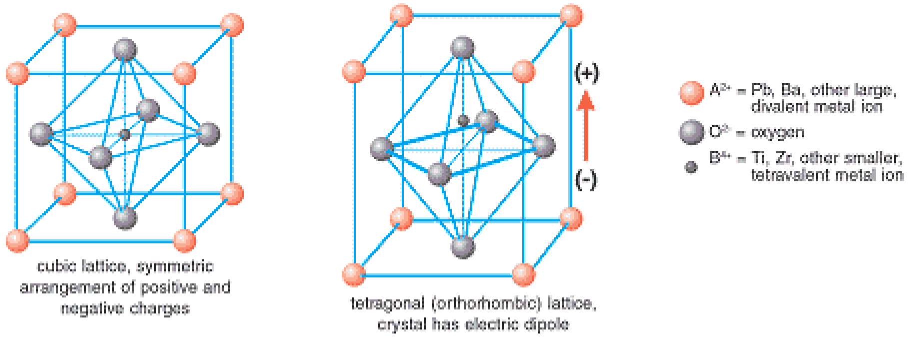

Figure 14 Traditional piezoelectric ceramic crystal structure, above and below the Curie point [55]

2.4.1 Poling

The poling process is critical in enabling the piezoelectric effect to be used in a ferroelectric ceramic. Without poling, ferroelectric does not exhibit piezoelectric properties due to the random arrangement of ferroelectric domains. At temperatures below the Curie point, when an electric field is applied, domains that are most closely aligned with the field grow at the expense of other domains. Additionally, the material will expand in the field direction. When the field is removed, the dipoles retain their approximate alignment due to residual polarization and strain. [55].

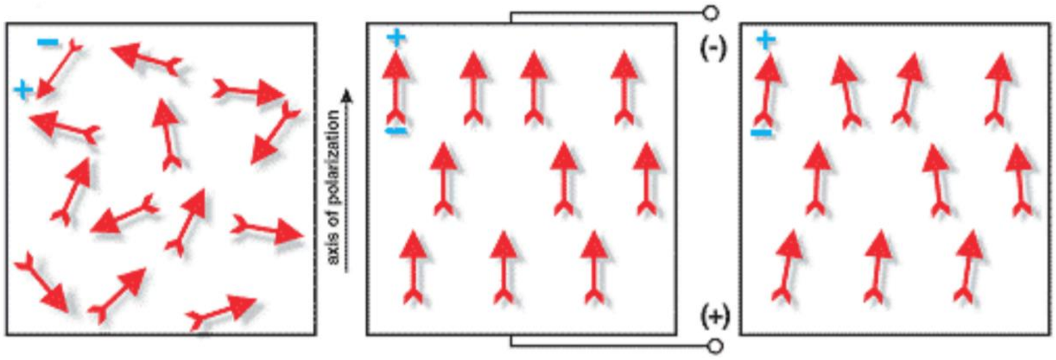

Figure 15 Left: prior to polarization, random orientation of polar domains , center: polarization of a piezoelectric ceramic, and right: polarization that remains after an electric field is removed. [55]

2.4.2 Ferroelectric properties

A ferroelectric material exhibits spontaneous polarization, in which the direction of the electric moment within can be changed by applying a field, and a hysteresis loop-shaped link between field and polarization. Valasek observed this phenomenon in 1921 using Rochelle salt. This is why, in France and Germany, ferroelectricity is frequently referred to as "Rochelle-electricity." This characteristic is exhibited only until the material reaches its Curie temperature, Tc, at which it ceases to be ferroelectric. Although the prefix "Ferro" refers to iron-based materials, ferroelectricity is not observed in these materials but was given the term due to its resemblance to ferromagnetism. Ferroelectric materials are a subgroup of piezoelectric materials that exhibit both ferroelectric and piezoelectric features.

A ferroelectric material is one in which dielectric materials can change their spontaneous polarization orientation when exposed to an external electric field. The grains in ceramic will all have a random orientation of domains in a polycrystalline ceramic, thus creating a net polarization of zero, shown by point A in Figure 16. When a DC field is given to a material, the domains are driven to align with the direction of the electric field as long as the material temperature remains below the Curie point, T_c. This increases with the applied field until a saturation point, D, where all domains that are not pinned or under internal stresses have aligned with the field. When point D is extrapolated back to zero applied field, this is the saturation point of domains, or saturation polarization, shown as P_s. The material has now undergone poling. This means that when the applied field is taken away, there will still be a net alignment of domains, known as the remnant polarization, P_r.

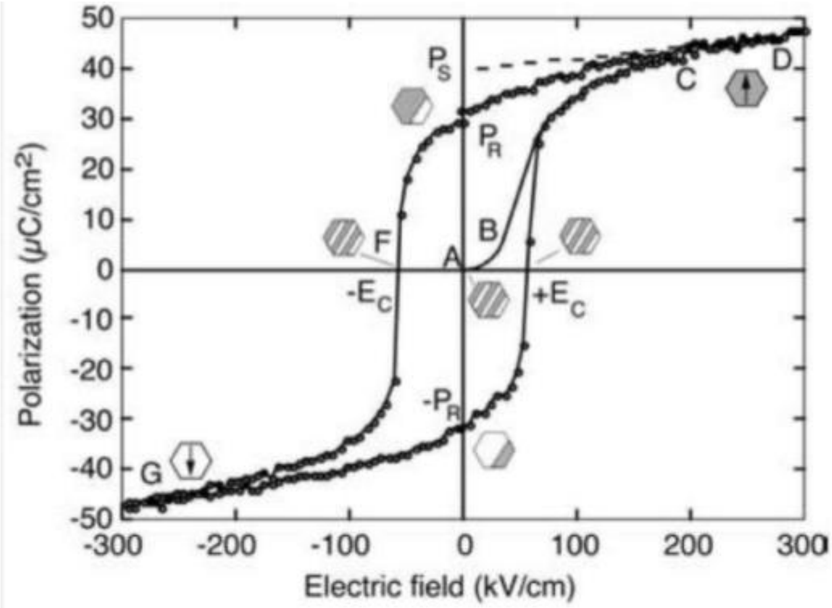

Figure 16 Schematic of typical ferroelectric P-E hysteresis loop.

2.4.3 Basic theory of dielectric and piezoelectric properties

Dielectric characteristics vary amongst solids and are dependent on temperature, field frequency, humidity, crystal structure, and other environmental factors. Additionally, the response can be linear or nonlinear in nature. Dielectric characteristics are critical practical parameters, and studying them helps us understand the fundamental properties of a material.

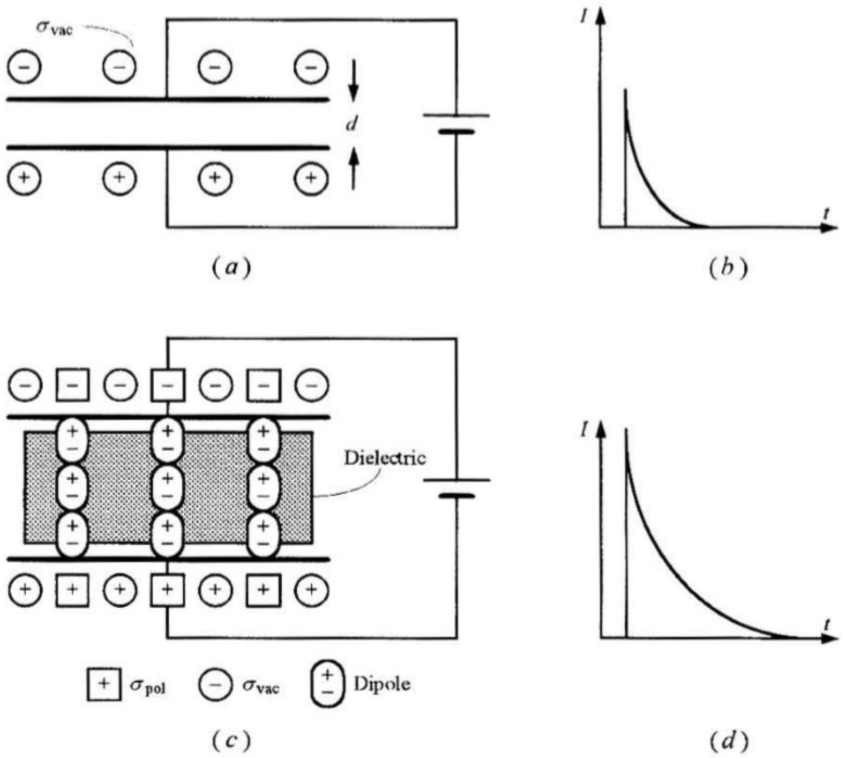

Figure 17(a) A and d parallel-plate capacitors in vacuum connected to a voltage source, (b) Circuit closure creates a brief burst of current. AUC (area under the curve) is the charge held on the capacitor. (c) Similar to (a) only a dielectric is now between the plates, (d) The charge stored on the parallel plates must be larger than the charge stored in the (b). [56]

The term "dielectric loss" (tan δ) refers to the ratio of the imaginary to the real part of the dielectric constant. Almost all uses of ferroelectric materials involve electric fields, making it important to examine their dielectric characteristics.

The piezoelectric coefficient (d_{ij}) is the amount of polarization created by a piezoelectric material per unit of mechanical stress (T). When the electric field (E) is zero, the initial subscript to d indicates the direction of polarization created in the material. The direction of the applied stress or produced strain is indicated by the second subscript.

d_{33} → Per unit force applied in direction 3 (parallel to the direction in which the ceramic element is polarized), it induced polarization in direction 3.

d_{31} → per unit force exerted in direction 1 caused polarization in direction 3 (parallel to the polarization direction of the ceramic element) (perpendicular to direction in which ceramic element is polarized)

2.4.4 Acoustic impedance

Acoustic impedance is critical for determining acoustic transmission and reflection at the interface of two materials with varying acoustic impedances, for designing ultrasonic transducers, and for determining sound absorption in a medium. The acoustic impedance of any material is calculated by multiplying its density by its velocity, and it also illustrates how a change in the impedance influences the amount of acoustic energy reflected and transmitted.

2.5 Piezoelectric materials: KNN-based piezoelectric ceramic

In civil engineering products such as tunnel linings, bridges, side slopes, stiff pavements, and some concrete structures, conventional piezoelectric materials have been employed in sensors and actuators for real-time structural health monitoring. The most often employed materials in these applications are lead-based perovskites, such as PZT-based ceramics, due to their superior electromechanical characteristics. However, the lead-free materials are interested to replace lead-containing ceramic due to that material causes pollution of the environment. At the moment, three major groups of materials are being considered: $K_{0.5}Na_{0.5}NbO_3$, $BaTiO_3$, and $Bi_{0.5}Na_{0.5}TiO_3$. However, while prior materials cannot completely replace PZT in all applications, some formulations exhibit equal or even superior qualities for specific application requirements.

2.5.1 Potassium Sodium Niobate (KNN)

KNN was first reported as a potential piezoelectric material in 1959, which occurred by $NaNbO_3$ is added to $KNbO_3$ for the stability of the perovskite structure decreases. At normal temperature, KNN exhibits a perovskite structure and has a high Curie temperature, high dielectric constant and good ferroelectric properties. The following are the primary advantages of KNN over other lead-free compositions: excellent temperature stability of piezoelectric capabilities, high mechanical quality factors, and a low density. The summary reaction of KNN is described by:

$$K_2CO_3(s) + Na_2CO_3(s) + 2\ Nb_2O_5(s) \rightarrow 4\ K_{0.5}Na_{0.5}NbO_3(s) + 2\ CO_2(g)$$

The effect of Potassium content on the dielectric properties were investigated by Seema et al[57]. The solid-state reaction technique was used to prepare $K_xNa_{1-x}NbO_3$ ceramics (where x = 0.41, 0.45, 0.48 and 0.53). The sample was calcined at 850 °C for 2 hours, then sintered at 1,150 °C for 2 hours. The result is also observed that dielectric constant increased when increasing potassium content. When x = 0.48 and 0.53 show a high value of dielectric constant by using 1 kHz and 370 °C.

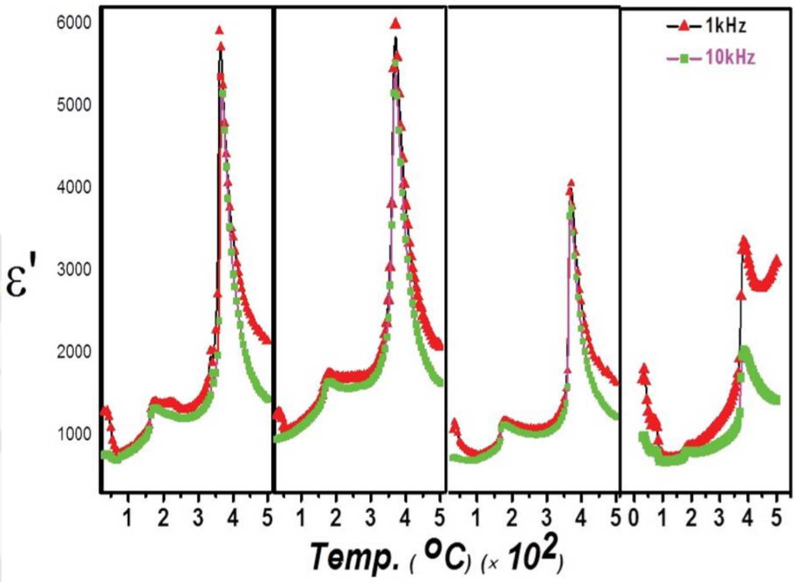

Figure 18 Variation of dielectric constant as a function of temperature of $K_xNa_{1-x}NbO_3$ (where x = 0.53, 0.48, 0.45 and 0.41) ceramic at 1 kHz and 10 kHz frequencies.[57]

Gerold A. Schneider et al.[31] studied the effect of lithium and antimony to KNN ceramic. In order to investigate dielectric and piezoelectric properties, $(K_xNa_{1-x})NbO_3$ (x = 0.31, 0.32, 0.33, 0.34, 0.35) and $(K_{0.35-1/2y}Na_{0.65-1/2y})Li_y(Nb_{1-2y}Sb_{2y})O_3$ (y = 0, 0.02, 0.04, 0.06, 0.08) were synthesized to investigate the dielectric and piezoelectric properties of the materials KNN and KNN-LS, respectively.

Calcination was carried out at a furnace temperature of 800 degrees Celsius for four hours. For one hour, KNN pellets were sintered at 1,080 and 1,100 degrees Celsius, whereas KNN-LS pellets were sintered at 1,060, 1,080, 1,100, and 1,120 degrees Celsius. Figure 19 displays the dielectric constant values for KNN and KNN-LS, which suggest that as x increases, the dielectric constant of KNN increases, however in the case of KNN-LS, it demonstrates that when Li and Sb concentrations in KNN decrease, both phase transitions and dielectric constant tend to decrease. a maximum piezoelectric coefficient value found 404 pm/V with KNN-LS by using y = 0.02.

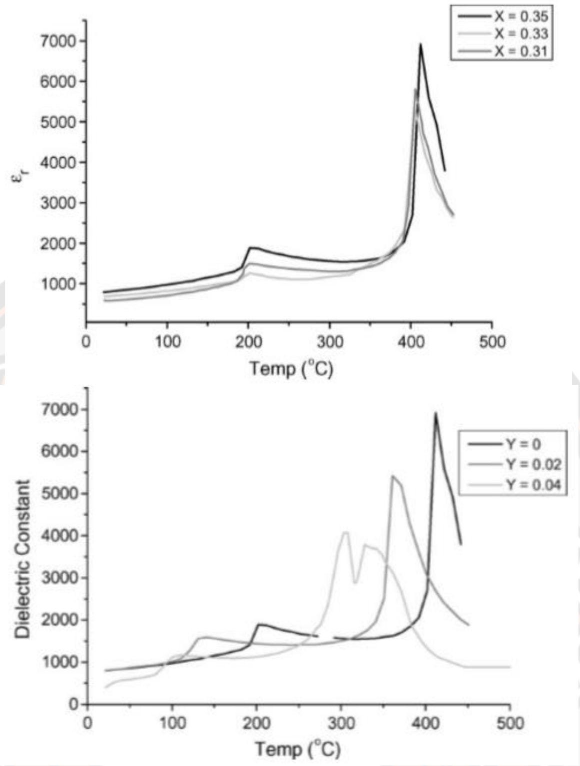

Figure 19 Temperature variations of KNN and KNN-LS dielectric constants at 100 kHz. [31]

In contrast, pure KNN solid solution has a low piezoelectric coefficient (80 pC/N) and weak residual polarization (~11 mC/cm^2), making it a poor candidate for electrostatic applications. Additionally, pure KNN ceramics are extremely difficult to create at high densities using conventional sintering procedures due to the volatility of K+ and Na+ and their limited phase stability at high sintering temperatures. Binary and ternary systems have been researched in order to increase the densification and electrical characteristics of KNN ceramics[32] by adding other piezoelectric elements such as $(K_{0.50}Na_{0.46}Li_{0.04})(Nb_{0.96-x}Ta_xSb_{0.04})O_3$ (x = 0, 0.12) or (KNN-LST) and $K_{0.52}N_{0.46}NbO_3$ or (KNN-N) was used to compare its result. A calcined powder was sintered at a temperature of 1,000 – 1,200 degrees Celsius for 4 hours after being calcined for 6 hours at 850 degrees Celsius. The bulk density and piezoelectric coefficient shows as the function of sintering temperature, which 1,130 °C shows maximum bulk density and piezoelectric coefficient of KNN-LST12 as 4.41 g/cm^3 and 192 pC/N, respectively (see Figure 20).

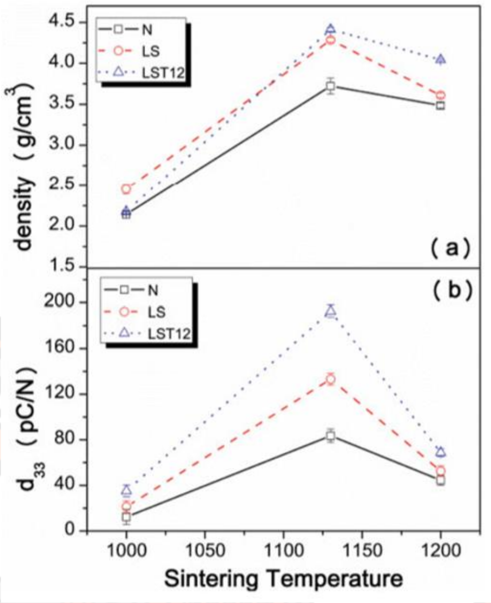

Figure 20 (a) Bulk densities, (b) d_{33} of KNN-N, KNN-LS and KNN-LST12 as a function of sintering temperature.[32]

Figure 21 depicts the dielectric characteristics of a material. KNN-LST12 ceramics display the highest dielectric constant of 1,019 at 1,130 C and the lowest dielectric loss of roughly 0.038 at 100 kHz.

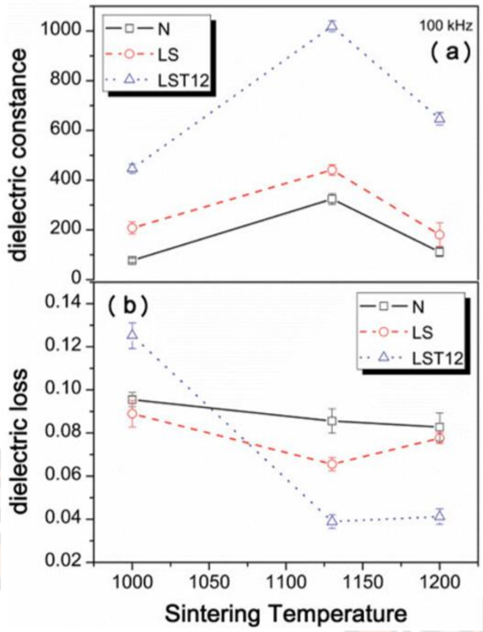

Figure 21 Dielectric constant and dielectric loss of KNN-N, KNN-LS, and KNN-LST12 at room temperature.[32]

2.6 Piezoelectric – cement composite

As mentioned previously, piezoelectric ceramics exhibit superior electrical sensitivity for monitoring the health of structures. Since 2002, cement-based piezoelectric composites have been developed to address volume compatibility and acoustic impedance incompatibilities between concrete structures and conventional piezoelectric sensors, which has an acoustic impedance of concrete is ≈ 10 x 10^6 kg/m^2s , but piezoelectric ceramics such as lead zirconate titanate (PZT) has a value of 34.6 x 10^6 kg/m^2s[41].

A. Chaipanich[58] studied piezoelectric – cement by using Portland cement type 1 and PZT ceramic. To manufacture PZT-OPC composites, the PZT ceramic particles (30-90 percent by volume) were mixed with Portland cement (PC) and allowed to cure for three days at 60 degrees Celsius and 100 percent relative humidity before being measured. After that, the effects of PZT on the dielectric and piezoelectric properties of the composites were explored further. The poling of PZT-OPC was carried out under a poling field of 2 kV/mm for 45 minutes in silicone oil at 130 °C, and the piezoelectric coefficient was measured after 24 hours of poling under the same conditions as above. shows that the dielectric constant and piezoelectric coefficient of composites both rise with the addition of PZT, with the maximum dielectric constant and piezoelectric coefficient of composites being 291 and 43 pC/N, respectively, when PZT was added to 90 percent of the composites.

Table 10 shows that the dielectric constant and piezoelectric coefficient of composites both rise with the addition of PZT, with the maximum dielectric constant and piezoelectric coefficient of composites being 291 and 43 pC/N, respectively, when PZT was added to 90 percent of the composites.

Table 10 Properties of PZT-PC composites.[58]

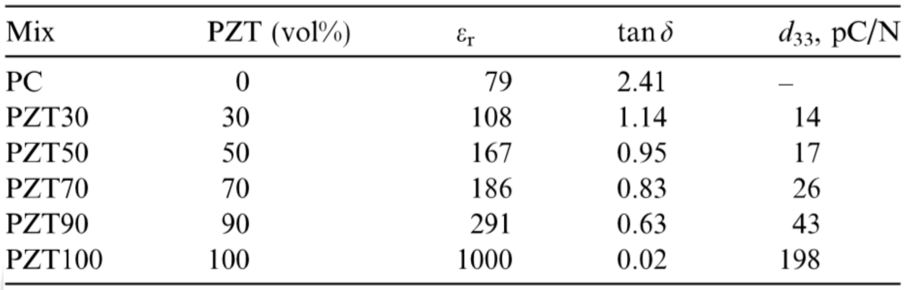

Mix	PZT (vol%)	ε_r	$\tan\delta$	d_{33}, pC/N
PC	0	79	2.41	–
PZT30	30	108	1.14	14
PZT50	50	167	0.95	17
PZT70	70	186	0.83	26
PZT90	90	291	0.63	43
PZT100	100	1000	0.02	198

Ruamporn Potong et al.[59] interested in 1-3 connectivity lead-free BNBK-Portland cement composite. Acoustic, dielectric, piezoelectric, electromechanical, and microstructural properties of composites were investigated in order to determine the optimal attributes of lead-free composites for smart structure applications. BNBK ceramic was added in increments of 30 %, 40 %, 50 %, 60 %, and 70 % by volume, with the dice-and-fill process being employed for each increment. According to the results, the acoustic impedance increased as the BNBK ceramic percentage was increased. The best BNBK content was found to be in the range of 30-50 % by volume due to an acoustic impedance match between composites and concrete (10 x 10^6 kg/m^{2}s), as shown in Figure 22.

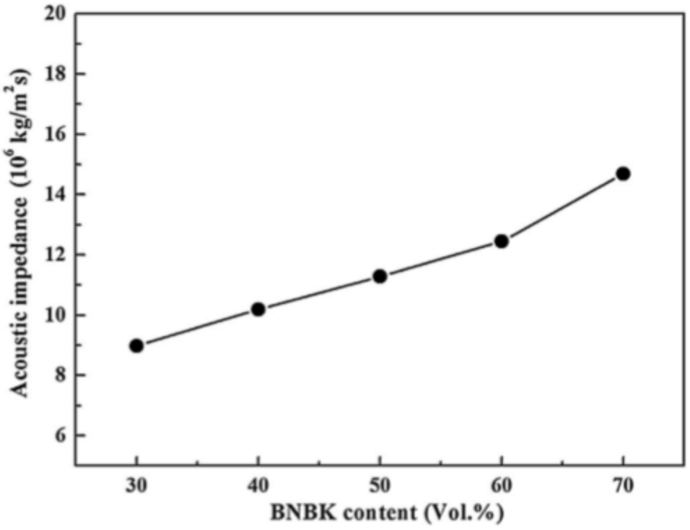

Figure 22 Effect of BNBK content on 1-3 BNBK-PC composites' acoustic impedance. [59]

The morphology of the 50% BNBK composite demonstrates a strong interfacial bond with the cement hydration product (calcium silicate hydrate, C-S-H). Figure 23 illustrates the dielectric constant and the resulting dielectric loss at room temperature (f = 1 kHz). The dielectric constant and dielectric loss are 447 and 0.09 with 70% BNBK concentration, respectively.

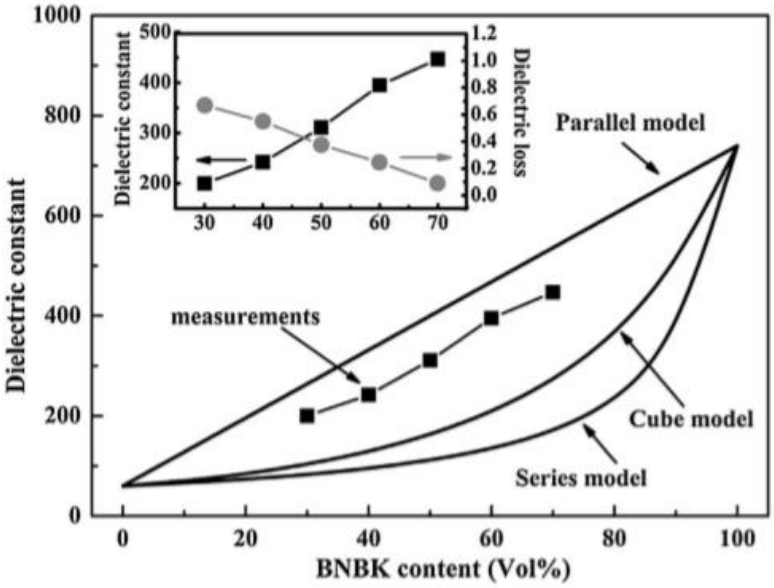

Figure 23 The dielectric characteristics of composites containing 1-3 BNBK and PC. [59]

Figure 24 illustrates the electromechanical coupling coefficient and the piezoelectric coefficient values. Both values tend to grow as the BNBK ceramic composition increases. The electromechanical coupling coefficient of 40%–70% BNBK ceramic was discovered to be near to 20%; it was previously reported that electromechanical coupling coefficient values close to 20% had a better potential as sensors.

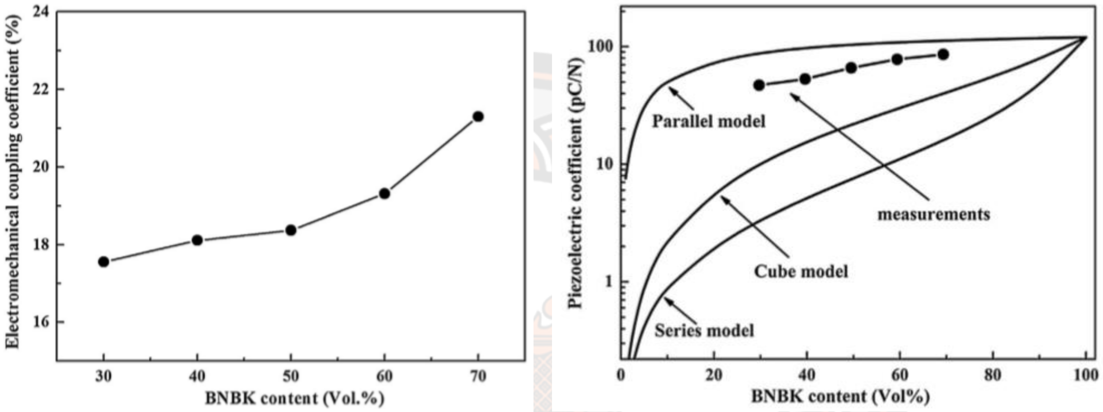

Figure 24 (a) Coefficient of electromechanical coupling and (b) The piezoelectric coefficient of composites containing 1-3 BNBK-PC.[59]

Rattiyakorn et al.[60] used 2-2 connectivity to investigate the dielectric and piezoelectric characteristics of BNT-Portland cement composites. By using the cut-filling approach, composites having a BNT content of 30%, 40%, 50%, 60%, and 70% by volume were manufactured. The BNT ceramic material was poled in a silicone oil bath along the thickness direction for 30 minutes at 80°C using a DC electric field of 3.5 kV/mm. At room temperature, the dielectric characteristics were determined using a 1 kHz signal. The dielectric constant increases linearly with increasing BNT content, as seen in Figure 25. On the other hand, the dielectric loss decreases as the BNT level increases. The piezoelectric coefficient also exhibits a strong dependence on the BNT ceramic composition, similar to the dielectric constant. When BNT is 70% by volume, the piezoelectric coefficient reaches 73 pC/N.

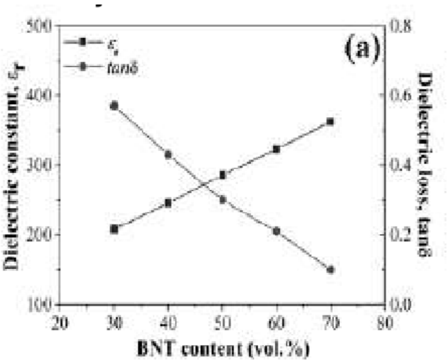

Figure 25 BNT-PC composites dielectric constant and dielectric loss.[60]

Phakin et al.[61] investigated the dielectric and piezoelectric properties of BZT-cement composites with high calcium fly ash additions (as a replacement for Portland cement). Fly ash was replacement into Portland cement of 0%, 10%, 30% and 50% by volume, which the compositions of the composites illustrated in Table 11. Poled samples of composites in silicone oil at 60 degrees Celsius for 45 minutes in fields of 0.5 kV/mm. The piezoelectric coefficient was then determined 24 hours after poling. At the interfacial zone, BZT ceramics can be bonded with cement containing calcium silicate hydrate (C-S-H). Additionally, fly ash is well known to react with calcium hydroxide from Portland cement's hydration product to generate calcium silicate hydrate, as illustrated in Figure 26.

Table 11 Compositions of the composites used for Fly ash was replacement into Portland cement.[61]

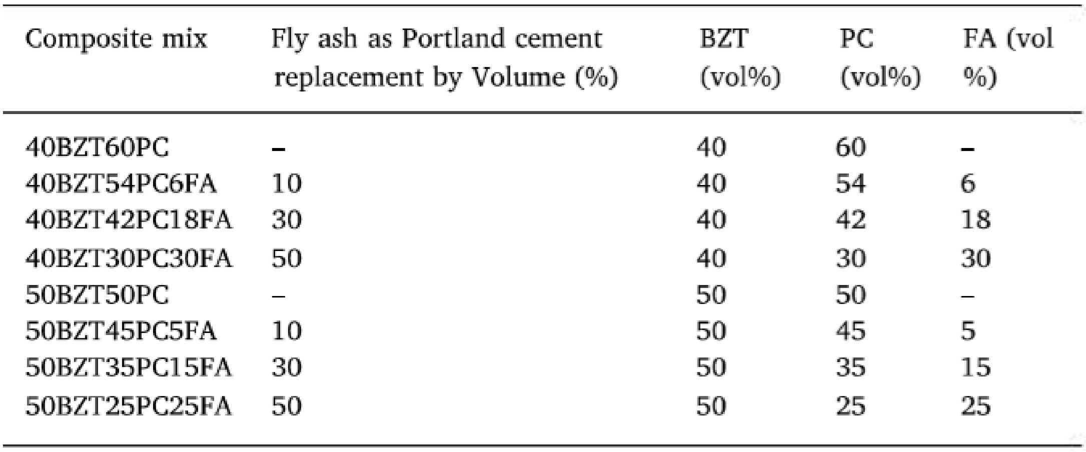

Composite mix	Fly ash as Portland cement replacement by Volume (%)	BZT (vol%)	PC (vol%)	FA (vol %)
40BZT60PC	–	40	60	–
40BZT54PC6FA	10	40	54	6
40BZT42PC18FA	30	40	42	18
40BZT30PC30FA	50	40	30	30
50BZT50PC	–	50	50	–
50BZT45PC5FA	10	50	45	5
50BZT35PC15FA	30	50	35	15
50BZT25PC25FA	50	50	25	25

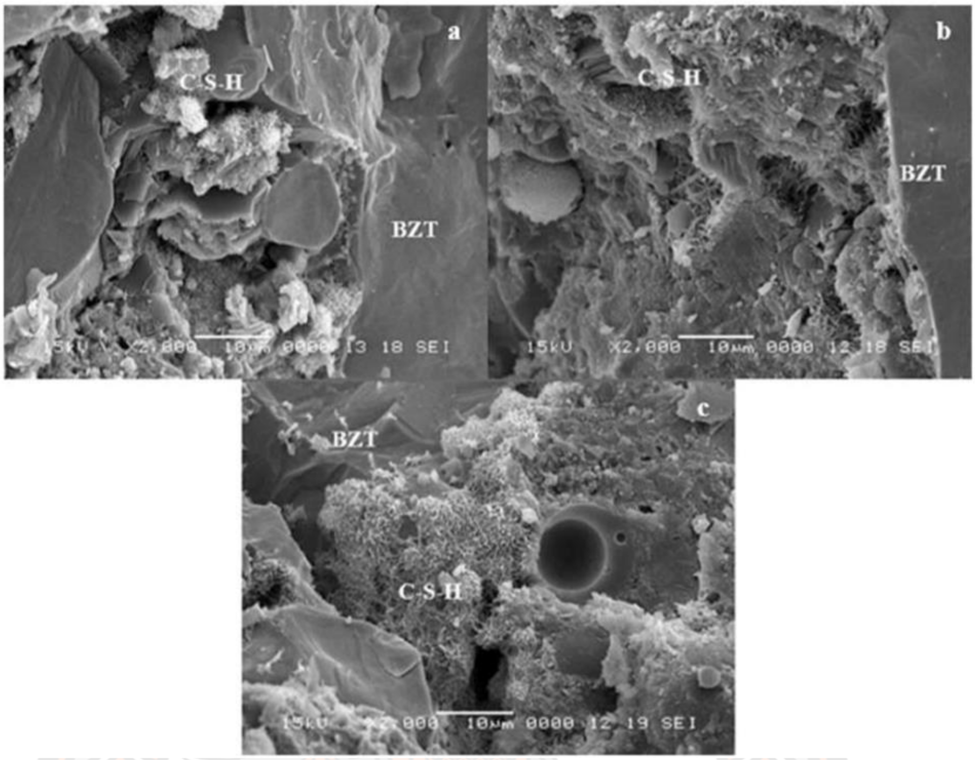

Figure 26 Composite BZT-PC SEM micrographs with (a) 10% volume of fly ash content, (b) 30% volume of fly ash content. And (c) 50% volume of fly ash content.[61]

The dielectric properties of 40% BZT and 50% BZT are shown in Figure 27. When fly ash concentration was increased, the dielectric constant and piezoelectric coefficient of composites dropped. On the other hand, it was discovered that the dielectric loss increased as the fly ash content rose.

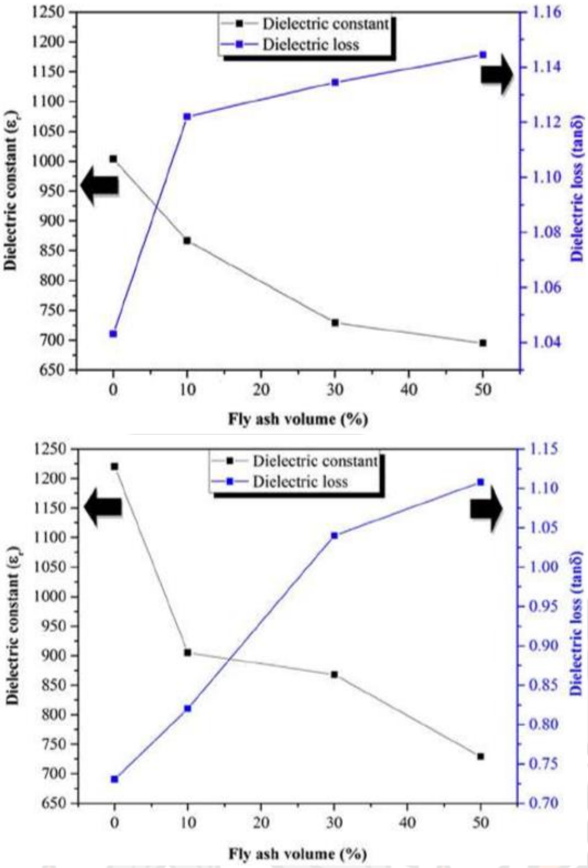

Figure 27 The effect of fly ash on dielectric properties of (a) 40BZT-PC/FA, (b) 50BZT-PC/FA composites at 1 kHz.[61]

The piezoelectric coefficient results are shown in Figure 28, where the piezoelectric coefficient values for 40BZT-PC/FA composite tend to decrease when increasing of fly ash and 50BZT-PC/FA shows similar results. However, when 10% fly ash was added to 50BZT-PC/FA, the piezoelectric coefficient increased to around 16.57 pC/N.

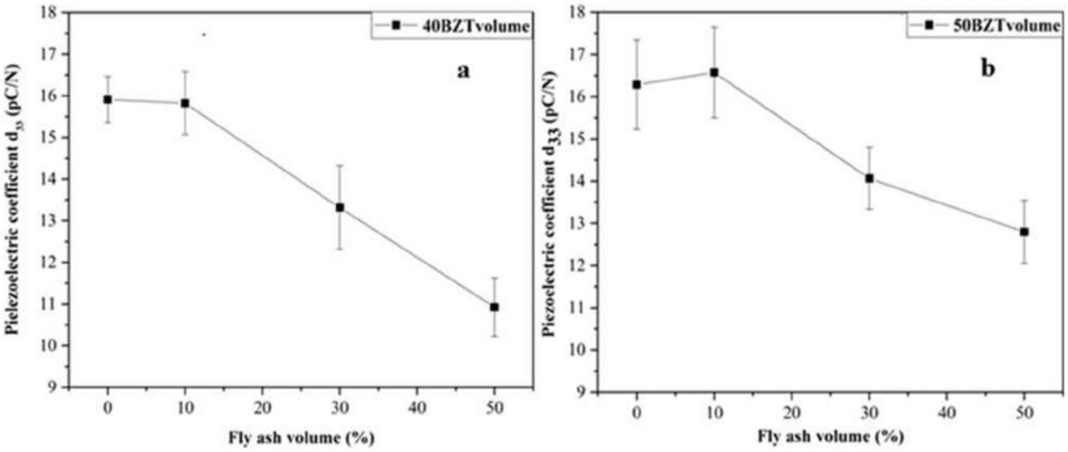

Figure 28 Fly ash's effect on the piezoelectric coefficient of (a) 40BZT-PC/FA and (b) 50BZT-PC/FA composites. [61]

Huang Hsing Pan et al.[62] investigated the influence of curing time and temperature on the piezoelectric characteristics of PZT-cement composites containing 50% PZT by volume. Without adding extra water, the powders of PZT ceramic and Portland cement were combined for 5 minutes in a solar-planetary mixer. The liquid was poured into a cylindrical steel mold with a 15 mm diameter. Following that, for 5 minutes, 80 MPa compression was applied to the mixture, resulting in the formation of a disc-like specimen. The samples were cured for one day (PP1), three days (PP3), and seven days (PP7) in a controlled environment set to 90 degrees Celsius and 100 percent relative humidity. All samples were subjected to a thermal treatment at A = 23 °C (room temperature) and B = 140 °C. The first time of temperature treatment occurred before to coating with silver paint at temperature A or B; the second time of temperature treatment occurred following the completion of the coating process at temperature A or B. At room temperature, the dielectric characteristics were determined using a 1 kHz signal. For piezoelectric characteristics, the sample was polarized in a 150°C silicone oil bath and then subjected to a 1.5 kV/mm poling field for 40 minutes. As illustrated in Figure 29, the influence of curing time on dielectric loss increased with increasing curing time for all heating conditions (pretreatment and posttreatment).

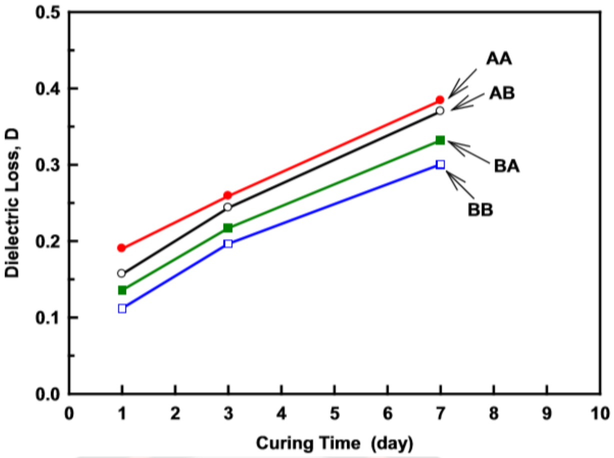

Figure 29 The dielectric loss of PP materials with time and temperature.[62]

The piezoelectric values of PP materials at various curing times and heating settings are shown in Figure 30. Due to the fact that PP1 has the lowest dielectric loss values, it exhibits a larger piezoelectric coefficient than other curing times, which likely enhances polarization efficiency. After polarization, the age of PP materials subjected to AB, BA, and BB heating conditions has an effect on their piezoelectric coefficient.

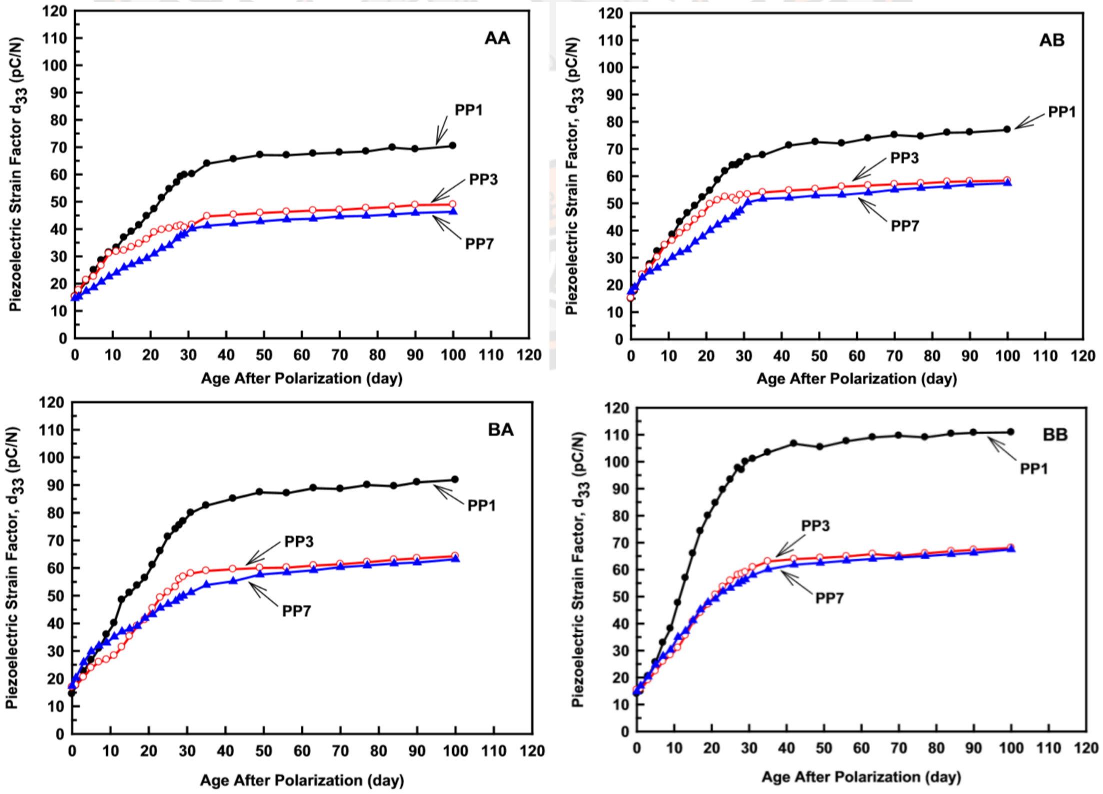

Figure 30 The effect of curing time on the piezoelectric coefficient of PP materials under the AA, AB, BA, and BB heating conditions.[62]

CHAPTER III
THE EXPERIMENTS

3.1 Synthesis of alite calcium sulfoaluminate cement

To synthesis ACSA clinker, high purity agents of $CaCO_3$, SiO_2, Al_2O_3, Fe_2O_3 and $CaSO_4 \cdot 2H_2O$ (purity higher than 98% for all) were used as starting materials with analytical grade of CaF_2 and CuO as additives. The particle size distribution curve and mean diameter (D [4,3]) of the raw materials and additives are shown in Figure 33. Target phases of the ACSA clinker were C_3S, C_2S, $C_4A_3\bar{S}$ and C_4AF for three target compositions, as shown in Table 12. Modified Bogue's equations [21] were applied to determine the raw material fractions of the three different clinker compositions, as shown in Eq. (3-1)- Eq.(3-5). The raw material composition of each mixture is listed in Table 13. To compare the effect of additives on the final phase compositions of the ACSA clinkers, each of the three compositions was prepared in two groups, one including CaF_2 (0.8 wt.%) + CuO (0.1 wt.%) additives in the raw materials and the second without additives in the raw materials for six experimental powder mixtures. The clinkers developed without additives were named as R-group mixes indicating the reference group, while those with additives were designated M-group implying "modified".

Table 12 Target compositions of the mixture designs.

Phase composition	Target compositions of designed mixture (wt.%)		
	Mix A	Mix B	Mix C
C_3S	55	45	35
C_2S	30	30	30
$C_4A_3\bar{S}$	5	15	25
C_4AF	10	10	10
$C\bar{S}$	0	0	0

$C_3S = 4.07(CaO – f_{CaO}) – 7.60SiO_2 – 2.24Al_2O_3 – 4.29Fe_2O_3 - 2.85SO_3$ Eq. (3-1)

$C_2S = 8.60SiO_2 + 1.69Al_2O_3 + 3.24Fe_2O_3 + 2.15SO_3 - 3.07(CaO-f_{CaO})$ Eq. (3-2)

$C_4A_3\bar{S} = 2.00Al_2O_3 – 1.27Fe_2O_3$ Eq. (3-3)

$C_4AF = 3.04Fe_2O_3$ Eq. (3-4)

$C\bar{S} = 1.70SO_3 – 0.45Al_2O_3 + 0.28Fe_2O_3$ Eq. (3-5)

Table 13 Targeted mineralogical phase assemblage and raw materials.

Chemical composition	Required wt.% of oxide		
	Mix A	Mix B	Mix C
CaO (C)	66.52	62.83	59.14
SiO_2 (S)	24.93	22.30	19.66
Al_2O_3 (A)	4.59	9.59	14.59
Fe_2O_3 (F)	3.29	3.29	3.29
SO_3 ($\bar{S}$)	0.67	2.00	3.32
Raw materials	Required wt.% of raw materials		
	Mix A	Mix B	Mix C
$CaCO_3$	77.50	73.54	69.42
SiO_2	16.38	14.95	13.46
Al_2O_3	3.02	6.43	9.98
Fe_2O_3	2.16	2.21	2.25
$CaSO_4·2H_2O$	0.95	2.88	4.89

The raw materials were mixed by the ball milling method for 3 hours in an ethanol medium to obtain high mixed powder homogeneity and to avoid reaction between the raw materials and water. After the mixing process, the materials were heated on a hot plate with a magnetic stirrer until dry and then ground and sieved through a No. 200 sieve to obtain a fine powder. The samples were then moulded into spherical shapes of about 1 cm diameter to promote good contact between the solid phases in the sintering process [21]. All samples were initially fired at 900 °C with a heating rate of 5 °C/minute and then soaked for 30 minutes to decompose $CaCO_3$ to CaO and CO_2 [1, 3]. After the decomposition period, the firing temperature was increased to one of six different maximum temperatures (1,100 °C; 1,200 °C; 1,250 °C; 1,275 °C; 1,300 °C; or 1,325 °C) for 30 minutes with a similar heating rate of 5 °C/minute. The hydraulic phases can be stabilised at low temperature by the quenching process [1]. Therefore, the hot clinkers were removed from the furnace immediately and cooled rapidly by a fan to maintain their phase composition at high temperature and prevent the formation of undesired phase at low temperature [52, 63]. Fineness of the clinker highly influenced the mechanical properties of ground cement [64, 65]. The clinkers were ground by a swing mill lab sample grinder for 1 minute and then sieved through a No. 200 sieve to control the particle size.

3.2 Modified potassium sodium niobate ceramic fabrication

To synthesise the $(K_{0.44}Na_{0.52}Li_{0.04})(Nb_{0.84}Ta_{0.10}Sb_{0.06})O_3$ powder, the KNLNTS powder starting material contained high purity agents of $KHCO_3$ (99%), Na_2CO_3 (99%), Li_2CO_3 (99%), Nb_2O_5 (99%), Ta_2O_5 (99%), and Sb_2O_5 (99%). These materials were mixed in ethanol by milling with zirconia balls for 24 hours. Then the mixture was heated on a hot plate with a magnetic stirrer to remove the ethanol. Next, the powder was divided into four portions and each portion was calcined at either 650°C, 750°C, 850°C, or 900°C (four experimental temperatures) for 6 hours at a heating rate of 5°C/minute. The four calcined samples were analysed using X-ray powder diffraction (XRD) to identify the optimal version that delivers the purest KNLNTS. The selected calcined sample was mixed with oxides of CuO (0.2 wt.%), Fe_2O_3 (0.4 wt.%), and Bi_2O_3 (0.3 wt.%) to reduce the sintering temperature of the final KNLNTS ceramics and improve their physical qualities [36]. This new mixture was ball milled for 24 hours and then dried in the same manner that the previous mixture was. At an 80 MPa pressure, the dried mixture was pressed mechanically into disk-shaped pellets with a diameter of 15 mm. After that, the pellets were sintered at either 1000°C, 1025°C, 1050°C, 1075°C, or 1100°C for 2 hours at a heating rate of 5°C/minute. XRD and SEM were conducted to analyse the sintered pellets and select the optimal version. The optimal sample was tested for acoustic impedance, dielectric properties, and piezoelectric properties.

Table 14 Specifications of the base materials for the KNLNTS + 0.2wt%CuO +0.4wt%Fe_2O_3 +0.3wt%Bi_2O_3 ceramic

	Oxide
Base materials	$KHCO_3$
	Na_2CO_3
	Li_2CO_3
	Nb_2O_5
	Ta_2O_5
	Sb_2O_3
Sinter aids	CuO
	Fe_2O_3
	Bi_2O_3

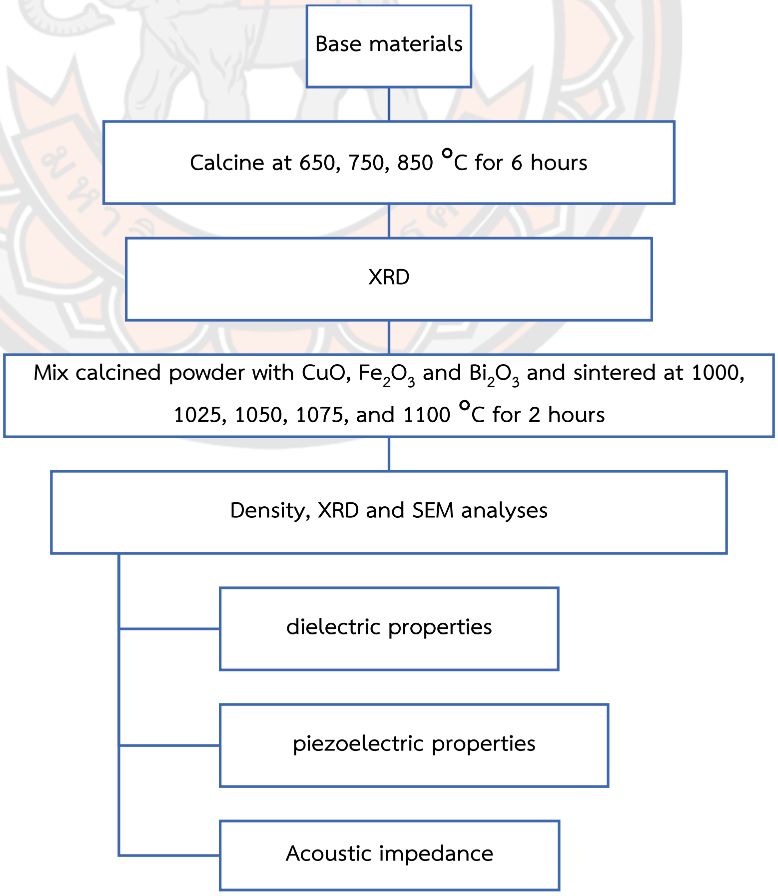

Figure 31 Steps for investigating the KNLNTS + sinter aids

3.3 Fabrication of the piezoelectric-cement composites

KNLNTS ceramic pellets previously manufactured were ground and sieved to a particle size range of 300 – 600 μm [66]. This ground powder was mixed with the previously prepared ACSA cement to prepare five different experimental KNLNTS/ACSA cement composites (0-3 connectivity) with respective KNLNTS volumes of 30%, 40%, 50%, 60%, and 70%. A hydraulic press at a pressure of 80 MPa was used to press each of the five composites into 1.5 mm thick disk-shaped pellets with a diameter of 15 mm. Next, the composite pellets were placed in a curing chamber for 1 day under controlled conditions of 60°C and 98% relative humidity [61] to allow the cement to hydrate and thereby bind the composite. The pellets were heated at 60°C in an oven for 3 days to enhance the composite's electrical characteristics and then sample pellets of each composite were tested for density and acoustic impedance. Before poling, the samples were polished to obtain smooth parallel top and bottom surfaces. The top and bottom of each pellet were then covered with silver paint. During polarisation of the composites, each sample was placed at room temperature in a silicone oil bath and subjected to a 1.5 kV/mm poling field for 40 minutes to determine its piezoelectric characteristics.

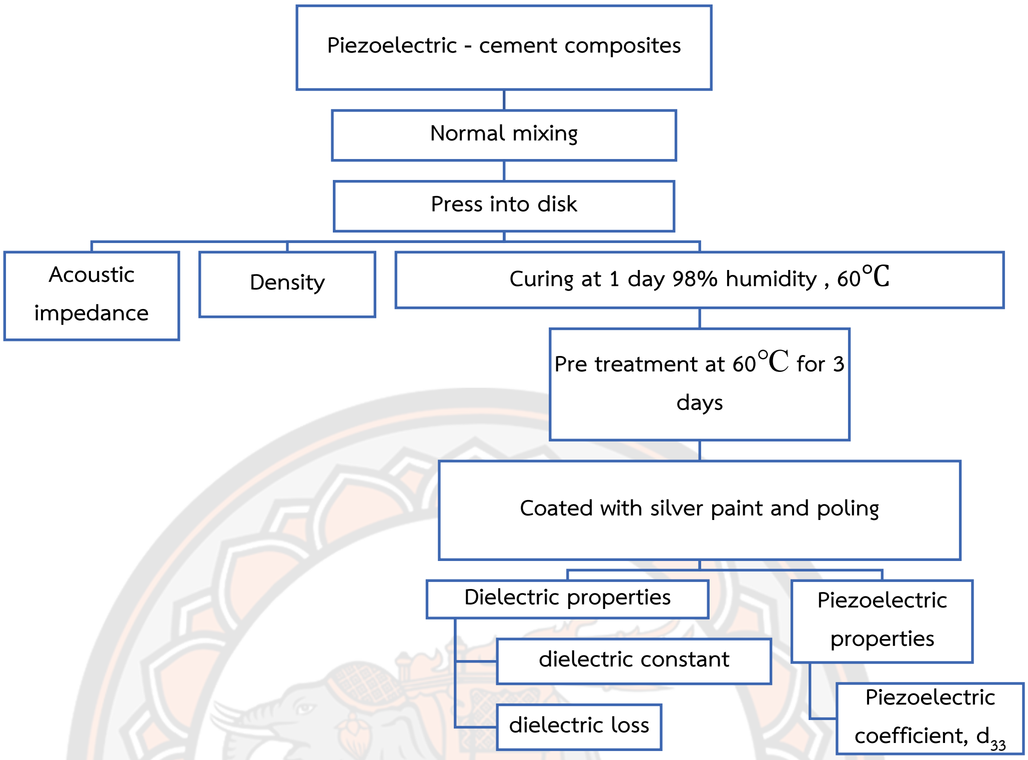

Figure 32 Piezoelectric-cement based composites fabrication.

3.4 Characterization measurements

Density and porosity

The density of piezoelectric ceramic-cement based composite was obtained using the Archimedes method which was described using the following Eq.(3-6):

$$\rho(\text{density}) = \frac{W_1\rho_w}{W_2-W_3} \qquad \text{Eq. (3-6)}$$

Where W_1 is the dry composites weight in air, then weighted again after fluid impregnation (W_2), and finally weight being immersed in water (W_3). ρ_w is the density of water at room temperature.

Acoustic impedance

The acoustic impedance of material has been measured for fundamental understanding of the acoustic property. Under the influence of sound pressure, sound passes through materials. Because the molecules or atoms of a solid are elastically connected, an increase in pressure leads in the propagation of a wave through the solid. The following applet can be used to determine the acoustic impedance of any material, if the density (ρ) and acoustic velocity (V) of the material are known. The acoustic velocity of composites (Vc) was determined in this study utilizing an ultrasonic thickness meter. The acoustic impedance (Zc) values measured experimentally were determined by multiplying the densities of composites (ρ_c) by the velocities (Eq.(3-7)). The following formulae can be used to determine the composite's acoustic impedance (Zc):

$$Z_c = \rho_c \, x \, V_c \qquad \text{Eq.(3-7)}$$

Particle size distribution

Particle size distribution of the raw materials and additives was investigated in an ethanol medium using a laser diffraction particle size analyser. Measurements were repeated at least three times to ensure repetition. Various particle sizes such as volume and mean diameter value (D [4, 3]) were also computed.

X-ray Diffraction (XRD)

X-ray powder diffraction is most widely used for the identification and characterisation of crystalline materials and measurement of sample purity. Therefore, the X-ray diffraction (XRD) analytical technique was used for phase identification of the ACSA clinkers. This analysis was performed with a Bruker-D8 ENDEAVOR Diffractometer (CuK_α λ = 0.15406 nm) operating at 45 kV and 30 mA. The measurements were calculated within the 2θ range of 8° to 65°.

The Rietveld refinement technique

The Rietveld method, born from the simple and brilliant idea of refining crystal structure together with parameters describing the diffraction profile directly employing the profile intensities, has been one of the most innovative and still now widely applied methods for studying materials from powder diffraction data. It has given a great impulse to the process of crystal structure solution by powder diffraction data, expanding the fields of application of powder diffraction which, up to the end of the 1970's, was primarily used for qualitative and semiquantitative analysis. Powder diffraction without the Rietveld method would be much less popular.

The Rietveld refinement technique was used to calculate the amount of quantitative phase. This was performed using DIFFRAC.SUITE TOPAS V.5.0 software, calculated by the XRD patterns from the model structure. The observed diffraction pattern was refined by fitting the calculated diffraction pattern to determine the crystal structures and the modal amounts of minerals (quantitative analysis). To confirm the reliability of the phase quantitative analysis, the goodness of fit (*GOF*) and the weighted profile residual (R_{wp}) values of the profile refinement were used to evaluate the quality of the fits in the Rietveld refinement processes. The *GOF* and R_{wp} values were calculated by Eq.(3-8)-Eq.(3-9). Generally, the results can be considered as reliable if the *GOF* and the R_{wp} values are lower than 4 and 12 respectively.

$$GOF = \sum_{i}^{n} \frac{[y_i(obs) - y_i(calc)]^2}{N-P} \qquad \text{Eq.(3-8)}$$

$$R_{wp} = \sum_{i}^{n} \sqrt{\frac{w_i[y_i(obs) - y_i(calc)]^2}{w_i[y_i(obs)]^2}} \qquad \text{Eq.(3-9)}$$

Where $y_i(obs)$ is the observed diffraction pattern, $y_i(calc)$ is the calculated diffraction pattern, N is the number of observations, P is the number of parameters and w_i is a suitable weight associated with each observed diffraction pattern.

X-ray fluorescence (XRF)

The chemical composition of samples was determined using X-ray fluorescence (XRF) analysis in terms of main oxides and trace elements. All XRF analyses were performed in accordance with ASTM D 4327-97.

Scanning electron microscopy (SEM)

Microstructural analysis is frequently employed in modern material science research as a potent technique for predicting a wide variety of material properties. Micrographs are created by scanning the surface of an object with a small electron probe (an electron beam) in sync with an electron beam from a source. Scanning electron microscopy (SEM) is a widely used technology in materials and biological sciences, as well as in industry, for high magnification microstructural examination.

Electrical measurements

- Dielectric measurement

The dielectric properties of the specimen were examined by LCR meter at room temperature. The LCR-meter measured the capacitance (C) and loss tangent (tan δ) of the samples. Relatives dielectric constant can be calculated using the following formula in Eq.(3-10):

$$\varepsilon_r = \frac{Cd}{\varepsilon_0 A} \qquad \text{Eq.(3-10)}$$

Where ε_r is the dielectric constant of the material between the plate, C is the capacitance of the sample, d is the thickness, ε_0 is the permittivity of free space equal to 8.85 x 10^{-12} $C^2/(J \cdot m)$ and A is the electrode area.

- Piezoelectric measurement

Poling is the process of aligning all of these distinct dipole moments in the same general direction. For polar axes, orientation is accomplished via the poling technique, which entails supplying a direct current to the material for an extended period of time. The amplitude and duration of the voltage required for poling very substantially between materials. Some material will pole easily and if used in large-signal switching applications may not even require a preliminary poling cycle. Other can only be poled near their curie point where the coercive field of the material is small. The greatest poling voltage that can be applied is constrained by the material's breakdown and arcing. As a result, poling is frequently performed in a silicon oil bath.

The strain constants or "d" coefficients are the piezoelectric coefficients or piezoelectric constants that relate the mechanical strain produced by an applied electric field to the piezoelectric coefficient or piezoelectric constants. The piezoelectric d constant expresses the charge density or strain per unit stress or field. When the force is applied in the three directions (along the polarization axis), the d_{33} is impressed on the same surface as the charge is collected.

CHAPTER IV THE RESULTS PART I: Effects of CaF_2-CuO additives and various firing temperatures on characteristics of alite calcium sulfoaluminate clinkers

4.1 Particle size analysis results

Figure 33 shows the particle size distribution curve and mean diameter of the raw materials and additives used. The narrowest particle size distribution and largest size were seen in Al_2O_3. while Fe_2O_3 and CaF_2 exhibited gap grade particle size distribution. All the other raw materials and additives showed favourable particle size distribution with similar mean diameter.

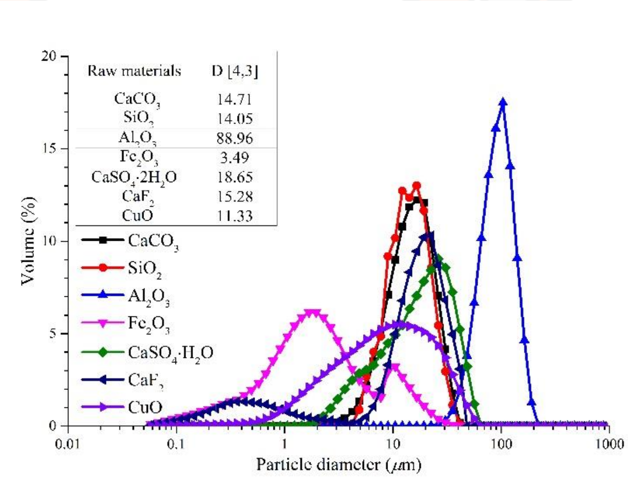

Figure 33 Particle size distibution of raw materials, D [4,3] = volume mean diameter (μm)

4.2 X-ray fluorescence analysis results

Chemical compositions of the clinkers analysed using the XRF technique are shown in Table 15. The clinker fired at 1,250 °C was chosen as the representative sample to be analysed for its chemical composition. Results suggested that the chemical composition of the fired samples showed slight differences when compared to the designed compositions.

Table 15 Chemical composition of clinkers fired at 1,250 °C.

Mixture	Condition	Chemical composition (%)				
		CaO	SiO_2	Al_2O_3	Fe_2O_3	SO_3
Mix A	Designed	66.52	24.93	4.59	3.29	0.67
	R-group	66.30	23.02	4.53	1.90	0.97
	M-group	68.31	23.66	4.61	1.94	0.97
Mix B	Designed	62.83	22.30	9.59	3.29	2.00
	R-group	64.58	20.95	9.75	2.03	2.24
	M-group	65.00	21.03	9.56	2.01	2.21
Mix C	Designed	59.14	19.66	14.59	3.29	3.32
	R-group	60.67	18.14	14.78	2.08	3.46
	M-group	60.00	18.25	14.59	2.07	3.46

4.3 X-ray diffraction patterns analysis results

Figure 34 shows the XRD patterns of the ACSA clinker of Mix A fired at various firing temperatures ranging from 1,100 °C to 1,325 °C. For the R-group clinkers, the XRD patterns revealed C_2S, $C_4A_3\bar{S}$, C_3A, C_4AF, and free lime components. Moreover, increasing the firing temperature slightly affected a change in their phase formation. For the M-group samples fired at 1,100 °C, the C_3S, C_2S, $C_4A_3\bar{S}$, C_3A, C_4AF and free lime were detected. The peak intensities of C_3S tended to increase when the firing temperature increased, accompanied by a decrease of both C_2S and free lime peak intensities. This was due to C_3S formation occurring as a result of the combination of C_2S and free lime [21]. The intensity peaks of $C_4A_3\bar{S}$ also slightly decreased when the firing temperature was higher than 1,250 °C.

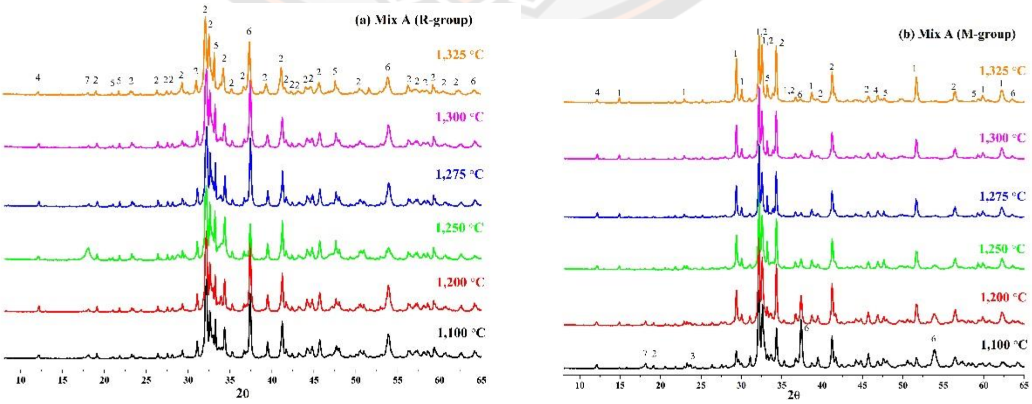

Figure 34 XRD patterns of Mix A-clinker; (a) R-group and (b) M-group
1 = C_3S, 2 = C_2S, 3 = $C_4A_3\bar{S}$, 4 = C_4AF, 5 = C_3A, 6 = free lime, 7 = $C_{12}A_7$

Comparisons of the XRD patterns of both the R-group and M-group for Mix B clinkers are illustrated in Figure 35. For the R-group samples, the diffraction patterns suggested C_2S as a main phase composition for all firing temperatures. As the firing temperature increased, the peak intensities of $C_4A_3\bar{S}$ and free lime tended to decrease, while C_3A showed strong peak intensity, especially when the firing temperature was higher than 1,250 °C. Adding CaF_2 and CuO caused C_3S initially to form at low temperature. This was more clearly observed when the firing temperature was increased (Figure 35 (b)). With increasing firing temperatures, the peak intensities of C_3A also tended to increase, while $C_4A_3\bar{S}$ and free lime peak intensities decreased. These observations suggested that $C_4A_3\bar{S}$ may initially decompose at firing temperatures higher than 1,250 °C [20].

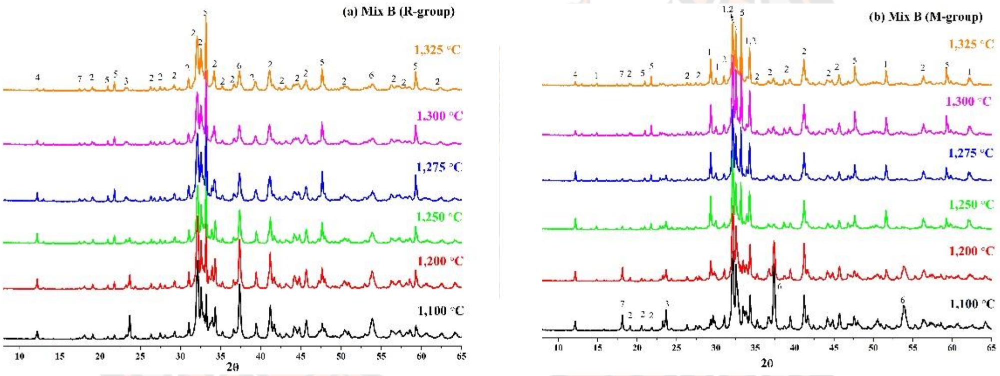

Figure 35 XRD patterns of Mix B-clinker; (a) R-group and (b) M-group
1 = C_3S, 2 = C_2S, 3 = $C_4A_3\bar{S}$, 4 = C_4AF, 5 = C_3A, 6 = free lime, 7 = $C_{12}A_7$

In the case of Mix C, diffraction patterns of the R-group samples fired at 1,100 °C were indexed as C_2S, $C_4A_3\bar{S}$, C_3A, C_4AF and free lime (Figure 36(a)). When the firing temperature increased to 1,250 °C – 1,325 °C, the peak intensities of $C_4A_3\bar{S}$ decreased, while C_3A showed stronger peak intensities. The XRD patterns of the M-group samples showed that C_2S, $C_4A_3\bar{S}$, C_3A, C_4AF, $C_{12}A_7$ (mayenite) and free lime were formed at 1,100 °C (Figure 36(b)). When firing at temperatures higher than 1,250 °C, the peak intensities of $C_4A_3\bar{S}$ and free lime decreased and the formation of C_3S was clearly observed. At firing temperatures between 1,275 and 1,325 °C, C_3A showed strong peak intensities.

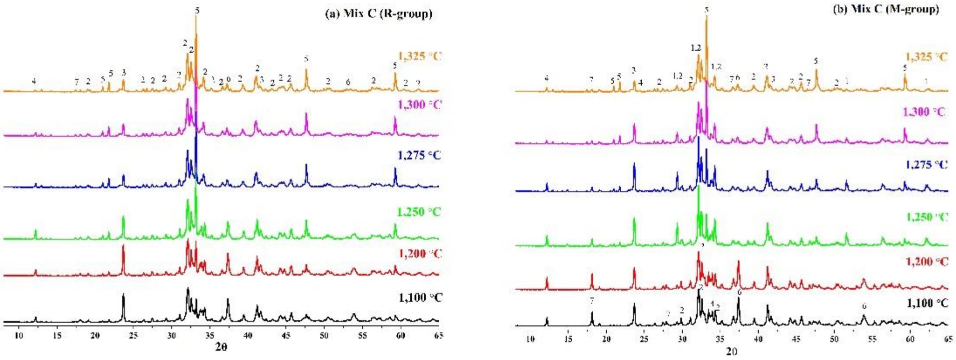

Figure 36 XRD patterns of Mix C-clinker; (a) R-group and (b) M-group
1 = C_3S, 2 = C_2S, 3 = $C_4A_3\bar{S}$, 4 = C_4AF, 5 = C_3A, 6 = free lime, 7 = $C_{12}A_7$

4.4 Phase quantitative analysis

For the in-depth quantitative analysis of the clinker phases, the Rietveld refinement technique was used to analyse the phase content through the XRD patterns. The Rietveld refinement process was performed until the reliability indices were acceptable (R_{wp} lower than 12). The results are listed in Table 16-Table 18.

Figure 37 shows the variation of phases content resulting from the firing temperatures of Mix A. For the R-group clinkers, it was obvious that C_3S initially formed at 1,250 °C. By increasing the firing temperature, C_3S slightly increased and reached maximum of 8.21 wt.% at 1,325 °C. However, this content was remote from the designed content of 55 wt.%. The main phase of the R-group sample is C_2S, which started to form at 1,100 °C to be 66 wt.% and then slightly increased when the firing temperature increased to 1,325 °C. However, the content of C_2S was significantly higher than that of the designed content of ~ 30 wt.%. The $C_4A_3\bar{S}$ initially formed at 1,100 °C and subsequently slightly changed in the range of 0.49-0.84 wt.% when the firing temperature increased. However, the $C_4A_3\bar{S}$ content was significantly lower than the designed content, while the unassigned phases of C_3A and $C_{12}A_7$ might occur instead of $C_4A_3\bar{S}$. The C_4AF content increased with the increase of the firing temperature and reached a maximum at 1,200 °C, at which the C_4AF content tended to decrease. A rich amount of free lime and C_2S content suggested that C_3S cannot fully form at lower temperatures without additives. For the Mix A clinkers (M-group), C_3S initially formed at 1,100 °C for 16.14 wt.%, which was higher than the R-group sample for all firing temperatures. The C_3S content tended to increase with increases in the firing temperature. The closed C_3S content compared to the designed content was observed from the sample fired at 1,250 °C. C_2S and free lime content started at 57.18 and 15.31 wt.%, respectively. The increase of the firing temperature effected the C_2S and free lime phases, both of which decreased. The $C_4A_3\bar{S}$ phase content showed similar characteristics to the Mix A clinkers (R-group) composition. C_4AF phase initially formed at 1,100 °C and the phase content was insignificantly changed with increasing firing temperatures. The decrease of C_2S and free lime corresponded with an increase of C_3S content in the M-group which suggests that the CaF_2 – CuO additives promoted the formation of C_3S by accelerating the reaction of C_2S and free lime.

Figure 38 shows the phase quantitative analysis of the Mix B clinkers analyzed by the Rietveld refinement method. For the R-group samples, the C_3S content showed in very small amounts lower than 1.0 wt.%, and their content was not significantly affected by varying the firing temperature. C_2S was a main phase composition around 61.22 wt.% for the samples fired at 1,100 °C, and then slightly increased with increased firing temperatures. However, the C_2S content was significantly higher than that of the designed content for all the firing temperatures. The $C_4A_3\bar{S}$ content initially formed at 1,100 °C for 6.55 wt.% and tended to decrease with increasing firing temperatures. The received amount of $C_4A_3\bar{S}$ was also lower than that of the target composition ~15 wt.%. The content of C_4AF was very close to the target content at 1,100 °C. Increasing the firing temperature caused the C_4AF phase to decrease. The unassigned phases of C_3A and free lime that were found in the sample when fired at 1,100 °C, increased with increasing firing temperatures. For the M-group samples, the C_3S initially formed at 1,100 °C with 4.75 wt.%. Enhancing the firing temperature caused an increase in the C_3S content which reached maximum with close to the designed content at the firing temperature of 1,250 °C. Thereafter, increases in the firing temperature caused C_3S content to decrease. In the case of C_2S, 59.65 wt.% was found at the firing temperature of 1,100 °C, with the C_2S content decreased at close to the target content of 30 wt.% at 1,250 °C. It increased again when the firing temperature increased. $C_4A_3\bar{S}$ phase formed at 4.82 wt.% at 1,100 °C and it decreased with increased firing temperatures, similarly to the R-group samples. However, the content of $C_4A_3\overline{S}$ was also significantly lower than that of the target phase content of 15 wt.%. The unassigned phases of C_3A and $C_{12}A_7$ were observed. The C_3A content was remarkably increased while $C_{12}A_7$ was decreased when the firing temperature exceeded 1,250 °C. The variation of C_4AF content with a varying firing temperature showed a similar trend to the R-group samples. Free lime content showed a maximum value of 14.96 wt.% at 1,100 °C, and then significantly decreased when the firing temperature exceeded 1,250 °C.

The variation of phases content with firing temperatures of Mix C is illustrated in Figure 39. For the R-group clinkers, the C_3S content was detected in small amounts for all firing temperatures, a finding remote from the target content of 35 wt.%. The C_2S was the main composition of Mix C (R-group), with a content of 55.33 wt.%; observed in the sample fired at 1,100 °C. Increases of the firing temperature also increased the C_2S content. The $C_4A_3\overline{S}$ phase started to form at 14.94 wt.% at 1,100 °C, then decreased when the firing temperature increased. This amount is lower than the target content of 25 wt.%. The unassigned phase of C_3A was found at 1,100 °C at 8.81 wt.% and then increased with increasing firing temperatures and reached a maximum content of 26.08 wt.% at 1,325 °C. The C_4AF content was closely aligned with the target phase of 10 wt.% for samples fired at 1,100 °C – 1,200 °C. Free lime content was 8.91 wt.% at 1,100 °C and tended to decrease with increased firing temperatures and was eliminated when the firing temperature was higher than 1,275 °C. For M-group clinkers, the C_3S content initially formed at around 0.4 wt.% at the firing temperature of 1,100 °C and then increased suddenly to 33.88 wt.% at 1,250 °C. Subsequent increases in the firing temperature caused the C_3S content to decrease. The C_2S content formed at 56.82 wt.% at 1,100 °C and then decreased with increments of the firing temperature. When the firing temperature was higher than 1,250 °C, the C_2S content tended to increase. $C_4A_3\overline{S}$ phase initially formed at 1,100 °C and then decreased when the firing temperature increased. $C_{12}A_7$ content also found at 1,100 °C at 9.28 wt.% and it then slightly decreased the firing temperature increased. C_3A content showed increased content when the temperature exceeded

1,250 °C and then reached a maximum of 26.95 wt.% at 1,325 °C. The C_4AF content showed similar changes to the R-group samples. Free lime content was 10.05 wt.% at 1,100 °C which then decreased substantially when the firing temperature was higher than 1,250 °C.

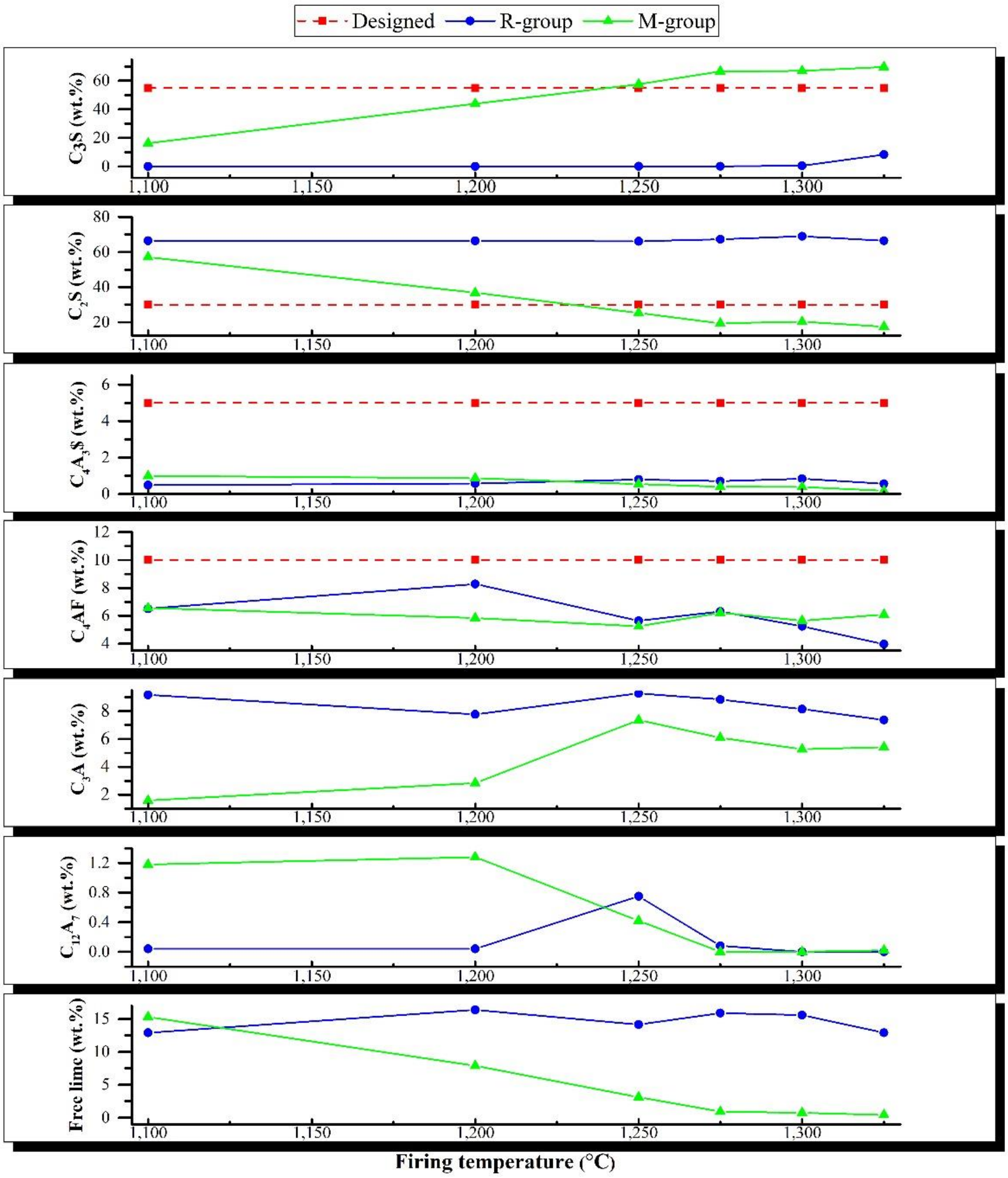

Figure 37 Variation of phases contents with firing temperatures of Mix A

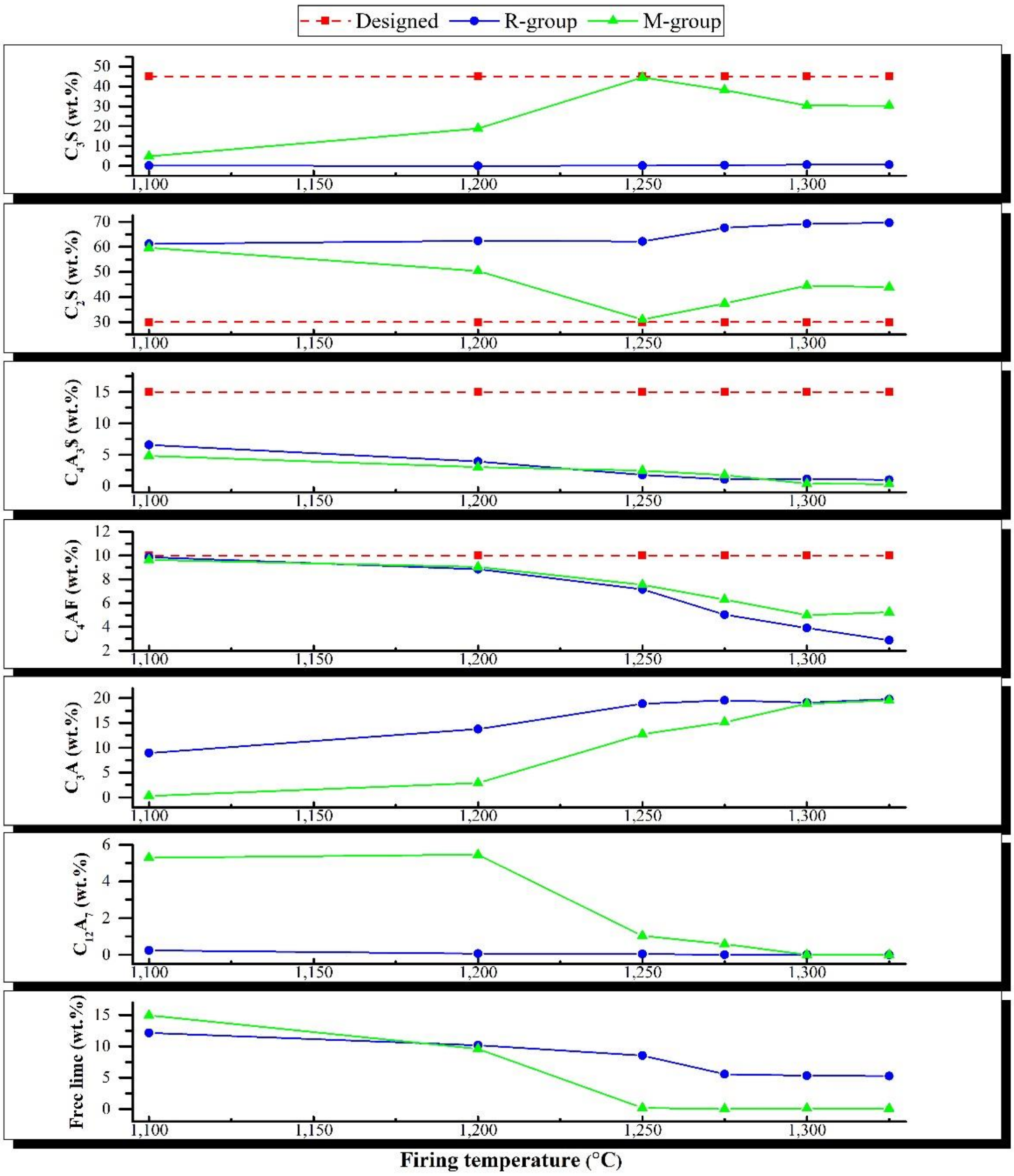

Figure 38 Variation of phases content with firing temperatures of Mix B

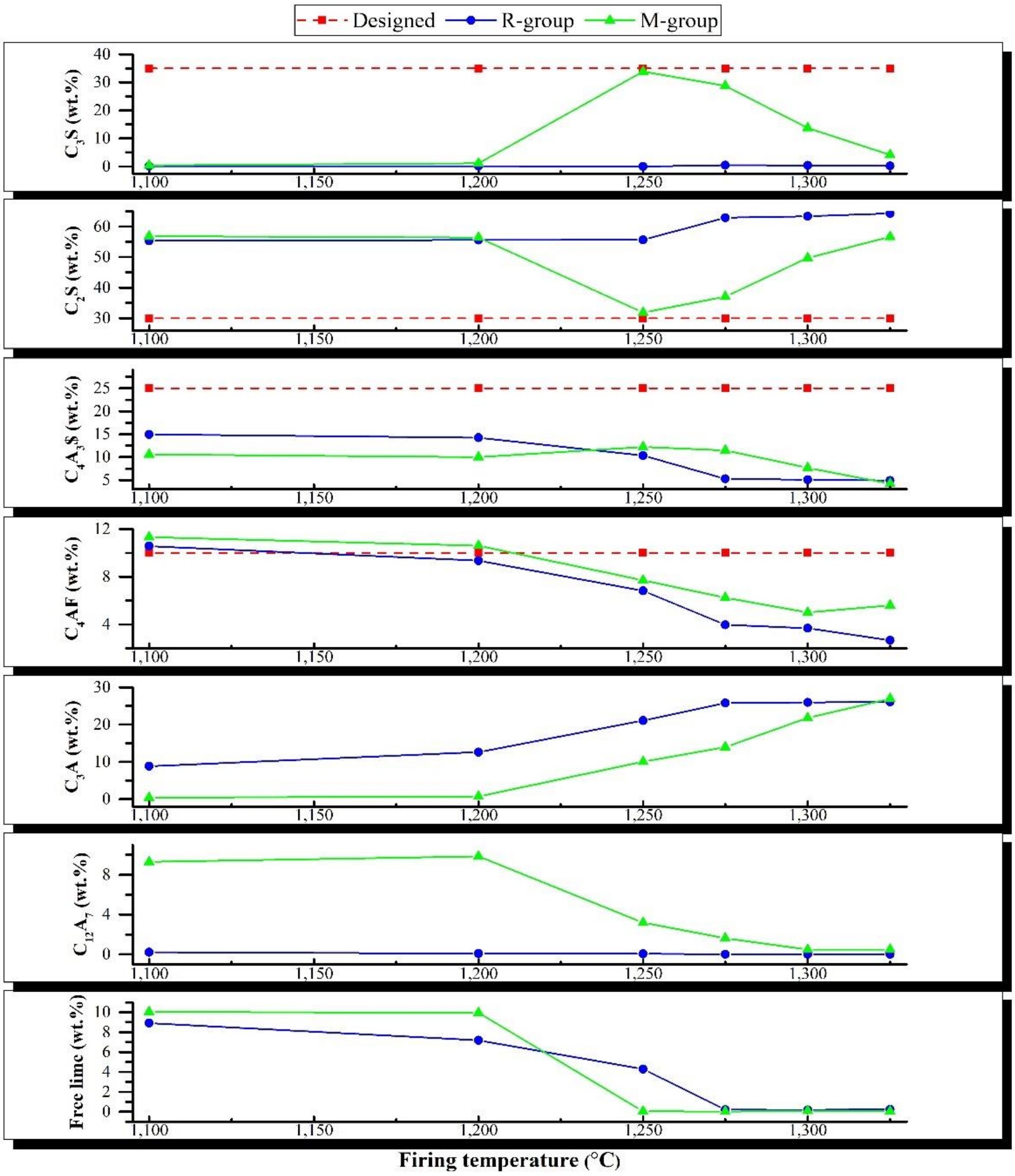

Figure 39 Variation of phases content with firing temperatures of Mix C

4.4.1 Effect of additives on clinker phase formation

For the R-group clinkers, the C_3S content was significantly lower than that of the designed content for all mixtures. A rich amount of free lime and C_2S content suggested that the C_3S phase could not fully form, even when the firing temperature increased to 1,325 °C [3]. However, when the samples were fired at 1,100 °C, the CaF_2 and CuO additives promoted C_3S formation by accelerating the reaction between C_2S and free lime. The $C_4A_3\bar{S}$ and C_4AF phase contents of the R-group samples and the M-group samples showed slight differences for all compositions. The unassigned phases of the C_3A content of the R-group samples were slightly lower than that of the M-group samples, while the $C_{12}A_7$ content was slightly higher than that of the M-group samples.

4.4.2 Effect of firing temperature on clinker phase formation

The phase quantitative analysis of the clinkers revealed that for all the compositions without additives, i.e. the R-group, very small amounts of C_3S phase were present when fired at low firing temperatures. Increasing the firing temperature from 1,100 °C to 1,325 °C also resulted in only a slight increment of the amount of C_3S present. The C_2S phase was a major phase component of all compositions (higher than 50 wt.%) in firings at 1,100 °C but increasing the firing temperature caused only a slight increase in the C_2S phase content. Nevertheless, the C_2S content was significantly higher than that of the designed content at all firing temperatures. This phenomenon differed from that seen in the M-group clinkers. For Mix A, the C_3S phase initially formed at firing temperature of 1,100 °C and then rapidly increased when the firing temperature increased, being higher than 50 wt.% when firing temperature exceeded 1,250 °C. For Mix B and Mix C, the C_3S content increased when the firing temperature increased and reached maximum content at firing temperature of 1,250 °C at which point the C_3S content value was close to that of the designed content. Thereafter, increasing the firing temperature caused C_3S content to decrease and C_2S content to increase. Content analysis showed that the $C_4A_3\bar{S}$ and C_4AF phases initially formed at 1,100 °C and tended to decrease with increased firing temperatures, accompanied with an increase of the unassigned C_3A and $C_{12}A_7$ phases. This point was observed for both Mix B and Mix C with additives. The decrease of C_4AF with temperature increase may be attributed to evaporation of Fe at high temperature, as shown in Table 15. In the case of $C_4A_3\bar{S}$, this is a significant point and is discussed in the next section.

4.4.3 C_3S polymorphic transformation

Normally, C_3S is the principal hydraulic phase of clinker and has a decisive impact on the strength of the cement [67]. Seven crystal structural modifications have been identified with enantiomorphic transformations as three triclinic (*T*), three monoclinic (M) and one rhombohedral (R). In most clinkers, the M_{I} and M_{III} phases are present at room temperature, but this is dependent on impurity content and heating and cooling history. One important aspect of previous investigations was that the M_{I} phase showed higher strength than M_{III} [1, 2, 4].

Significant quantities of C_3S phases were observed in the samples with additives, therefore this part of the discussion focuses on the M-group samples. In the Mix A clinkers, coexistent phases of M_{I}-C_3S and M_{III}-C_3S were observed. The M_{III}-C_3S content was distinctly higher than the M_{I}-C_3S content in all samples, independent of firing temperature. By contrast, the Mix B and Mix C clinkers fired below 1,250 °C had slightly more M_{III}-C_3S than M_{I}-C_3S but increasing the firing temperature resulted in more M_{I}-C_3S phase than M_{III}-C_3S phase.

Table 16 Quantity of phase analysis of Mix A clinkers fired at various temperatures calculated by the Rietveld refinement technique.

Phase (wt.%)	**Designed**	**Sample of Mix A (R-group)**					
		1,100 ˚C	**1,200** ˚C	**1,250** ˚C	**1,275** ˚C	**1,300** ˚C	**1,325** ˚C
M_{I}-C_3S		-	-	-	0.02	0.37	6.94
M_{III}-C_3S		-	-	-	0.11	0.12	1.27
C_3S_sum	55	-	-	-	0.13	0.49	8.21
α-C_2S		1.99	1.10	2.02	2.67	3.13	5.53
β-C_2S		64.29	64.52	60.85	62.28	63.25	58.92
γ-C_2S		0.22	0.68	3.23	2.38	2.60	1.96
C_2S_sum	30	66.50	66.30	66.10	67.33	68.98	66.41
$C_4A_3\bar{S}$	5	0.49	0.57	0.79	0.70	0.84	0.56
C_4AF	10	6.51	8.28	5.65	6.31	5.24	3.97
C_3A		9.17	7.77	9.27	8.84	8.14	7.37
$C_{12}A_7$		0.04	0.04	0.75	0.08	-	-
$C\bar{S}$		-	-	0.11	-	-	-
Free lime		12.90	16.39	14.14	15.90	15.58	12.90
R_{wp}		9.07	8.53	10.07	8.44	8.63	9.08
Phase (wt.%)	**Designed**	**Sample of Mix A (M-group)**					
		1,100˚C	**1,200˚C**	**1,250˚C**	**1,275˚C**	**1,300˚C**	**1,325˚C**
M_{I}-C_3S		5.52	9.69	16.07	24.13	22.83	29.17
M_{III}-C_3S		10.62	34.24	41.46	42.37	44.16	40.54
C_3S_sum	55	16.14	43.92	57.52	66.50	66.99	69.71
α-C_2S		0.39	0.36	0.71	0.20	0.08	0.77
β-C_2S		49.18	33.15	19.71	17.57	19.89	16.65
γ-C_2S		7.61	3.32	4.87	1.63	0.41	0.05
C_2S_sum	30	57.18	36.83	25.29	19.40	20.38	17.47
$C_4A_3\bar{S}$	5	0.99	0.87	0.54	0.40	0.39	0.17
C_4AF	10	6.56	5.84	5.25	6.22	5.66	6.09
C_3A		1.58	2.84	7.36	6.09	5.26	5.41
$C_{12}A_7$		1.18	1.28	0.42	-	-	0.02
$C\bar{S}$		0.03	-	-	-	-	0.02
Free lime		15.31	7.90	3.12	0.93	0.74	0.40
R_{wp}		7.76	7.64	7.47	7.26	7.49	7.38

Table 17 Quantity of phase analysis of Mix B clinkers fired at various temperatures calculated by the Rietveld refinement technique.

Phase (wt.%)	**Designed**	**Sample of Mix B (R-group)**					
		1,100 °C	**1,200 °C**	**1,250 °C**	**1,275 °C**	**1,300 °C**	**1,325 °C**
M_{I}-C_3S		-	-	-	0.24	0.35	0.18
M_{III}-C_3S		-	-	0.07	0.09	0.22	0.41
C_3S_sum	45	-	-	0.07	0.33	0.57	0.59
α-C_2S		1.71	1.10	1.67	2.79	3.48	4.22
β-C_2S		59.07	60.85	59.18	64.03	64.62	64.45
γ-C_2S		0.44	0.44	1.32	0.80	1.09	0.91
C_2S_sum	30	61.22	62.39	62.17	67.62	69.19	69.58
$C_4A_3\bar{S}$	15	6.55	3.91	1.76	1.06	1.10	1.01
C_4AF	10	9.86	8.85	7.16	5.02	3.92	2.88
C_3A		8.94	13.77	18.87	19.56	19.12	19.78
$C_{12}A_7$		0.23	0.06	0.04	-	-	-
$C\bar{S}$		0.07	0.18	0.78	0.09	0.07	0.07
Free lime		12.14	10.19	8.55	5.56	5.33	5.26
R_{wp}		7.54	7.82	7.76	8.65	9.20	10.12

Phase (wt.%)	**Designed**	**Sample of Mix B (M-group)**					
		1,100°C	**1,200°C**	**1,250°C**	**1,275°C**	**1,300°C**	**1,325°C**
M_{I}-C_3S		-	7.68	28.89	24.69	19.5	20.63
M_{III}-C_3S		4.75	11.15	15.68	13.47	10.67	9.66
C_3S_sum	45	4.75	18.83	44.58	38.16	30.37	30.29
α-C_2S		0.59	0.29	1.24	1.06	2.07	2.28
β-C_2S		47.51	43.33	25.66	33.82	41.50	49.95
γ-C_2S		11.55	6.79	4.09	2.56	0.91	0.69
C_2S_sum	30	59.65	50.41	30.99	37.44	44.48	43.92
$C_4A_3\bar{S}$	15	4.82	3.03	2.45	1.74	0.38	0.32
C_4AF	10	9.63	9.04	7.53	6.30	4.99	5.23
C_3A		0.30	2.90	12.76	15.17	18.87	19.55
$C_{12}A_7$		5.30	5.46	1.03	0.58	0.00	0.00
$C\bar{S}$		-	-	0.16	0.13	0.11	0.08
Free lime		14.96	9.6	0.18	0.03	0.11	0.07
R_{wp}		8.07	7.57	7.65	8.08	7.92	7.92

Table 18 Quantity of phase analysis of Mix C clinkers fired at various temperatures calculated by the Rietveld refinement technique.

Phase (wt.%)	**Designed**	**Sample of Mix C (R-group)**					
		1,100 ˚C	**1,200 ˚C**	**1,250 ˚C**	**1,275 ˚C**	**1,300 ˚C**	**1,325 ˚C**
M_{I}-C_3S		-	-	-	0.49	0.44	0.12
M_{III}-C_3S		-	-	-	-	-	0.11
C_3S_sum	35	-	-	-	0.49	0.44	0.23
α-C_2S		1.27	1.05	1.66	3.06	3.90	4.05
β-C_2S		53.67	54.19	52.77	58.7	58.36	59.19
γ-C_2S		0.39	0.37	1.19	1.10	1.07	1.02
C_2S_sum	30	55.33	55.61	55.62	62.86	63.33	64.26
$C_4A_3\bar{S}$	25	14.94	14.25	10.32	5.28	5.09	4.93
C_4AF	10	10.58	9.35	6.83	3.97	3.69	2.67
C_3A		8.81	12.60	21.08	25.79	25.93	26.08
$C_{12}A_7$		0.20	0.07	0.05	-	-	-
$C\bar{S}$		0.10	0.11	0.91	0.39	0.20	0.23
Free lime		8.91	7.18	4.29	0.21	0.19	0.25
R_{wp}		8.13	8.21	8.29	8.72	9.68	10.06

Phase (wt.%)	**Designed**	**Sample of Mix C (M-group)**					
		1,100˚C	**1,200˚C**	**1,250˚C**	**1,275˚C**	**1,300˚C**	**1,325˚C**
M_{I}-C_3S		-	-	23.47	19.18	8.51	1.85
M_{III}-C_3S		0.40	1.18	10.41	9.54	5.27	2.28
C_3S_sum	35	0.40	1.18	33.88	28.72	13.78	4.14
α-C_2S		0.81	0.84	1.23	0.91	2.70	3.21
β-C_2S		52.62	52.34	28.19	33.88	45.84	52.23
γ-C_2S		3.39	3.19	2.44	2.27	1.19	1.16
C_2S_sum	30	56.82	56.37	31.86	37.06	49.73	56.60
$C_4A_3\bar{S}$	25	10.59	9.99	12.23	11.47	7.69	4.17
C_4AF	10	11.33	10.60	7.70	6.24	5.01	5.61
C_3A		0.42	0.73	10.05	13.93	21.78	26.95
$C_{12}A_7$		9.28	9.86	3.18	1.61	0.46	0.47
$C\bar{S}$		0.16	0.21	0.19	0.13	0.51	0.79
Free lime		10.05	9.94	0.04	0.02	0.09	0.03
R_{wp}		8.98	9.57	7.91	8.01	7.87	8.76

Results in Table 16-Table 18 demonstrate that adding CaF_2 and CuO greatly influenced C_3S formation. Previous studies suggested that increasing the CaF_2 content of raw mix from 0 to 1 wt.% increased the reaction rate constant of the sample from 0.734×10^{-5} to 2.730×10^{-5} s^{-1} [68]. Thus, the CaF_2 additive improved the solid-diffusion rate of the reaction and lowered the formation temperature of the liquid phase [1]. The dissolution of CuO lowered the melting temperature and yielded a more liquid phase [23]. CuO also has the additional benefit of promoting consumption of CaO, thereby accelerating the formation and growth of C_3S [51]. Other studies reported that high $CaSO_4{\cdot}2H_2O$ content modified the C_3S crystalline phase from M_{III} to M_{I} [67]. However, compositions of the M-group that were fired at 1,250 °C appeared to be mostly close to the design for all mixture compositions. Table 19 lists the root mean square error (*RMSE*) values that were calculated by Eq.(4-1) to analyse the differences between obtained and designed compositions [69]. *RMSE* values near "0" denote a good fit performance. The formula for determining the *RMSE* is presented in Equation below[69]. All the M-group samples showed lowest *RMSE* values when they were fired at 1,250 °C. This suggested that the optimal firing temperature was 1,250 °C.

$$RMSE = \sqrt{\frac{1}{N}\sum_{i=1}^{N}(t_i - td_i)^2} \qquad \text{Eq.(4-1)}$$

Where t_i is the experimental value of the considered sample, td_i is the output predicted value and N is the total number of observed samples.

Table 19 *RMSE* values of Mix A, Mix B, and Mix C

Mixture	Condition	RMSE					
		1,100 °C	1,200 °C	1,250 °C	1,275 °C	1,300 °C	1,325 °C
Mix A	R-group	24.08	24.22	24.10	24.41	24.60	21.77
	M-group	17.73	5.87	4.11	6.30	6.17	7.43
Mix B	R-group	20.28	20.89	21.41	22.48	22.73	22.92
	M-group	18.89	13.12	6.41	8.08	11.28	11.35
Mix C	R-group	16.25	16.57	17.93	20.50	20.66	20.97
	M-group	17.00	16.81	5.96	7.77	14.31	18.84

4.5 Influence of sulfur on ye'elimite formation

Table 16-Table 18 show $C_4A_3\overline{S}$ content formed at low temperature. This content was significantly lower than expected based on the phase composition design. These tables also show that as the firing temperature increased, C_3A content also increased, while $C_4A_3\overline{S}$ and $C_{12}A_7$ content decreased. One possible explanation for this behaviour was evaporation of sulfur from both the $CaSO_4{\cdot}2H_2O$ and the $C_4A_3\overline{S}$ phases at high temperature [16]. When the LOI test was run on $CaSO_4{\cdot}2H_2O$ at 1,250 °C for 30 minutes, the result was 21.99%. This clearly indicated the loss of sulfur content. At high temperature, C_3A may no longer be formed from $C_{12}A_7$ as usual but rather the observed sulfur loss causes C_3A to be formed from $C_4A_3\overline{S}$. After evaporation, there may not be enough sulfur available to form $C_4A_3\overline{S}$ [16]. To investigate the possible benefit from loading the raw materials with extra $CaSO_4{\cdot}2H_2O$ to increase sulfur content, two trials were run with an additional 50% and 100% of the original $CaSO_4{\cdot}2H_2O$ content. These mixtures were called Mix C-M + $0.5x$ SO_3 and Mix C-M + $1x$ SO_3 respectively. Both of these experimental high sulfur mixtures were then fired at 1,250 °C for 30 minutes, as before.

The XRD patterns of Mix C (M-group), Mix C-M + $0.5x$ SO_3 and Mix C-M + $1x$ SO_3 are presented in Figure 40. Results showed obvious C_3A and $C_{12}A_7$ peaks in the Mix C (M-group). Peak intensities of C_3A and $C_{12}A_7$ significantly decreased for samples with added SO_3 at $0.5x$ and $1x$. The XRD patterns of these mixtures were used to investigate phase quantitative analysis by the Rietveld refinement technique (Table 20).

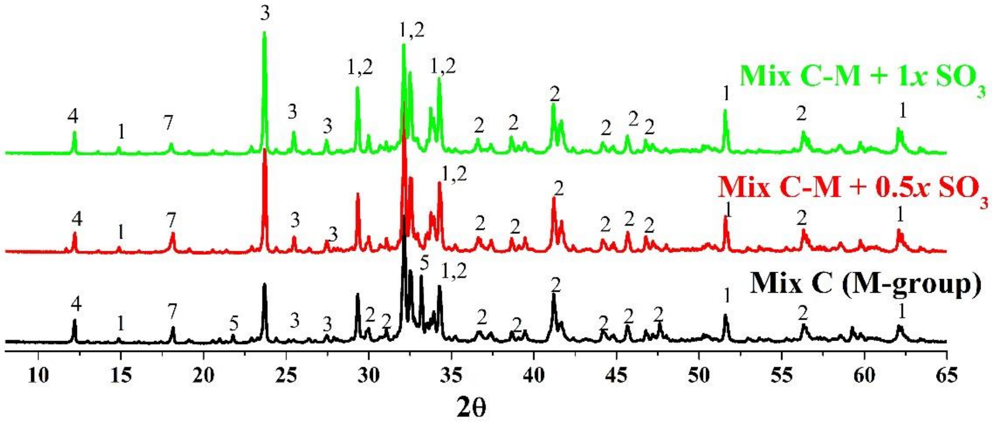

Figure 40 XRD patterns with and without excess SO_3 of Mix C at 1,250 °C: 1 = C_3S, 2 = C_2S, 3 = $C_4A_3\bar{S}$, 4 = C_4AF, 5 = C_3A, 6 = free lime, 7 = $C_{12}A_7$

The $C_4A_3\bar{S}$ content increased to 23.12 wt.% in the sample with 1*x* SO_3 excess. Moreover, amounts of unassigned phases of C_3A, and $C_{12}A_7$ were substantially reduced. These observations suggested that C_3A and $C_{12}A_7$ phases were transformed to $C_4A_3\bar{S}$. The 1*x* SO_3 excess showed the content of $C_4A_3\bar{S}$ to be the nearest to the designed composition, while excess SO_3 content decreased the C_2S and increased the C_3S content [67].

Table 20 Design phase compositions and clinkers with excess sulfur fired at 1,250 C of Mix C (M-group), Mix C-M + 0.5*x* SO_3 and Mix C-M + 1*x* SO_3.

Phase composition	Mix C			
	Designed (wt.%)	Non-excess SO_3 (wt.%)	0.5*x* SO_3 (wt.%)	1*x* SO_3 (wt.%)
C_3S	35	33.88	34.54	38.78
C_2S	30	31.86	29.77	24.38
$C_4A_3\bar{S}$	25	12.23	19.27	23.12
C_4AF	10	7.70	7.73	7.45
C_3A	-	10.05	0.01	0.00
$C_{12}A_7$	-	3.18	3.23	0.02
$C\bar{S}$	-	0.19	1.70	3.61
Free lime	-	0.04	2.18	1.46

Table 21 shows the atomic ratios of each phase. These ratios were calculated from the EDS data. Morphological features as fractured surfaces of the sample clinkers can be seen in the SEM images shown in Figure 41. Figure 41(a) shows the formation of C_3A phase in Mix C (M-group). The prismatic particles in Mix C are C_3A (~7 μm) and the rounded particles are C_2S (<5 μm). Figure 41(b) shows Mix C-M

+ 1*x* SO_3 where the rhombic particles are $C_4A_3\bar{S}$ (<7 μm), the prismatic particles are C_3S (~5 μm) and the plate-shaped particles are C_4AF (~3 μm). Comparing Figure 41(a) and Figure 41(b), increasing the SO_3 proportion in the raw materials of Mix C (M-group) prevented the unwanted phases from forming and instead produced the target phases. Figure 41(c) is the same SEM image as Figure 41(b) but the added orange frame shows the portion of the image which was analysed for element distribution. Results of the element distribution analysis are shown in Figure 41(d) and these agreed with the EDS analysis results. Neither the element distribution analysis nor the EDS analysis found any fluorine or copper.

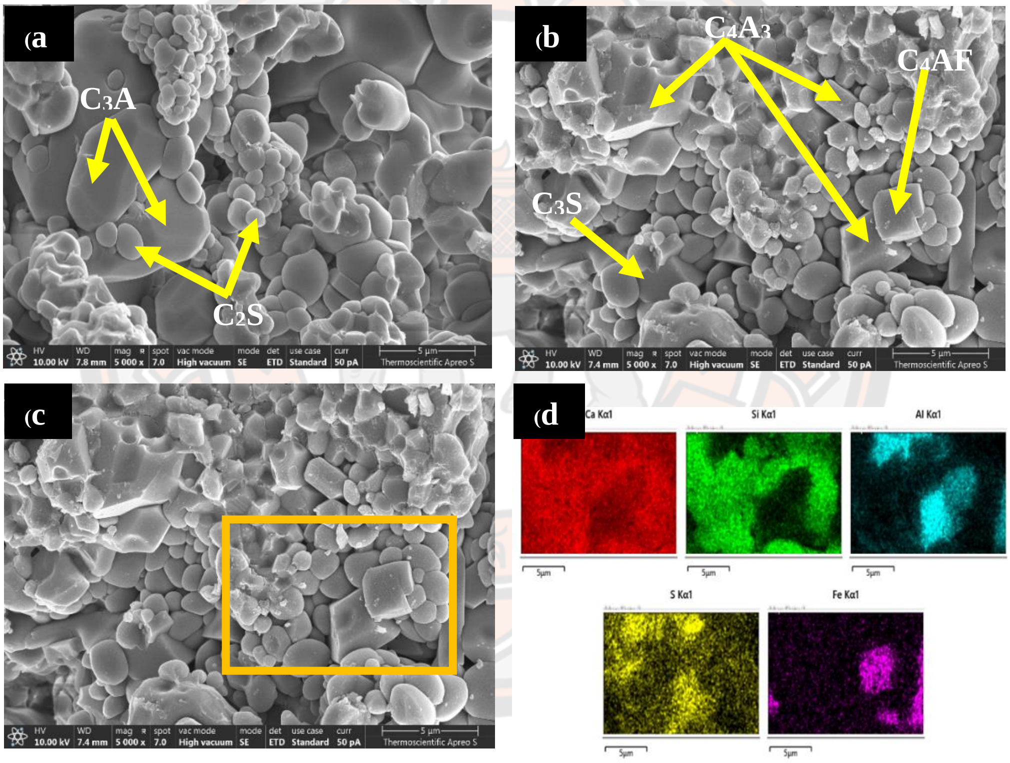

Figure 41 SEM images of (a) Mix C (M-group), (b) Mix C-M + 1*x* SO_3
(c) Elemental mapping area of Mix C-M + 1*x* SO_3, and (d) Element distribution of Mix C-M + 1*x* SO_3

Table 21 Atomic ratios of sample clinker phases as calculated from EDS data. The corresponding theoretical atomic ratio of each clinker phase is included in parentheses.

Phase	Atomic ratio			
	Ca/Si	Ca/Al	Ca/S	Ca/Fe
Experimental EDS ratios				
C_3S	2.74 (3.00)	-	-	-
C_2S	1.90 (2.00)	-	-	-
$C_4A_3\overline{S}$	-	0.80 (0.67)	4.08 (4.00)	-
C_4AF	-	1.75 (2.00)	-	2.28 (2.00)
C_3A	-	1.51 (1.50)	-	-

CHAPTER V THE RESULTS PART II: Fabrication and characterisation of 0–3 KNLNTS piezoelectric ceramic/alite calcium sulphoaluminate cement composites

5.1 KNLNTS ceramics

5.1.1 KNLNTS calcined powders

The XRD patterns of KNLNTS calcined powders burned at temperatures ranging from 650 to 900 degrees Celsius are shown in Figure 42. The XRD patterns reveal a perovskite structure for all samples that matched the Joint Committee on Powder Diffraction Standard (JCPDS) files no. 71-2171 and 71-0945 [29]. The small impurity peaks of the Ta_2O_5 and Nb_2O_5 raw materials were observed for the sample calcined at 650^{o}C. This is due to an incomplete reaction in the calcination process because of insufficient energy being supplied. By increasing the firing temperature, the intensity peaks of the raw materials disappeared, accompanied by an increase in the intensity of the perovskite peaks. However, for the samples calcined with firing temperatures in range of 750°C to 900°C, diffraction peaks of the secondary impurities phase $N_6Nb_{10}O_{30}$ appeared immediately. Additionally, the phase formation of the KNLNTS powders calcined at 650°C displayed an orthorhombic structure according to JCPDS 71-2171. The orthorhombic structure was subsequently transformed to tetragonal structures when the calcined temperature increased from 750°C to 900°C. The percentage of the perovskite phase was calculated using the relative quantities of perovskite and the secondary phase. The perovskite percentage was approximately 80% to 92% for the samples calcined between 650°C to 900°C (Table 22). The highest perovskite percentage was 92%, which was found in the sample calcined at 750°C. Therefore, the KNLNTS powders calcined at 750°C was selected as raw materials to prepare the KNLNTS ceramics in next step.

$$\text{Percent perovskite phase} = \frac{I_{perov}}{I_{perov} + I_{impurities}} \qquad \text{Eq.(5-1)}$$

where I_{perove} is the intensity of the perovskite phase

$I_{\text{impurities}}$ is the intensity of the impurities phase

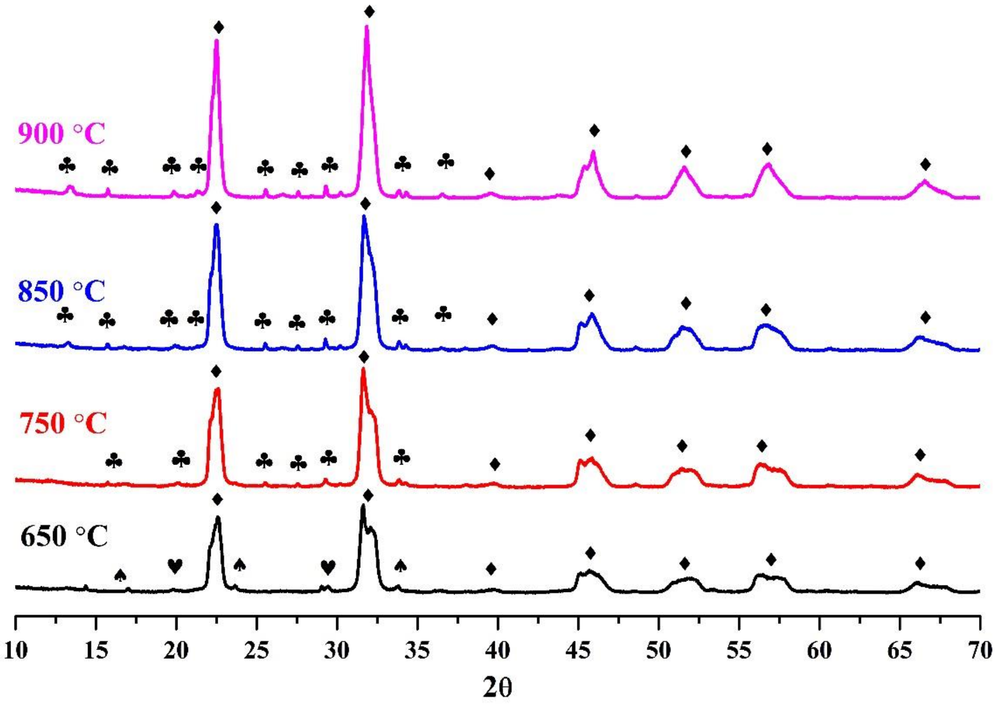

Figure 42 XRD patterns of KNLNTS powders calcined at 650 – 900 °C; ♦ = Perovskite, ♥ = Ta_2O_3, ♠ = Nb_2O_3, ♣ = $K_6Nb_{10}O_{30}$.

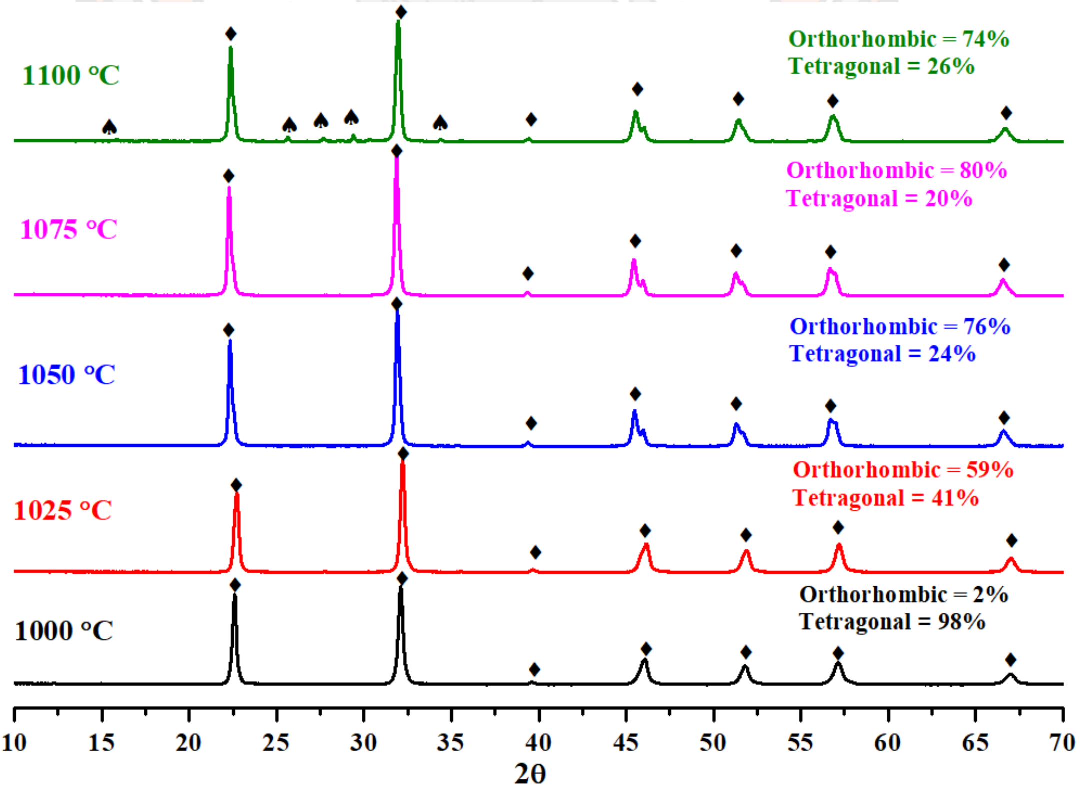

Figure 43 XRD patterns of KNLNTS ceramics sintered at 1000 – 1100 °C; ♦ = Perovskite, ♠ = Nb_2O_3.

Table 22 Percent perovskite phase of the KNLNTS calcined powders and the KNLNTS sintered ceramics.

	Firing temperature (°C)	Percent perovskite phase (%)
Calcined powders	650	80
	750	92
	850	85
	900	85
Sintered ceramics	1000	100
	1025	100
	1050	100
	1075	100
	1100	94

5.1.2 KNLNTS sintered ceramics

After the KNLNTS powders were calcined at 750°C for 6 hours, the calcined powders were mixed with the sintered aids agents and then pressed and sintered at sintering temperatures ranging from 1,000°C to 1100°C. Figure 43 presents the XRD patterns of the sintered KNLNTS ceramics. The pure perovskite structure was obtained from the samples sintered at 1000°C to 1075°C. The secondary impurity phase of Nb_2O_5 appeared when the sintering temperature was increased to 1100°C. The Rietveld refinement technique was used to investigate the fraction of KNN perovskite structure shown in Figure 43. The structural model was based on an orthorhombic (space group; Amm2) and tetragonal phase (space group; P4mm) of the KNN perovskite structure that corresponds to the crystallography open database (COD) no. 2300499 and 2104294, respectively. The structural phase was indexed as tetragonal higher than orthorhombic perovskite structures for the samples sintered below 1050°C. Increasing the sintering temperature to 1075 °C affected the crystal structure which distorted from tetragonal to an orthorhombic crystal. The highest content of orthorhombic crystal was found in sample sintered at 1075 °C. After the sintered temperature increase to 1100 °C, the content of orthorhombic crystal tends to slightly decrease.

Figure 44 (a)-(e) shows the surface morphologies of the KNLNTS ceramics sintered variously at 1000°C, 1025°C, 1050°C, 1075°C, and 1100°C. A small grain size with a formless shape was observed from the sample sintered at 1000^{o}C (Figure 44 (a)). As the sintered temperature rose, the grain shape began to take shape and the average grain size suddenly increased, as shown in Figure 44 (b)-(c). The cuboid-like grains with the largest average grainsize are seen in the sample sintered at 1075^{o}C (Figure 44 (d)). However, Figure 44 (e) illustrates that increasing the sintering temperature to 1100^{o}C caused the grains boundary to melt, and little grains combine to form larger grains.

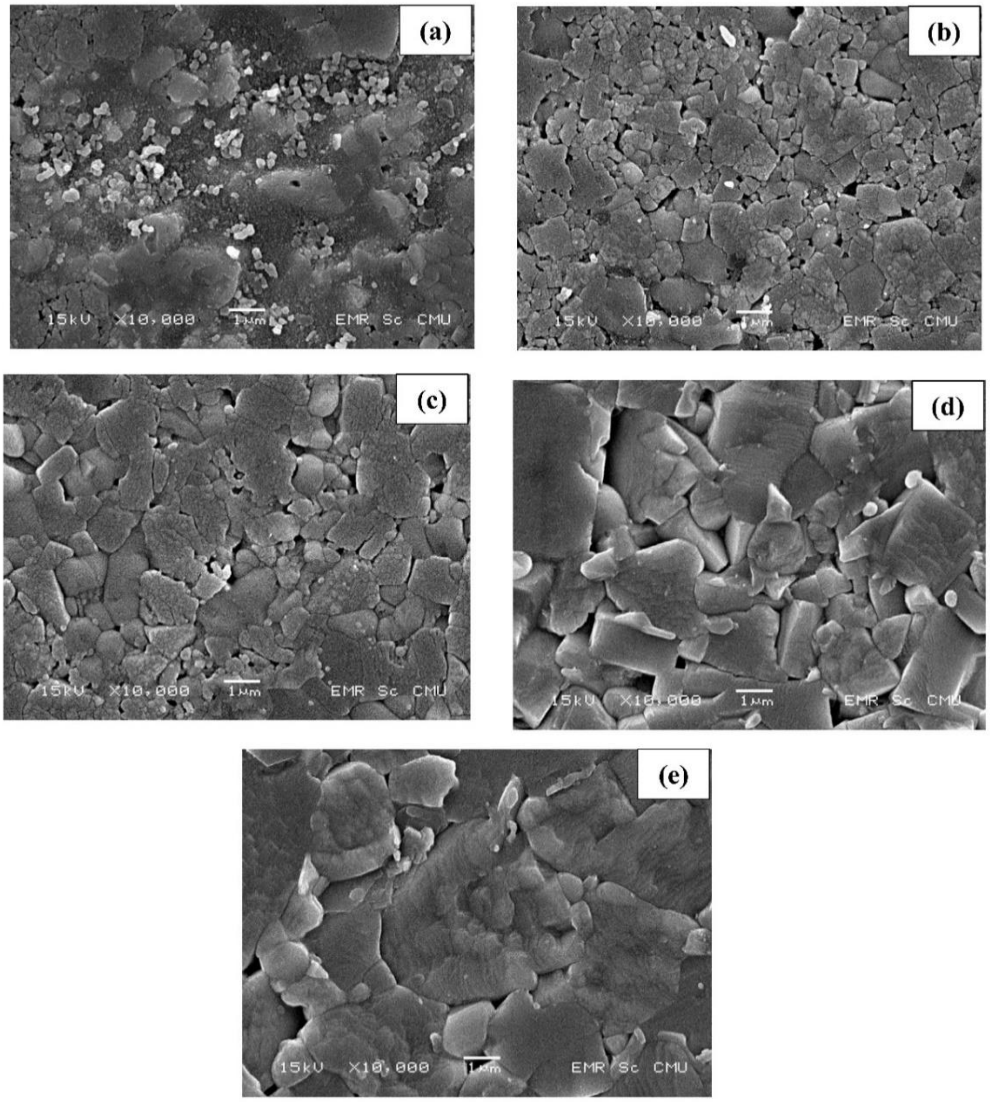

Figure 44 SEM images of the pellet surface sintered at (a) 1000°C, (b) 1025°C, (c) 1050°C, (d) 1075°C, and (e) 1100°C.

The dielectric properties of the poled ceramics at room temperature were investigated, with the results summarised in Figure 45 and Table 23. For KNLNTS ceramics sintered at 1000^{o}C and 1025^{o}C, the dielectric constant and dielectric loss curves exhibited anomalous behaviour which can be attributed to incomplete formation of grains in the KNLNTS ceramics. This can be identified by their surface morphologies, as shown in Figure 44 (a) and (b). The temperature dependence of the dielectric constant for the KNLNTS ceramics displayed a strong dielectric peak at the Curie temperature. The ceramics also exhibited a dense microstructure, as shown in (Figure 44 (c) – (e)). The dielectric constant and dielectric loss at room temperature and Curie temperature are listed in Table 23. The maximum dielectric constant at room temperature was obtained from the sample sintered at 1100^{o}C, while the highest dielectric constant at Curie temperature was observed in the sample sintered at 1075^{o}C. The curie temperature tended to increase with an increase of sintering temperature. However, the dielectric loss at room temperature of the ceramics sintered at 1100^{o}C was significantly higher than for the other samples. The piezoelectric coefficient of the KNLNTS sintered ceramics which were fired at various firing temperatures ranging from 1000°C to 1100°C are listed in Table 23, which shows that the piezoelectric coefficient increased from 61 pC/N to 118 pC/N when the sintering temperature increased from 1000°C to 1075°C. However, the piezoelectric coefficient of KNLNTS ceramic sintered at 1100°C slightly decreased because the grain boundaries in the ceramics began to melt. This suggests that when there was an increase of the sintering temperature from 1000°C to 1075°C, the dielectric constant at curie temperature and piezoelectric coefficient tend to increase. On the other hand, after the sintered temperature up to 1100°C the dielectric constant at curie temperature and piezoelectric coefficient were slightly decreased. These result corresponding with the fraction of orthorhombic and tetragonal crystal in the ceramics from the XRD. This demonstrated that the samples with high content of orthorhombic crystal are able to deliver good dielectric constant at curie temperature and piezoelectric coefficient[29].

From the phase impurities, microstructure, and dielectric properties results, it can be concluded that the KNLNTS ceramics sintered at 1075°C present the pure perovskite phase with clear grain boundaries and large grain size, and they also showed optimal satisfactory dielectric properties. This sintering condition was therefore selected to prepare the KNLNTS/ACSA cement composite in the following section.

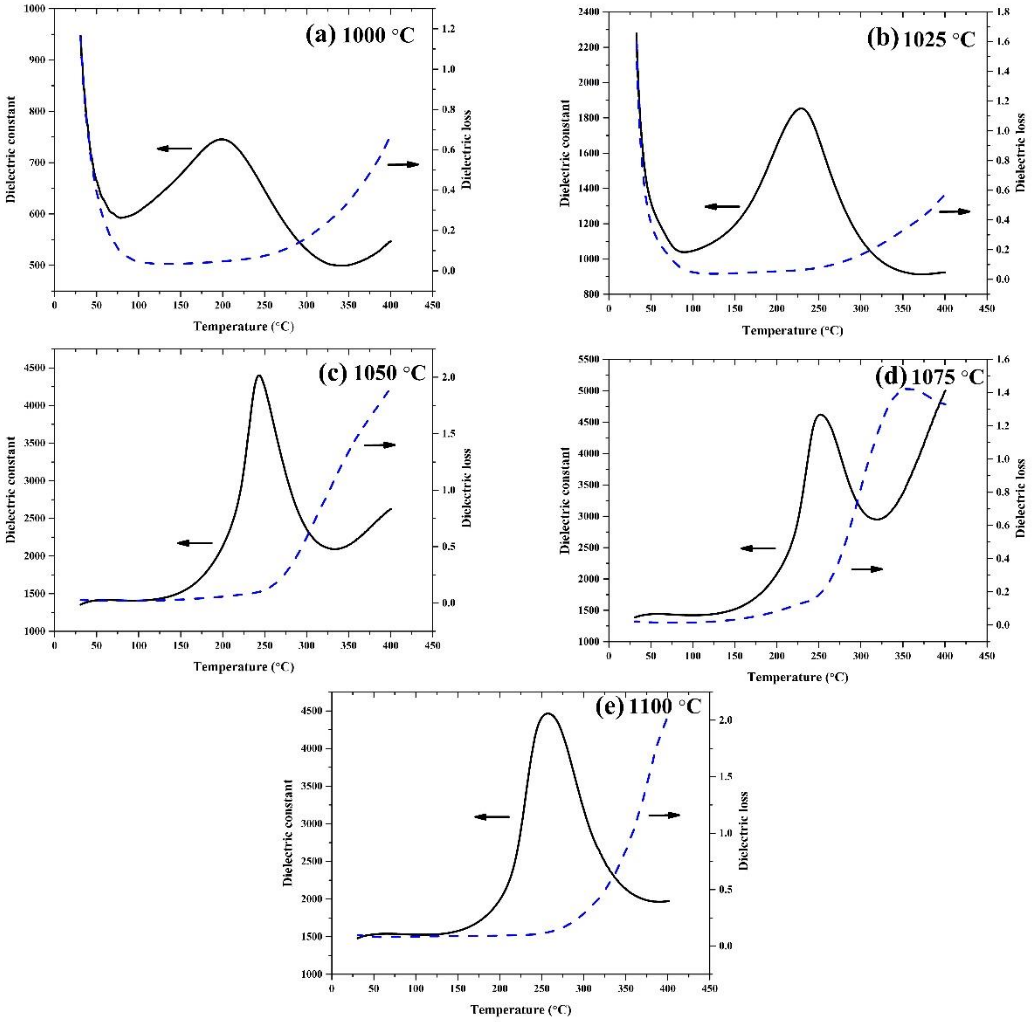

Figure 45 The temperature dependence of dielectric properties of KNLNTS ceramics sintered at (a) 1000°C, (b) 1025°C, (c) 1050°C, (d) 1075°C, and (e) 1100°C.

Table 23 The dielectric properties and piezoelectric coefficient of the KNLNTS ceramics.

Sintered temperature (°C)	Dielectric constant at room temperature	Dielectric loss at room temperature	Curie temperature (°C)	Dielectric constant at Curie temperature	Dielectric loss at Curie temperature	d_{33} (pC/N)
1000	-	-	198	745	0.046	61
1025	-	-	228	1853	0.063	72
1050	1354	0.028	242	4399	0.096	113
1075	1386	0.022	251	4622	0.188	118
1100	1479	0.098	257	4464	0.122	105

5.2 KNLNTS/ACSA cement composite

5.2.1 Density and acoustic impedance

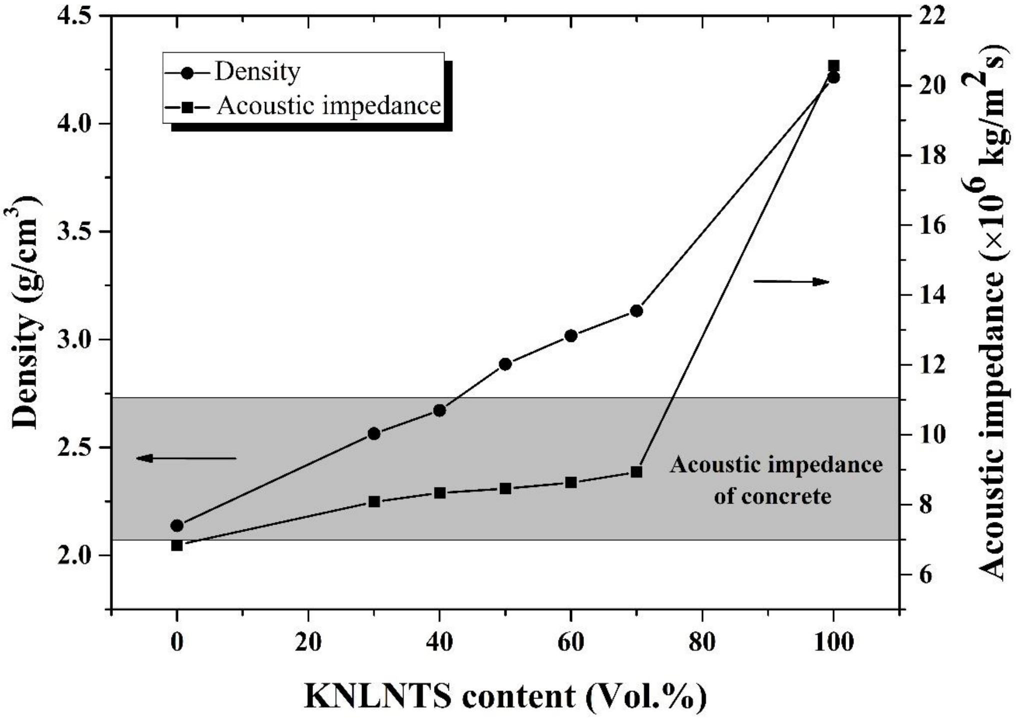

Figure 46 The density and acoustic impedance of KNLNTS/ACSA cement composite.

The dependency between density and acoustic impedance of the KNLNTS/ACSA cement composites with various KNLNTS fractions are presented in

Figure 46 which illustrates that with increasing KNLNTS content, the density and acoustic impedance of composites also increased.

Higher density associated with increased KNLNTS content was caused by the specific gravity of the KNLNTS ceramics being greater than that of the hardened ACSA paste. The acoustic impedance results suggest that the KNLNTS/ACSA cement composites with 30-70 vol.% of KNLNTS ceramics are suitable for use as piezoelectric sensors for OPC concrete due to the matching acoustic impedance range (6.90-11.23 × 10^6 kg/m^2s) [70].

5.2.2 Microstructure analysis

The typical SEM micrographs of the 0-3 connectivity of KNLNTS/ACSA cement composites of 30 vol.% of KNLNTS and 70 vol.% of KNLNTS ceramics can be seen in Figure 47 and Figure 48, respectively. The SEM micrographs illustrate a typical interfacial transition zone (ITZ) between the KNLNTS ceramics powders and the ACSA hardened cement matrixes. In the case of 30 vol.% KNLNTS ceramics (Figure 47 (a)), the KNLNTS ceramics particle bound well with the cement matrix. For the 70 vol.% KNLNTS ceramics (Figure 48 (a)), the ITZ between the KNLNTS ceramic particles and the cement matrix exhibited poor interface bonding performance between the ceramic and the cement matrix due to higher porosity compared to the sample with 30 vol.% of KNLNTS. Elemental mapping of niobium (Nb) and Calcium (Ca) are shown in Figure 47 (b) and Figure 48 (b). This exhibits the position of ceramic and cement matrix in the composite. The EDS spectra of composite (Figure 47 (c)-(d)) and Figure 48 (c)-(d)) show that niobium is the main element of the KNLNTS ceramics. Additionally, calcium was identified as the primary component of cement hydration.

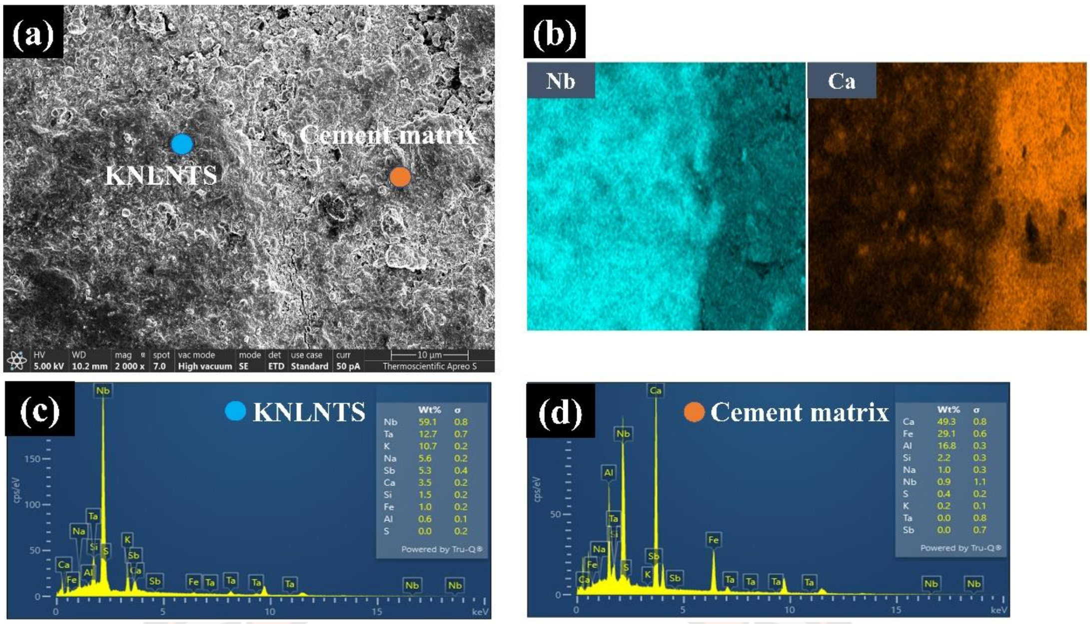

(c) KNLNTS

	Wt%	σ
Nb	59.1	0.8
Ta	12.7	0.7
K	10.7	0.2
Na	5.6	0.2
Sb	5.3	0.4
Ca	3.5	0.2
Si	1.5	0.2
Fe	1.0	0.2
Al	0.6	0.1
S	0.0	0.2

(d) Cement matrix

	Wt%	σ
Ca	49.3	0.8
Fe	29.1	0.6
Al	16.8	0.3
Si	2.2	0.3
Na	1.0	0.3
Nb	0.9	1.1
S	0.4	0.2
K	0.2	0.1
Ta	0.0	0.8
Sb	0.0	0.7

Figure 47 Microstructure of 0-3 connectivity KNLNTS/ACSA cement composites with KNLNTS content of 30 vol.%: (a) SEM micrograph; (b) element mapping for Nb and Ca in composite; (c) EDS analysis of the KNLNTS ceramics phase; and (d) EDS analysis of the cement matrix phase.

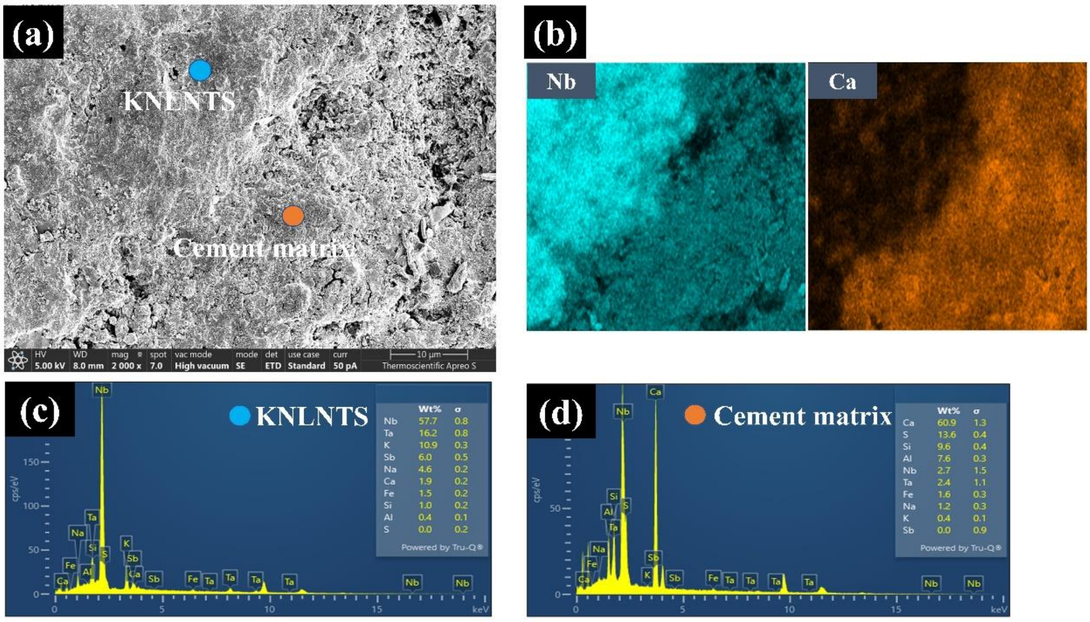

(c) KNLNTS

	Wt%	σ
Nb	57.7	0.8
Ta	16.2	0.8
K	10.9	0.3
Sb	6.0	0.5
Na	4.6	0.2
Ca	1.9	0.2
Fe	1.5	0.2
Si	1.0	0.2
Al	0.4	0.1
S	0.0	0.2

(d) Cement matrix

	Wt%	σ
Ca	60.9	1.3
S	13.6	0.4
Si	9.6	0.4
Al	7.6	0.3
Nb	2.7	1.5
Ta	2.4	1.1
Fe	1.6	0.3
Na	1.2	0.3
K	0.4	0.1
Sb	0.0	0.9

Figure 48 Microstructure of 0-3 connectivity KNLNTS/ACSA cement composite with KNLNTS content of 70 vol.%: (a) SEM micrograph; (b) element mapping for Nb and Ca in composite; (c) EDS analysis of the KNLNTS ceramics phase; and (d) EDS analysis of the cement matrix phase.

5.2.3 Effect of KNLNTS content on dielectric and piezoelectric properties

The relationships between the relative dielectric constant and loss measured at 1 kHz, 28 days after polarisation, and at room temperature are represented in Figure 49. The experimental results demonstrate that the dielectric constant of the KNLNTS/ACSA cement composite tended to increase and were accompanied by a decrease in dielectric loss with increased KNLNTS volume. This was mostly owing to the conductivity of the cement matrix (such as OH^-, Ca^{2+}, and Al^{3+}) , which reduced dielectric loss [59, 71]. A high improvement of dielectric properties from increased KNLNTS ceramics fraction was based on the contribution of ions and electron polarisation of the composites. The mathematical equation of the cube model, parallel model, and series model for the dielectric constant of composite materials (ε_c) [70] with various KNLNTS content was calculated by Eq.(5-2)-Eq.(5-4) and then plotted in Figure 49. The experimental results are consistent with the theoretical cube model, indicating that the ceramic particles in the composites are uniformly distributed.

Cube model; $\varepsilon_c = \frac{\varepsilon_1 \cdot \varepsilon_2}{(\varepsilon_2 - \varepsilon_1) \cdot v_1{}^{-1/3} + \varepsilon_1 \cdot v_1{}^{-2/3}} + \varepsilon_2 \cdot (1 - v_1{}^{2/3})$ Eq.(5-2)

Parallel model: $\varepsilon_c = v_1 \varepsilon_1 + v_2 \varepsilon_2$ Eq.(5-3)

Series model: $\varepsilon_c = \frac{\varepsilon_1 \cdot \varepsilon_2}{v_1 \varepsilon_2 + v_2 \varepsilon_1}$ Eq.(5-4)

where ε_1 is the dielectric constant of the KNLNTS ceramics, ε_2 is the dielectric constant of the cement matrixes, and v_1 is the volume percentage of the KNLNTS ceramics.

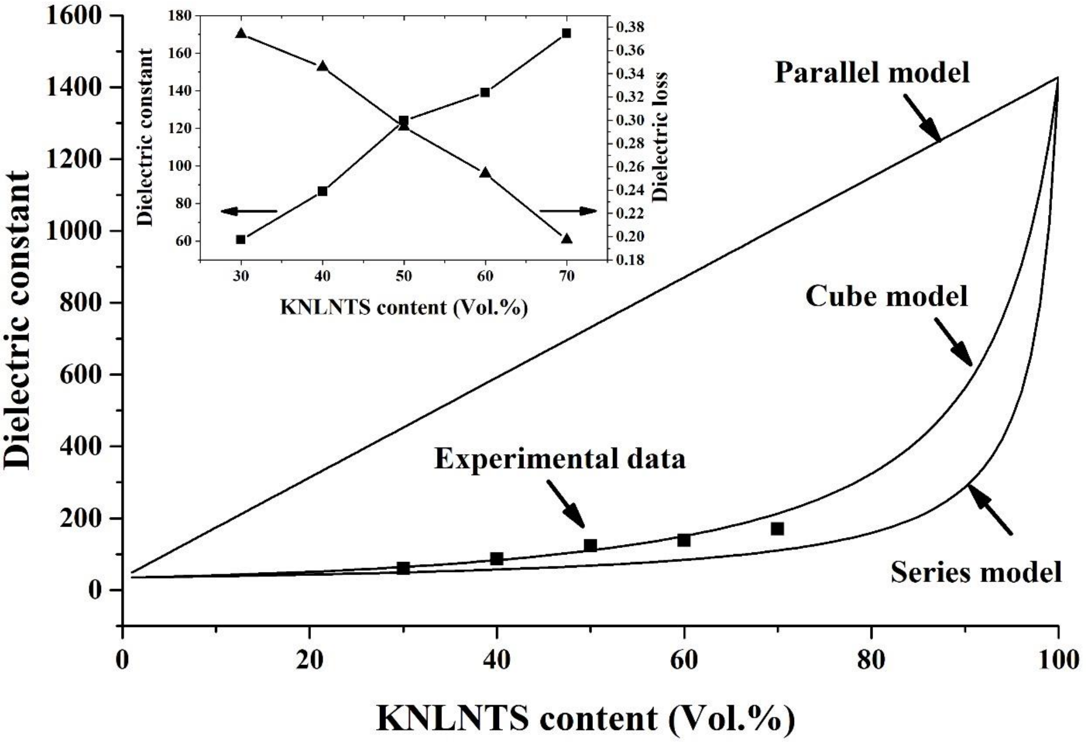

Figure 49 Comparison of the dielectric constant from the experimental data and the numerical model for 0-3 KNLNTS/ACSA cement composites.

Figure 50 presents the experimental results of the piezoelectric coefficient (d_{33}) of the 0-3 KNLNTS/ACSA cement composites after polling for 28 days. This shows that the piezoelectric coefficient is highly influenced by the KNLNTS ceramic content. This relationship is due to the density of charges on the surface of piezoelectric composites per unit area when they are stressed by an applied electric field. [72]. The effects of KNLNTS content on the piezoelectric coefficient of the KNLNTS/ACSA cement composite were compared with the cube model, parallel model, and series model (Eq.(5-5)-Eq.(5-7)), as illustrated in Figure 50. The experimental results are slightly higher than that of the theoretical value of the cube model. Therefore, the KNLNTS ceramic particles in the composites are dispersed as 0-3 connectivity.

Cube model; $$d_{33} = d_{33}^{1} \cdot \frac{v_1}{v_1^{1/3}+\left(1-v_1^{1/3}\right)\cdot\frac{\varepsilon_1}{\varepsilon_2}} \cdot \frac{1}{1-v_1^{1/3}+v_1} \qquad \text{Eq.(5-5)}$$

Parallel model: $$d_{33} = \frac{v_1 \cdot d^1_{33} \cdot S^2_{33} + v_2 \cdot d^2_{33} \cdot S^1_{33}}{v_1 S^2_{33} + v_2 S^1_{33}} \quad \text{Eq.(5-6)}$$

Series model: $$d_{33} = \frac{v_1 \cdot d^1_{33} \cdot \varepsilon_2 + v_2 \cdot d^2_{33} \cdot \varepsilon_1}{v_1 \varepsilon_2 + v_2 \varepsilon_1} \quad \text{Eq.(5-7)}$$

where d^1_{33} is the piezoelectric coefficient of the ceramics, ε_1 is the dielectric constant of the KNLNTS ceramics, ε_2 is the dielectric constant of the cement matrixes, and v_1 is the volume percentage of the ceramics.

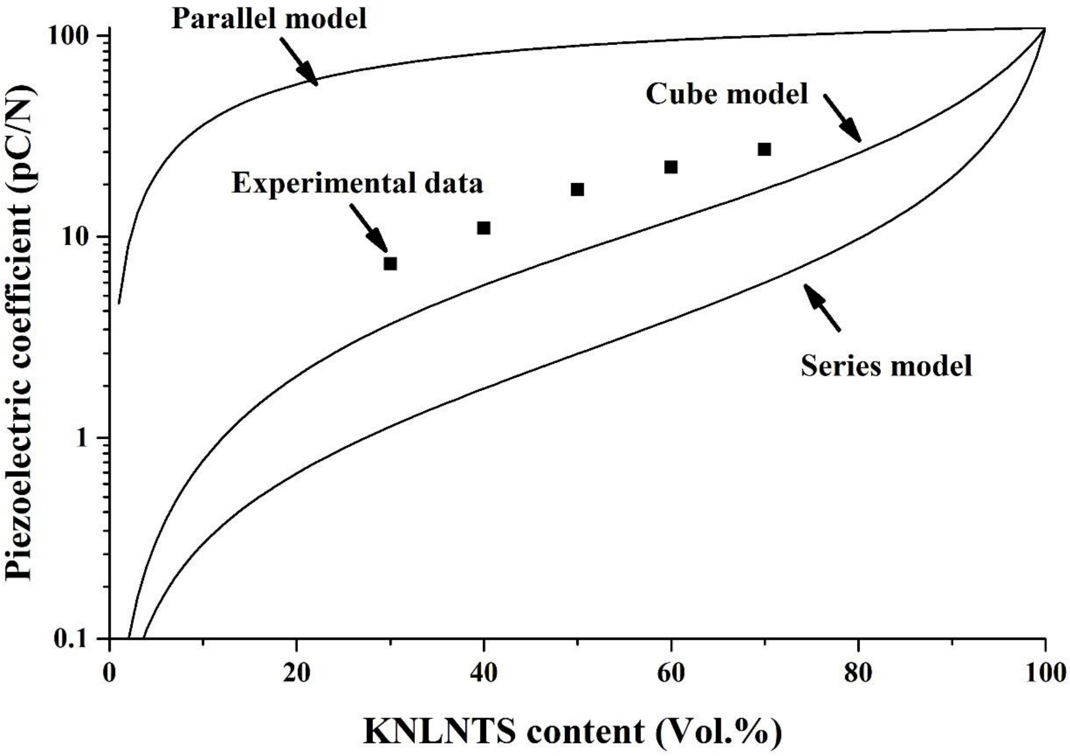

Figure 50 Comparison of the piezoelectric coefficient from experimental data and the numerical model for 0-3 KNLNTS/ACSA cement composites.

Figure 51 presents the experimental results of the piezoelectric voltage factor (g_{33}) of the 0-3 KNLNTS/ACSA cement composites after polling for 28 days. The piezoelectric voltage factor is the sensitivity of a receiving voltage and was calculated by Eq.(5-8). The results show that the piezoelectric voltage factor value increased slightly in line with increased KNLNTS. The primary reason is that the greater rate increase of the piezoelectric coefficient than that of dielectric constant. The results of

g_{33} values of the 0-3 KNLNTS-ACSA cement composites are plotted against KNLNTS content with cube model, parallel model, and series model (Eq.(5-9)-Eq.(5-11)). The experimental results can be seen to increase with increasing KNLNTS content similar to the trend of cube model. Besides, comparing this result with the pure piezoelectric ceramic, the g_{33} value of the composites increases significantly because of the greater increase trend of the d_{33} of the composites when compare with the dielectric constant value, which indicates that the piezoelectric composites have good receiving sensitivity.

piezoelectric voltage factor: $g_{33} = \frac{d_{33}}{\varepsilon_r \cdot \varepsilon_0}$ Eq.(5-8)

Cube model:

$$g_{33} = \frac{d_{33}^{1} v_1}{(v_1^{\frac{1}{3}} + \left(1 - v_1^{\frac{1}{3}}\right) \cdot \frac{\varepsilon_1}{\varepsilon_2})} \cdot \frac{1}{1 - v_1^{1/3} + v_1} \text{ x } \frac{(\varepsilon_2 - \varepsilon_1) v_1^{-\frac{1}{3}} + \varepsilon_1 v_1^{-\frac{2}{3}}}{\varepsilon_1 \varepsilon_2 + \left[\varepsilon_2 \left(1 - v_1^{\frac{2}{3}}\right)\right] [(\varepsilon_2 - \varepsilon_1) v_1^{-\frac{1}{3}} + \varepsilon_1 v_1^{-\frac{2}{3}}]} \quad \text{Eq.(5-9)}$$

Parallel model:
$$g_{33} = \frac{v_1 \cdot d_{33}^{1} \cdot S_{33}^{2} + v_2 \cdot d_{33}^{2} \cdot S_{33}^{1}}{(v_1 S_{33}^{2} + v_2 S_{33}^{1})(v_1 \varepsilon_1 + v_2 \varepsilon_2)} \quad \text{Eq.(5-10)}$$

Series model:
$$g_{33} = \frac{v_1 \cdot d_{33}^{1}}{\varepsilon_1} + \frac{v_2 \cdot d_{33}^{2}}{\varepsilon_2} \quad \text{Eq.(5-11)}$$

where d^1_{33} is the piezoelectric coefficient of the ceramics, ε_1 is the dielectric constant of the KNLNTS ceramics, ε_2 is the dielectric constant of the cement matrixes, and v_1 is the volume percentage of the ceramics.

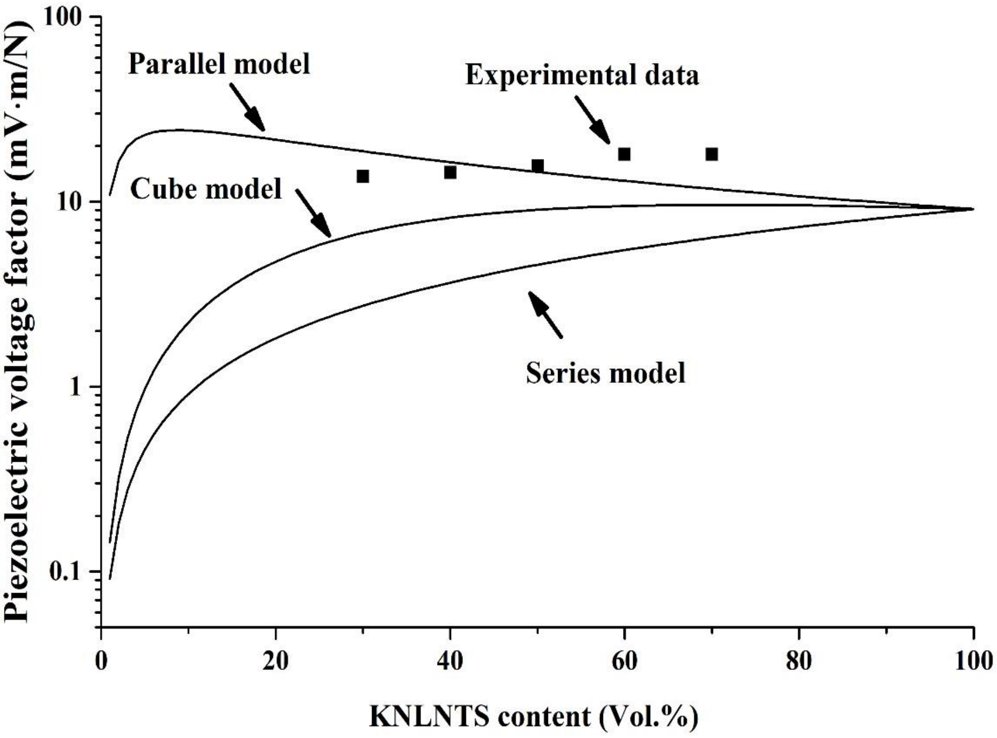

Figure 51 Comparison of the piezoelectric voltage factor from experimental data and the numerical model for 0-3 KNLNTS/ACSA cement composites.

5.2.4 Effect of hydration ages on dielectric and piezoelectric properties

The variations in the dielectric constant, and piezoelectric coefficient with different fractions of KNLNTS ceramics of the KNLNTS/ACSA cement composites with age are shown in Figure 52 and Figure 53, respectively. For the pure KNLNTS ceramic, it is evident that the dielectric constant and piezoelectric coefficient slightly decreased with ageing after polarisation. This can be attributable to the diverted 90° domains reverting to an increasingly disorderly state over time. As a result, the residual polarisation of piezoelectric ceramic in materials decreases with time [73-76]. By contrast, the relative dielectric constant and the piezoelectric coefficient of the KNLNTS/ACSA cement composites tended to enhance with longer ageing time. During the early stage the relative dielectric constant and the piezoelectric coefficient increased rapidly. The significant improvement of dielectric and piezoelectric properties at the early stage of hydration may be explained by variation of the pore structure from the hydration processes of the cement paste. During the initial stage of hydration, the cement matrix often has some big pores [77] which affect the relative dielectric constant and piezoelectric coefficients which presented the lowest values on day-1. These pores asserted a high influence on the binding of the KNLNTS ceramic and the cement matrix and decreased stress transfer inside the material caused by applied loads [73]. Because cement matrix is a porous substance, moisture is absorbed into the porous voids following poling. The pores in the cement matrix gradually close when the cement hydrates [62]. However, the hydration rate of the ACSA cement is higher than that of ordinary Portland cement [51], thus the porosity in the cement matrix rapidly decreased at the early age of hydration, resulting in the dielectric constant and the piezoelectric coefficients being significantly enhanced. After 7 days of polling age, the hydration reaction of the ACSA cement was nearly complete and the pore structure rarely changed at this stage. This clearly indicates that the dielectric constant and the piezoelectric coefficient are slightly affected by ageing time. In addition, it is found that the dielectric constant and the piezoelectric coefficient values of the 40 vol% KNLNTS and the 50 vol% KNLNTS composites are significantly different. The composite with less than 50 vol% ceramics content exhibited a higher non-piezoelectric cement matrix which raises the number of ions in the cement matrix, leading to a rise of current leakage to the composite [70]. Figure 54 shows the development of the piezoelectric voltage factor for the composite with different fractions of KNLNTS ceramics. The results indicate that the piezoelectric voltage factor drops early in the ageing process and the values become steady after 7 days. However, the piezoelectric voltage factor of the composites after 3 days were higher than that of the pure KNLNTS ceramic. Figure 55(a) shows the comparison between the dielectric constant and piezoelectric coefficient at 28 days of composites and pure ceramic after polarization. The comparison of dielectric constant and piezoelectric coefficient of composites and pure ceramic were found to be significantly different. Figure 55(b) shows the piezoelectric coefficient and dielectric constant ratio of composites and pure ceramic at 28 days. It demonstrated that the ratio of composites tends to increase with increasing KNLNTS ceramic from 0.12 – 0.16, while pure ceramic shows the ratio of 0.07 due to high dielectric constant value. Therefore, after calculated the piezoelectric voltage factor (Eq.5-8), the result of composite show slightly higher than the result of pure KNLNTS. These findings demonstrate that the KNLNTS/ACSA cement composite sensor is more sensitive than the KNLNTS ceramic sensor.

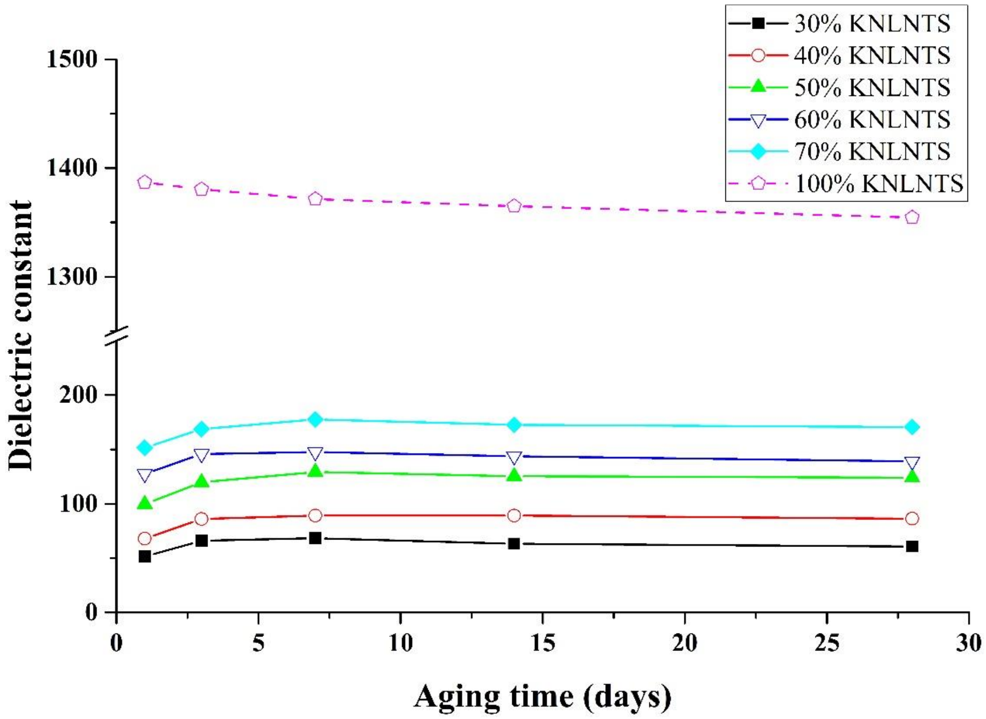

Figure 52 Variation over time of the dielectric constants for the KNLNTS ceramic and the KNLNTS/ACSA cement composites.

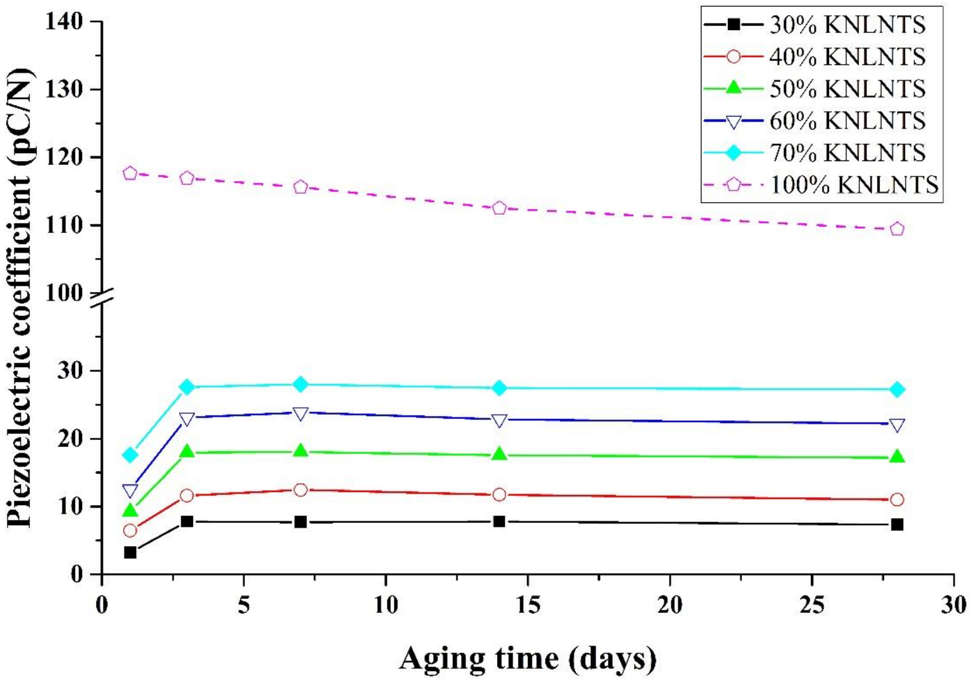

Figure 53 Variation over time of the piezoelectric coefficients for the KNLNTS ceramic and the KNLNTS/ACSA cement composites.

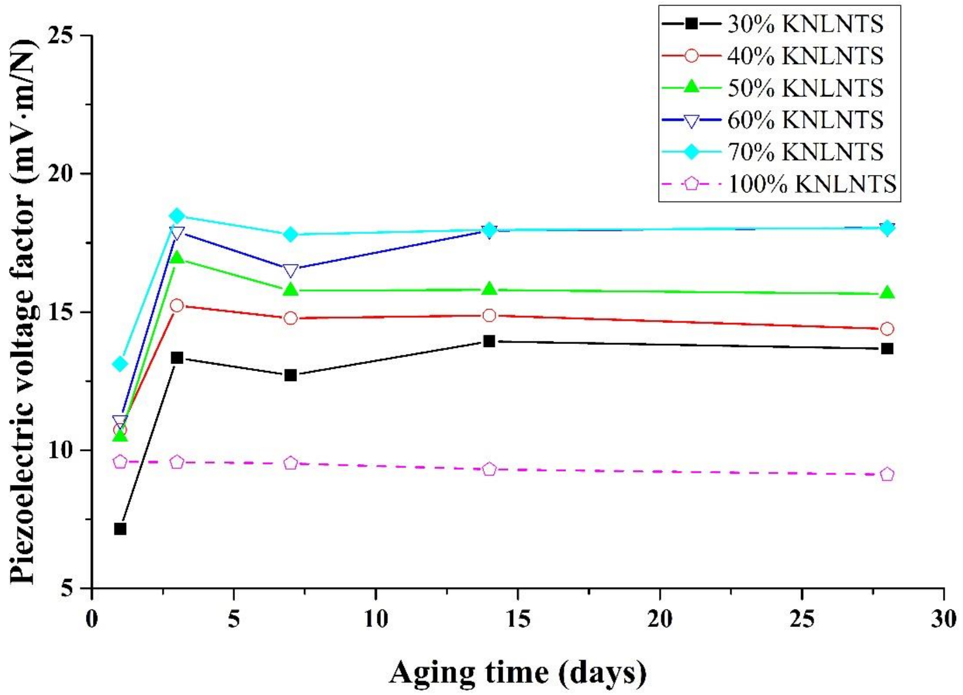

Figure 54 Variation over time of the piezoelectric voltage factor for the KNLNTS ceramic and the KNLNTS/ACSA cement composites.

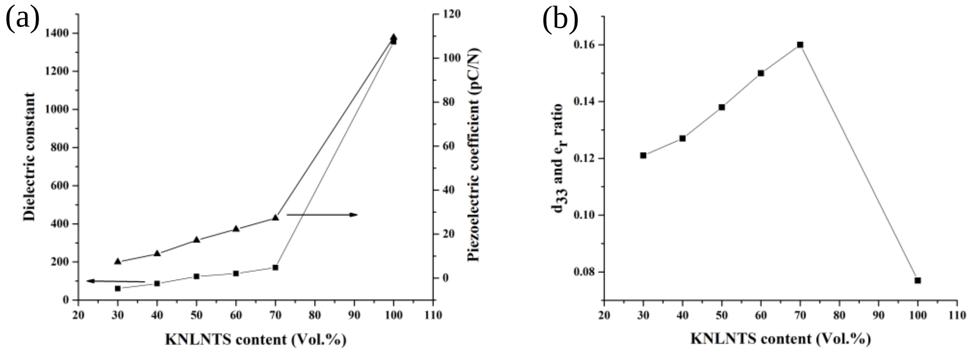

Figure 55 (a) The comparison between the dielectric constant and piezoelectric coefficient with KNLNTS content at 28 days, (b) The d_{33} / ε_r ratio and KNLNTS content at 28 days

CHAPTER VI CONCLUSIONS

Part I: Effects of CaF_2-CuO additives and various firing temperatures on characteristics of alite calcium sulfoaluminate clinkers

This study investigated the effects of adding CaF_2 and CuO and varying the firing temperature during production of ACSA clinkers. Findings revealed the following:

- Addition of CaF_2 and CuO greatly contributed to the phase formation, especially by promoting the occurrence of C_3S at low temperature. Clinkers with these additives attained formation of C_3S at the low firing temperature of 1,100 °C, while clinkers without the additives required 1,325 °C as the minimum firing temperature. At firing temperature of 1,250 °C, the *RMSE* revealed lowest values for clinker addition of CaF_2 and CuO compared to other firing temperatures and clinkers without additives. This suggested that the optimal firing temperature of ACSA with clinker additives was 1,250 °C.
- Increasing the $CaSO_4{\cdot}2H_2O$ content of the raw materials achieved a higher $M_{I:}$ M_{III} ratio, and vice versa. Loss of SO_3 due to evaporation during firing at high temperature reduced the content of the obtained $C_4A_3\bar{S}$ phase. Hence, excess $CaSO_4{\cdot}2H_2O$, as the source of SO_3, should be added to reduce this problem. Moreover, increasing the proportion of $CaSO_4{\cdot}2H_2O$ also had the side benefit of increasing C_3S content.

Part II: Fabrication and characterisation of 0–3 KNLNTS piezoelectric ceramic/alite calcium sulphoaluminate cement composites

The novel composite of KNLNTS piezoelectric ceramic - alite calcium sulfoaluminate cement were fabricated and investigated. Findings revealed the following:

- The optimum calcination temperature for synthesising lead-free KNLNTS powders is 750^{o}C. Although this firing condition could not achieve a pure perovskite phase, it does show the highest percent of perovskite phase (92%). Pure KNLNTS ceramics with optimum temperature was obtained after mixing the calcined powders with CuO (0.2 wt.%), Fe_2O_3 (0.4 wt.%), and Bi_2O_3 (0.3 wt.%) as the sintered aids and sintered at 1075^{o}C. The results of the phase identification, microstructural analysis, analysis of the dielectric properties, and the piezoelectric properties of the KNLNTS ceramic sintered at 1075^{o}C indicate that this ceramic material possesses the most desirable properties. Hence, this sintering condition was selected for fabrication of the KNLNTS ceramic for use as a raw material in the fabrication of the KNLNTS/ACSA cement composites.
- The KNLNTS/ACSA cement composites were fabricated with several KNNLTS fractions. The acoustic impedance test results demonstrate that composites with 30-70 vol% of KNLNTS ceramics are the most appropriate for use in piezoelectric sensor applications for OPC concrete since they match the acoustic impedance range. The dielectric properties and piezoelectric coefficient are highly related to the KNLNTS fraction. Increasing KNLNTS content significantly enhanced the dielectric and the piezoelectric properties, which were most clear when the KNLNTS fraction was greater than 50% by volume. Additionally, the dielectric constant and piezoelectric coefficient increased significantly at the early stage of hydration due to a sudden decrease in pore size and content in the cement matrix.

REFERENCES

1. Lea's chemistry of cement and concrete. 4th ed. ed. Lea FM, editor. London: Arnold; 1998.
2. Structure and performance of cements. 2nd ed. ed. Bensted J, Barnes P, editors. London ;: Spon Press; 2002.
3. Aitcin P-C. Sustainability of concrete. Mindess S, editor. Abingdon, Oxon: Spon Press; 2011.
4. Cement and concrete science & technology: vol.1,part 1. 1st ed. ed. Ghosh SN, editor. New Delhi: ABI; 1991.
5. Hanein T, Galvez-Martos J-L, Bannerman MN. Carbon footprint of calcium sulfoaluminate clinker production. Journal of Cleaner Production. 2018;172:2278-87.
6. Juenger MCG, Winnefeld F, Provis JL, Ideker JH. Advances in alternative cementitious binders. Cement and Concrete Research. 2011;41(12):1232-43.
7. Bullerjahn F, Schmitt D, Ben Haha M. Effect of raw mix design and of clinkering process on the formation and mineralogical composition of (ternesite) belite calcium sulphoaluminate ferrite clinker. Cement and Concrete Research. 2014;59:87-95.
8. Hargis CW, Telesca A, Monteiro PJM. Calcium sulfoaluminate (Ye'elimite) hydration in the presence of gypsum, calcite, and vaterite. Cement and Concrete Research. 2014;65:15-20.
9. Rungchet A, Poon CS, Chindaprasirt P, Pimraksa K. Synthesis of low-temperature calcium sulfoaluminate-belite cements from industrial wastes and their hydration: Comparative studies between lignite fly ash and bottom ash. Cement and Concrete Composites. 2017;83:10-9.
10. Gartner E. Industrially interesting approaches to “low-CO2” cements. Cement and Concrete Research. 2004;34(9):1489-98.
11. El-Alfi EA, Gado RA. Preparation of calcium sulfoaluminate-belite cement from marble sludge waste. Construction and Building Materials. 2016;113:764-72.
12. Shen Y, Qian J, Huang Y, Yang D. Synthesis of belite sulfoaluminate-ternesite cements with phosphogypsum. Cement and Concrete Composites. 2015;63:67-75.
13. Alvarez-Pinazo G, Santacruz I, Leon-Reina L, Aranda M, De la Torre A. Hydration Reactions and Mechanical Strength Developments of Iron-Rich Sulfobelite Eco-cements. 2013;52:16606–14.
14. Trauchessec R, Mechling JM, Lecomte A, Roux A, Le Rolland B. Hydration of ordinary Portland cement and calcium sulfoaluminate cement blends. Cement and Concrete Composites. 2015;56:106-14.
15. Skibsted J, editor Hydrate phase assemblages in blends of ye’elimite and gypsum with alite and belite. International Conference on the Chemistry of Construction Materials; 2016 10/10/2016; Technische Universität München.
16. Londono-Zuluaga D, Tobón JI, Aranda MAG, Santacruz I, De la Torre AG. Clinkering and hydration of belite-alite-ye´elimite cement. Cement and Concrete Composites. 2017;80:333-41.
17. Li X, Zhang Y, Shen X, Wang Q, Pan Z. Kinetics of calcium sulfoaluminate formation from tricalcium aluminate, calcium sulfate and calcium oxide. Cement and Concrete Research. 2014;55:79-87.
18. Puertas F, Varela MTB, Molina SG. Kinetics of the thermal decomposition of $C_4A_3\bar{S}$ in air. Cement and Concrete Research. 1995;25(3):572-80.

19. Dominguez O, Torres-Castillo A, Flores-Velez LM, Torres R. Characterization using thermomechanical and differential thermal analysis of the sinterization of Portland clinker doped with CaF2. Materials Characterization. 2010;61(4):459-66.

20. Duvallet T. Influence of ferrite phase in alite-calcium sulfoaluminate cements 2014.

21. Duvallet T, Zhou Y, Robl T, Andrews R. Synthesis and Characterization of High-Iron Alite-Calcium Sulfoaluminate-Ferrite Cements Produced from Industrial By-Products2014. 29-34 p.

22. Pérez-Bravo R, Compana J, Bruque S, Santacruz I, Alvarez-Pinazo G, Losilla E, et al. Alite sulfoaluminate clinker: Rietveld mineralogical and SEM-EDX analysis. Advances in Cement Research. 2014;26:10-20.

23. Ma X, Chen H-X, Wang P-M. Effect of CuO on the formation of clinker minerals and the hydration properties. Cement and Concrete Research - CEM CONCR RES. 2010;40:1681-7.

24. lv Y, Li X, Ma B, De Schutter G. Polymorph transformation of tricalcium silicate doped with heavy metal. Journal of Wuhan University of Technology-Mater Sci Ed. 2016;31:883-90.

25. Shih P-H, Chang J-E, Lu H-C, Chiang L-C. Reuse of heavy metal-containing sludges in cement production. Cement and Concrete Research. 2005;35(11):2110-5.

26. Ma S, Shen X, Gong X, Zhong B. Influence of CuO on the formation and coexistence of $3CaO{\cdot}SiO_2$ and $3CaO{\cdot}3Al_2O_3{\cdot}CaSO_4$ minerals. Cement and Concrete Research. 2006;36(9):1784-7.

27. Kornphom C, Udeye T, Thongbai P, Bongkarn T. Phase structures, PPT region and electrical properties of new lead-free KNLNTS-BCTZ ceramics fabricated via the solid-state combustion technique. Ceramics International. 2017;43:S182-S92.

28. Chootin S, Bongkarn T. Optimum Conditions for Preparation of High-Performance $(Ba_{0.97}Ca_{0.03})(Ti_{0.94}Sn_{0.06})O_3$ Ceramics by Solid-State Combustion. Journal of Electronic Materials. 2017;46(8):5215-24.

29. Mathrmool K, Udeye T, Bongkarn T. Low temperature fabrication of lead-free piezoelectric KNLNTS ceramics by the solid state combustion technique. Ferroelectrics. 2017;518:31-41.

30. Liu Y, Du Y, Cheng C, Sun X, Jiang N, Wang J, et al. Dielectric and impedance spectroscopy analysis of lead-free $(1-x)(K_{0.44}Na_{0.52}Li_{0.04})(Nb_{0.86}Ta_{0.10}Sb_{0.04})O_3$-$xBaTiO_3$ ceramics. Ceramics international. 2019;45(10):13347-53.

31. Mgbemere H, Herber R-P, Schneider G, M K. Investigation of the Dielectric and Piezoelectric Properties of Potassium Sodium Niobate Ceramics Close to the Phase Boundary at $(K_{0.35}na_{0.65})NbO_3$ and Partial Substitutions with Lithium and Antimony. Journal of the European Ceramic Society 29 (2009) 3273-3278. 2009;29.

32. Uthaisar C, Kantha P, Yimnirun R, Pojprapai S. Effect of Sintering Temperature of Lead-free $(K_{0.50}Na_{0.46}Li_{0.04})(Nb_{(0.96-x)}Sb_{0.04}Ta_x)O_3$ Ceramics on Piezoelectric Properties. Integrated Ferroelectrics. 2013;149:114-20.

33. Oh Y, Yoo J. Microstructural, piezoelectric properties and temperature stability in $Li_{0.02}(Na_{0.55}K_{0.45})_{0.98}[(Nb_{0.77}Ta_{0.18}Sb_{0.05})_{1-2x/5}Cu_x]O_3$ ceramics for piezoelectric actuator. Materials Letters. 2012;79:180-3.

34. Shin S-H, Han J-D, Yoo J. Piezoelectric and dielectric properties of B_2O_3-added $(Ba_{0.85}Ca_{0.15})(Ti_{0.915}Zr_{0.085})O_3$ ceramics sintered at low temperature. Materials Letters. 2015;154:120-3.

35. Jeong Y, Yoo J, Lee S, Hong J. Piezoelectric characteristics of low temperature sintering $Pb(Mn_{1/3}Nb_{2/3})O_3$–$Pb(Ni_{1/3}Nb_{2/3})O_3$–$Pb(Zr_{0.50}Ti_{0.50})O_3$ according to the addition of CuO and Fe_2O_3. Sensors and Actuators A: Physical. 2007;135:215–9.

36. Shin S-H, Ra C-M, Yoo J. Piezoelectric and dielectric properties of low temperature sintering $(Na_{0.52}K_{0.443}Li_{0.037})(Nb_{0.883}Sb_{0.08}Ta_{0.037})O_3$ ceramics substituted with $(Sr_{0.95}Ca_{0.05})TiO_3$. Materials Letters. 2016;178:166-70.

37. Li ZJ, Zhang D, Wu KR. Cement matrix 2-2 piezoelectric composite— Part 1. Sensory effect. Materials and Structures. 2001;34(8):506-12.

38. Dong B, Li Z. Cement-based piezoelectric ceramic smart composites. Composites Science and Technology. 2005;65(9):1363-71.

39. Li Z-X, Yang X-M, Li Z. Application of Cement-Based Piezoelectric Sensors for Monitoring Traffic Flows. Journal of Transportation Engineering. 2006;132(7):565-73.

40. Cheng X, Xu D, Lu L, Huang S, Jiang M. Performance investigation of 1-3 piezoelectric ceramic–cement composite. Materials Chemistry and Physics. 2010;121(1):63-9.

41. Lam KH, Chan HLW. Piezoelectric cement-based 1-3 composites. Applied Physics A. 2005;81(7):1451-4.

42. Li Z, Zhang D, Wu K. Cement-Based 0-3 Piezoelectric Composites. Journal of the American Ceramic Society. 2002;85(2):305-13.

43. Wen S, Chung DDL. Cement-based materials for stress sensing by dielectric measurement. Cement and Concrete Research. 2002;32(9):1429-33.

44. Li Z, Gong H, Zhang Y. Fabrication and piezoelectricity of 0–3 cement based composite with nano-PZT powder. Current Applied Physics. 2009;9(3):588-91.

45. Han R, Shi Z. Dynamic analysis of sandwich cement-based piezoelectric composites. Composites Science and Technology. 2012;72(8):894-901.

46. Chaipanich A. Effect of PZT particle size on dielectric and piezoelectric properties of PZT–cement composites. Current Applied Physics. 2007;7(5):574-7.

47. Hunpratub S, Yamwong T, Srilomsak S, Maensiri S, Chindaprasirt P. Effect of particle size on the dielectric and piezoelectric properties of 0–3BCTZO/cement composites. Ceramics International. 2014;40:1209-13.

48. Pan H-H, Lin D-H, Yeh R-H. Influence Of Pozzolanic Materials On 0–3 Cement-Based Piezoelectric Composites2013. 929-34 p.

49. A. Aldieb M, Ibrahim H. Variation of Feed Chemical Composition and Its Effect on Clinker Formation-Simulation Process. 2010;2187.

50. Chitvoranund N, Winnefeld F, Hargis C, Sinthupinyo S, Lothenbach B. Synthesis and hydration of alite-calcium sulfoaluminate cement. 2017. p. 101-11.

51. Hu Y, Li W, Ma S, Wang Q, Zou H, Shen X. The composition and performance of alite-ye'elimite clinker produced at 1300 °C. Cement and Concrete Research. 2018;107:41-8.

52. Liu X, Li Y, Zhang N. Influence of MgO on the formation of Ca_3SiO_5 and $3CaO{\cdot}3Al_2O_3{\cdot}CaSO_4$ minerals in alite–sulphoaluminate cement. Cement and Concrete Research. 2002;32(7):1125-9.

53. Fundamentals of piezoelectric sensorics : mechanical, dielectric, and thermodynamical properties of piezoelectric materials. Tich[illegible]i J, editor. Berlin: Springer; 2010.

54. Safari A, Akdogan EK. Piezoelectric and acoustic materials for transducer

applications: Springer; 2008.
55. Sikalidis C. Advances in Ceramics: Electric and Magnetic Ceramics, Bioceramics, Ceramics and Environment: IntechOpen; 2011.
56. Barsoum M, Barsoum MW. Fundamentals of Ceramics: CRC Press; 2002.
57. Sharma D, Kholkin A, Kumari S, Sharma S. Effect of potassium content on the dielectric and electrical properties of sodium potassium niobate ceramics2015. 151-4 p.
58. Chaipanich A. Dielectric and piezoelectric properties of PZT–cement composites. Current Applied Physics. 2007;7(5):537-9.
59. Potong R, Rianyoi R, Ngamjarurojana A, Chaipanich A. Microstructure and performance of 1–3 connectivity environmental friendly lead-free BNBK-Portland cement composites. Materials Research Bulletin. 2017;90:59-65.
60. Rianyoi R, Potong R, Ngamjarurojana A, Chaipanich A. Dielectric and piezoelectric properties of 2-2 connectivity lead-free piezoelectric ceramic $Bi_{0.5}Na_{0.5}TiO_3$/Portland cement composites. Ceramics International. 2018.
61. Chomyen P, Potong R, Rianyoi R, Ngamjarurojana A, Chindaprasirt P, Chaipanich A. Microstructure, dielectric and piezoelectric properties of 0–3 lead free barium zirconate titanate ceramic-Portland fly ash cement composites. Ceramics International. 2018;44(1):76-82.
62. Pan H-H, Wang C-K, Cheng Y-C. Curing time and heating conditions for piezoelectric properties of cement-based composites containing PZT. Construction and Building Materials. 2016;129.
63. Lu X, Ye Z, Wang S, Du P, Li C, Cheng X. Study on the preparation and properties of belite-ye’elimite-alite cement. Construction and Building Materials. 2018;182:399-405.
64. Assaad J. Effect of energy and temperature on performance of alkanolamine processing additions. Minerals Engineering. 2017;102:30-41.
65. Assaad J, Issa C. Effect of clinker grinding aids on flow of cement-based materials. Cement and Concrete Research. 2014;63:1–11.
66. Potong R, Rianyoi R, Jarupoom P, Pengpat K, Chaipanich A. Effect of Particle Size on the Dielectric Properties of Sodium Potassium Niobate -Portland Cement Composites. Ferroelectrics Letters Section. 2009;36(3-4):76-81.
67. Staněk T, Sulovský P. The influence of the alite polymorphism on the strength of the Portland cement. Cement and Concrete Research. 2002;32(7):1169-75.
68. Wang C, Zhou Z, Liu CX, Cheng X. Effects of CaF2 on the Formation Kinetics of Portland Cement Clinker. Advanced Materials Research. 2011;306-307:966-9.
69. Shaik SB, Karthikeyan J, Jayabalan P. Influence of using agro-waste as a partial replacement in cement on the compressive strength of concrete – A statistical approach. Construction and Building Materials. 2020;250:118746.
70. Potong R. Dielectric and piezoelectric properties of modified barium titanate-Portland cement composites: Chiang Mai University; 2013.
71. Newnham RE, Bowen LJ, Klicker KA, Cross LE. Composite piezoelectric transducers. Materials & Design. 1980;2(2):93-106.
72. Banerjee S, Cook-Chennault KA. Influence of Al Particle Size and Lead Zirconate Titanate (PZT) Volume Fraction on the Dielectric Properties of PZT-Epoxy-Aluminum Composites. Journal of Engineering Materials and Technology. 2011;133(4).
73. Xin C, Shifeng H, Jun C, Ronghua X, Futian L, Lingchao L. Piezoelectric and dielectric properties of piezoelectric ceramic–sulphoaluminate cement composites.

Journal of the European Ceramic Society. 2005;25(13):3223-8.

74. Chaipanich A, Rianyoi R, Potong R, Jaitanong N. Aging of 0–3 piezoelectric PZT ceramic–Portland cement composites. Ceramics International. 2014;40(8, Part B):13579-84.

75. Herbiet R, Tenbrock H, Arlt G. The aging behaviour of the complex material parameters ε, d and s in ferroelectric PZT ceramics. Ferroelectrics. 1987;76(1):319-26.

76. Kholkin AL, Tagantsev AK, Colla EL, Taylor DV, Setter N. Piezoelectric and dielectric aging in pb(zr,ti)o3 thin films and bulk ceramics. Integrated Ferroelectrics. 1997;15(1-4):317-24.

77. Pan HH, Chiang C-K. Effect of aged binder on piezoelectric properties of cement-based piezoelectric composites. Acta Mechanica. 2014;225(4):1287-99.